ABSTRACT

Title of Dissertation:
RECEPTOR MOBILITY AND
CYTOSKELETAL DYNAMICS AT THE
IMMUNE SYNAPSE: THE ROLE OF ACTIN
REGULATORY PROTEINS

Ivan Adolfo Rey Suarez
Doctor of Philosophy, 2020

Dissertation directed by:
Professor Arpita Upadhyaya
Department of Physics

Spatial and temporal regulation of actin and microtubule dynamics is of utmost importance for many cellular processes at different sub-cellular length scales. This is particularly relevant for cells of the immune system, which must respond rapidly and accurately to protect the host, where B cells and T cells are the main players during the adaptive immune response. An understanding of the biophysical principles underlying cytoskeletal dynamics and regulation of signaling will help elucidate the fundamental mechanisms driving B and T cell immune response.

B cell receptor (BCR) diffusivity is modulated by signaling activation, however the factors linking mobility and signaling state are not completely understood. I used single molecule imaging to examine BCR mobility during signaling activation and a novel machine learning based method to classify BCR trajectories into distinct diffusive states. Inhibition of actin dynamics downstream of the actin nucleating factors Arp2/3 and formins resulted decreased BCR mobility. Loss of the Arp2/3 regulator, N-WASP, which is associated with enhanced signaling, leads to a predominance of BCR trajectories with lower diffusivity. Furthermore, loss of N-WASP reduces diffusivity of the stimulatory co-receptor CD19, but not that of unstimulated FcγRIIB, an inhibitory co-receptor. Our results implicate the dynamic actin network in fine-tuning receptor mobility and receptor-ligand interactions, thereby modulating B cell signaling.

Activation of T cells leads to the formation of the immunological synapse (IS) with an antigen presenting cell (APC). This requires T cell polarization and coordination between the actomyosin and microtubule cytoskeleton. The interactions between the different cytoskeletal components during T cell activation are not well understood. I use high-resolution fluorescence microscopy to study actin-microtubule crosstalk during IS formation. Microtubules in actin rich zones display more deformed shapes and higher dynamics compared to MTs at the actin-depleted region. Chemical inhibition of formin and myosin activation reduced MT deformations, suggesting that actomyosin contractility plays an important role in defining MT shapes. Interestingly MT growth was slowed by formin inhibition and resulting enrichment of Arp2/3 nucleated actin networks. These observations indicate an important mechanical

coupling between the actomyosin and microtubule systems where different actin structures influence microtubule dynamics in distinct ways.

RECEPTOR MOBILITY AND CYTOSKELETAL DYNAMICS AT THE
IMMUNE SYNAPSE: THE ROLE OF ACTIN REGULATORY PROTEINS

by

Ivan Adolfo Rey Suarez

Dissertation submitted to the Faculty of the Graduate School of the
University of Maryland, College Park, in partial fulfillment
of the requirements for the degree of
Doctor of Philosophy
2020

Advisory Committee:

 Dr Arpita Upadhyaya, Chair
 Dr Hari Shroff
 Dr Helim Aranda-Espinoza
 Dr Wolfgang Losert
 Dr Wenxia Song, Dean's Representative

Preface

From my curiosity for insects in my backyard during my childhood to the spotting of wildlife in the Amazon jungle, I have always enjoyed observing the complex interrelations found in nature. How structure and function are interconnected in nature at every length scale, is fascinating for me. This interest led me to pursue a PhD in biophysics where I was very lucky to study different biophysical aspects of the cytoskeleton, a complex and dynamic network of bio-polymers, in a system of great biomedical relevance – the adaptive immune system.

Cells of the immune system must respond rapidly and accurately to the presence of pathogens. A critical part of the machinery responsible for proper immune response is the cytoskeleton. What I found most interesting during my doctoral studies is that the main components of the cytoskeleton, actin and microtubules, are highly conserved across eukaryotic cells, yet immune cells can migrate through the body and rapidly transition to adhere transiently to a cell showing signs of infection to either initiate or effect the immune response. This ability is conferred by the cytoskeleton regulators that can be activated through specific signaling pathways to control cytoskeletal dynamics in space and time. In this dissertation I summarize my studies on the role of actin regulators in modulating the adaptive immune response.

Dedication

I dedicate this dissertation to Tata, Fausto, Canela, Miro and Turquesa (and to all the wild cats of the world – especially jaguars).

Acknowledgements

Table of Contents

List of Figures

List of Abbreviations

APC   Antigen Presenting Cells

BCR   B Cell Receptor

BLNK   B cell linker protein

Btk   Bruton's tyrosine kinase

DAG   Diacylglycerol

DMSO   Dimethyl sulfoxide

dSTORM   Direct stochastic optical reconstruction microscopy

EGTA   ethylene glycol tetraacetic acid

EMTB   ensconsin microtubule-binding domain

ERM Ezrin,   radixin and moesin

F-actin   Filamentous actin

FAK   focal adhesion kinase

GFP   Green Fluorescent Protein

Grb2   Growth factor receptor-bound protein 2

ICAM-1   Intercellular Adhesion Molecule 1

IL-2   interleukin 2

IP3   inositol 1,4,5-trisphosphate

IS   Immunological synapse

iSIM   Instant Structured Illumination Microscopy

ITAM   Immunoreceptor Tyrosine-based Activation Motif

LAT   Linker of activated T cells

Lck   lymphocyte-specific protein tyrosine kinase

LFA-1   Lymphocyte function-associated antigen 1

MHC   Major Histocompatibility Complex

MTOC   microtubule organization center

Nck   non-catalytic region of tyrosine kinase

N-WASP   Neuronal Wiskott–Aldrich Syndrome protein

pEM   Perturbation-Expectation Maximization

PIP2   phosphatidylinositol-4,5-biphosphate

PKC   protein kinase C

PLCγ1   PhospholipaseCγ1

pMHC   peptide-MHC complex

SLP-76   Lymphocyte cytosolic protein 2

SMAC   Supra Molecular Activation Cluster

TCR   T Cell Receptor

TIRF   Total Internal Reflection Fluorescence

WASp   Wiskott-Aldrich syndrome protein

WAVE2   Wiskott-Aldrich syndrome protein family member 2

ZAP-70   Zeta-chain-associated protein kinase 70

Chapter 1: Introduction

1.1 Overview of the Thesis

The cytoskeleton is a complex and dynamic network of protein filaments that play a wide variety of roles of vital importance for eukaryotic cells. The classical view of the cytoskeleton is that of a molecular scaffold providing structural support at many scales in the cell. It is, however, a very dynamic system that allows cells to change shape, divide and migrate. Over the recent years novel roles for the cytoskeleton have been discovered. Along with the discovery of the importance of external physical cues on cell fate and behavior, the acto-myosin cytoskeleton has been implicated in playing a major role in the sensing and transmission of these physical cues. This is particularly true for cells of the immune system that must respond rapidly and accurately to the presence of pathogens.

B and T lymphocytes are the main agents responsible for the adaptive immune response, which confers protection against new pathogens. These cells navigate the body looking for signs of infection and use special surface receptors to detect the presence of pathogen fragments (antigen) in the surface of antigen presenting cells. The detection of antigen leads to the formation of a contact region between the lymphocyte and the cell presenting the antigen. This contact zone is known as an immunological

synapse and is an essential step in the immune response. The coordinated remodeling of the actin and microtubule cytoskeletons is required for proper formation of the immune synapse and its stabilization.

In the first chapter of this thesis I provide a summary of the steps that lead to the immune synapse formation and describe in detail the role that the cytoskeleton plays during this process. In the second chapter of this thesis I highlight the importance of the actin cytoskeleton and associated regulators in the modulation of signaling activation in B cells through the control of membrane receptor diffusivities and hypothesize about the role of actin as a catalyzer of the biochemical reactions at the membrane-proximal cytoplasm. In the third chapter of the thesis I show the importance of the interactions between different cytoskeletal systems during the activation of T cells, highlighting the importance of studying the actin and microtubules networks as a complex intertwined system.

1.2 Adaptive immune response

Mammals, among other vertebrates, possess two defensive immune systems that protect them from the invasion of pathogenic microorganisms: the innate and the adaptive immune system. Both systems are composed of specialized types of cells that use membrane receptors to identify possible pathogens. The innate immune system provides an early defense against infections, thanks to the rapid recognition of pathogen-associated molecular patterns through receptors on the membrane of the effector cells. Recognition of microbial patterns leads to the phagocytosis and

destruction of the pathogen. Cells of the innate immune system, like dendritic cells, can also ingest and process pathogen-associated protein structures or antigens for later presentation to cells of the adaptive immune system [1].

While the innate immune systems acts rapidly, the number of protein structures associated with pathogens that are recognized by its cells is limited to less than a thousand [2]. In contrast, effective action by the adaptive immune system takes longer and the specificity of pathogenic protein structures detection is far more diverse (lymphocytes can recognize more than a billion different antigens).

A fundamental step in the adaptive immune response is mediated by a group of cells of the innate immune system known as antigen presenting cells (APC). These cells, upon detection of potentially harmful antigens, will phagocytize and digest these antigens for presentation at their surface for detection by adaptive immune cells as shown in Figure 1.1a [3]. The role of B and T lymphocytes is critical for the adaptive immune response. The recognition of pathogenic antigen can activate B cells and T cells and lead to proliferation of cells specific for the structure identified. The immune response launched by these cells can either kill pathogens directly or through the secretion of antibodies.

Binding of these antibodies to the pathogen facilitates its recognition by cells of the innate immune system like macrophages and neutrophils, enhancing the phagocytosis

of the pathogen and disrupting the infection [4].The adaptive immune response can provide long-term immunity to the host through the proliferation and establishment of memory cells that will protect upon reinfection with the same type of pathogen, providing an efficient and quick response (Figure 1.1b). The adaptive immune system can respond to pathogens in two ways: cell-mediated immune response, which is carried out by T cells and humoral immune response which is carried out by activated B cells and antibodies as shown by Figure 1.1c.
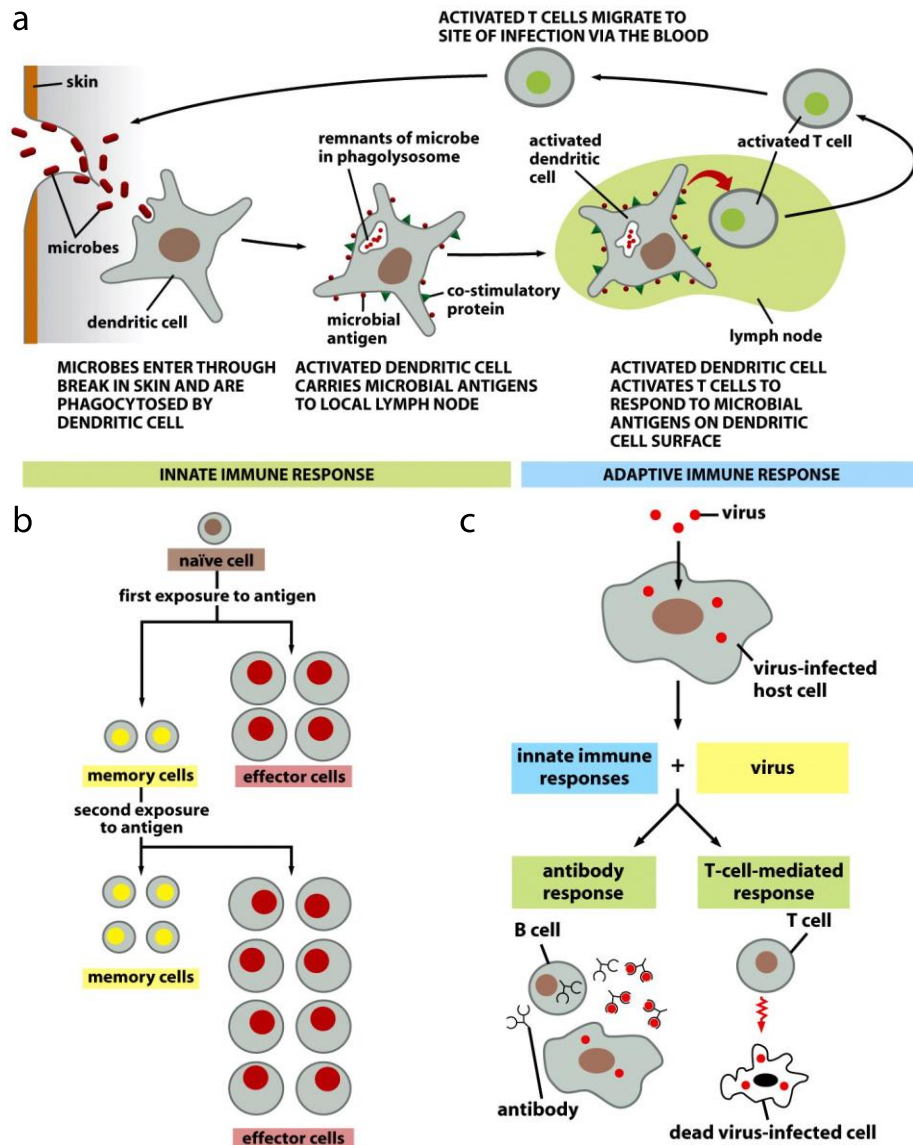
Figure 1.1. The adaptive immune response. a) Pathogen detection and antigen presentation by antigen presenting cells to cells of the adaptive immune system. b) Antigen recognition leads to proliferation of cells and differentiation into effector and memory cells, the latter providing long-term protection for the host. c) Diagram showing the two types of adaptive immune response, humoral or antibody response

5

carried out by B cells and cell-mediated response carried out by T cells. Figure panels taken from [3]. Image used with permission.

1.3 The immunological synapse

Adaptive immunity is mediated by B and T lymphocytes that are activated through interaction with antigen presenting cells (e.g. dendritic cells or macrophages). This interaction is triggered by the recognition of antigen on the APC membrane surface through specialized receptors. In B cells the antigen-recognition molecules are immunoglobulins or Ig, which have a vast range of specificities. Membrane-bound immunoglobulins, known as B cell receptors (BCR), allow the cell to detect antigen. In T cells the antigen-recognition molecule is known as T cell receptor (TCR) and instead of recognizing and binding antigen directly, like the BCR, it recognizes short peptide fragments of antigen bound to special receptors on the surface of APCs known as major histocompatibility complex (MHC) [5]. The engagement of the BCR or the TCR triggers a signaling cascade that activates multiple downstream signaling molecules and spatiotemporal assembly of these molecules into microclusters. Concurrent with this, the B or T cell polarizes and spreads over the antigen-presenting surface in a cytoskeleton-dependent manner. The contact region formed between the two cells is known as the immunological synapse and provides a stable platform for cell-to-cell communication during the immune response. Remodeling of the actin cytoskeleton and polarization of the microtubule cytoskeleton are essential steps for proper formation and maturation of the immunological synapse. In the following

6

sections I will introduce the main regulators of both actin and microtubule cytoskeletal systems.

1.4 The actin cytoskeleton: Nucleators and regulators.

The actin cytoskeleton is essential at many levels for the formation of the immunological synapse and the immune response. The basic unit of actin is a globular monomer known as G-actin (or globular actin). Actin monomers can self-assemble into asymmetric filaments known as F-actin, which possess a fast growing end (barbed end) and a slow growing end (pointed end). Such spontaneous nucleation is kinetically unfavorable because the actin dimer intermediate is very unstable (Figure 1.2a) [6, 7]. Actin filament polymerization can be accelerated and sustained by a group of proteins known as nucleators. The Arp2/3 complex is perhaps the best known and consists of a stable assembly of seven polypeptides. Arp2/3 complex mediated nucleation starts by binding a mother filament where it initiates growth in the barbed direction at a 70° angle (see Figure 1.2b). This molecular complex is largely inactive on its own and requires activation by a group of proteins known as nucleation promoting factors (NPFs). The activities of NPFs are regulated by signal-transduction pathways, thus coordinating actin polymerization in space and time [7]. The best characterized NPFs are the proteins of the WASP (Wiskott-Aldrich syndrome protein) family: WASP, N-WASP, Scar/WAVE1, Scar/WAVE2 and Scar/WAVE3 [8].

WASP-family proteins have a conserved domain in the C-terminus known as VCA, which allow them to bind and activate the Arp2/3 complex. Despite the structural similarities, these proteins can induce different actin polymerization rates with Scar1 being the slowest, followed by WASP (16-fold higher than Scar) and N-WASP (70-fold higher than Scar) [9]. WASP and N-WASP exist in an autoinhibited configuration that blocks the VCA domain. These proteins are activated by GTPases like Cdc42, Nck and Grb2 among others [8]. The nucleation of actin mediated by Arp2/3 gives rise to structures on the cellular scale such as the lamellipodium of crawling cells (see Figure 1.2 d,e). The other major class of actin nucleators are the proteins of the formin family. Formins are large multi-domain proteins with a fomin homology domain 2 (FH2) that allows them to bind to actin [10]. Formin binds to an actin dimer or trimer and stabilizes it, and then promotes actin assembly and displays processive movement on the growing barbed end while protecting the filament from capping proteins (Figure 1.2c). This results is an unbranched filament that can give rise to protruding structures as filopodium (Figure 1.2f) or that through association with myosin motors can produce contractile actin arcs.
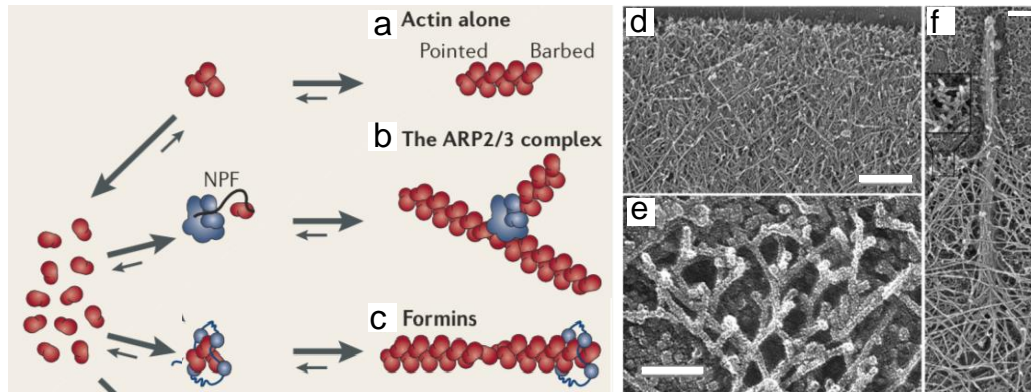
Figure 1.2. Actin nucleators and resulting architectures. Actin filament formation can be the result of a) Self-assembly, b) branched nucleation from existing filament by Arp2/3 or c) nucleation by formin. The larger arrows correspond to more favorable conformations. Electron micrographic images showing the actin cytoskeleton for d) the lamellipodium of a Xenopus Keratinocyte (scale bar is 500 nm), e) zoomed region of lamellipodium showing the branched actin structure formed by Arp2/3 mediated nucleation (scale bar 100 nm) and f) a filopodium formed by formin nucleated actin cables (scale bar is 200 nm). Panels a-c taken from [7]. Panels d-f taken from [8]. Images used with permission.

1.5 Microtubule filaments: Dynamics and associated proteins

Microtubules (MTs) play an important role during immune synapse formation by serving as highways for intracellular transport, recycling of membrane proteins and repositioning of centrosome-associated organelles towards the APC [11]. MTs are tubular hollow polymers of approximately 25 nm outer diameter and higher rigidity than actin filaments [12]. MTs are formed through the polymerization of αβ-tubulin

9

heterodimers that is regulated by the hydrolysis of GTP bound to the β subunit [13] (Figure 1.3). The energy input from GTP hydrolysis allows for non-equilibrium polymerization dynamics in which prolonged phases of depolymerization (catastrophe) alternate stochastically with prolonged phases of polymerization (rescue), a phenomenon denominated dynamic instability [12]. Nucleation of MTs occurs primarily at microtubule-organizing centers (MTOC), which are usually composed of a pair of cylindrical centrioles surrounded by pericentriolar material containing γ-tubulin, a tubulin isoform, in a large complex with other proteins that functions as a nucleating seed [14]. MT filaments have a defined polarity with a very dynamic plus end, where β-tubulin is exposed, and a stable minus end, where α-tubulin is exposed, that is typically bound to the MTOC [15]. The spatiotemporal dynamics of microtubules is regulated by microtubule associated proteins (MAPs) which includes molecular motors like kinesin and dynein and plus tip proteins, which can bind to growing MTs plus ends (EB1, CLIP-170) or to growing and shrinking MTs plus ends (Dam1, Kar9) [16] as shown in figure 1.3. End binding proteins, like EB1 or EB3, bound to GFP can be used to quantify microtubule growth speeds using fluorescence microscopy [17] and evaluate the effect that disruption of actin networks has on MT growth as shown in Chapter 3 of this thesis.
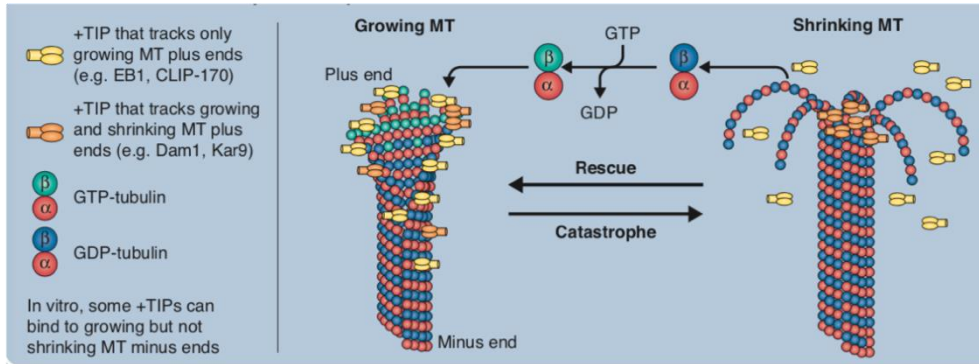
Figure 1.3. Microtubule dynamics and plus tip proteins. Microtubules are highly dynamic structures that undergo events of catastrophe (rapid depolymerization) and rescue. Plus tip proteins can bind to the polymerizing end of the microtubule and help stabilize it and sustain growth. Image taken from [16]. Image used with permission.

1.6 The BCR and B cell signaling activation

Antigen detection by B cells relies on the immunoglobulin-like receptors at their surface. The basic structure of the B cell receptor is shown in Figure 1.4a. It consists of a light chain bound through disulfide bonds to the heavy chain, which in turn is non-covalently bound to two transmembrane signaling molecules, Igα and Igβ, containing immune tyrosine activation motifs (ITAM). There are five different heavy chain structures that lead to five different classes of antibodies, IgA, IgD, IgE, IgG and IgM [3]. Mature naïve B cells express IgG and IgM on their surface. BCR crosslinking by antigen is required for activation [18] and initiates a signaling cascade as shown in Figure 1.4b. At the membrane, antigen crosslinking induces the clustering of BCR which become signaling amplification subunits or signalosomes. These clusters are

typically associated with cholesterol and glycolipid-rich membrane regions, liquid ordered lipid domains or lipid rafts, where the BCR ITAMs can be phosphorylated by the Src-family kinase Lyn [19, 20]. ITAM phosphorylation allows binding of Syk kinase to the Igα/β, which activates its tyrosine kinase activity. Once Syk is activated, it phosphorylates and activates phospholipase Cγ2 (PLCγ2), Bruton's tyrosine kinase (Btk), adaptor proteins like BLNK and Grb2 and the coreceptor CD19 among other molecules that are recruited to BCR clusters [21, 22]. Following signal propagation, inhibitory phosphatases like SH2-containing tyrosine (SHP) and phosphatidylinositol-5 phosphatases (SHIP) become activated [23, 24]. The negative regulation of signaling can also involve membrane surface receptors like CD22 and FcγRIIB. Indeed, the colligation of BCR with FcγRIIB can lead to the activation of the phosphatase SHIP which leads to the removal of lipid raft-docking sites for PlCγ2, Akt and Btk thus inhibiting their activation. CD22 contains immune receptor tyrosine-based inhibitory motifs (ITIMs) within its cytoplasmic tails and can recruit the tyrosine phosphatase SHP1 to microclusters and inhibit BCR signaling [25].
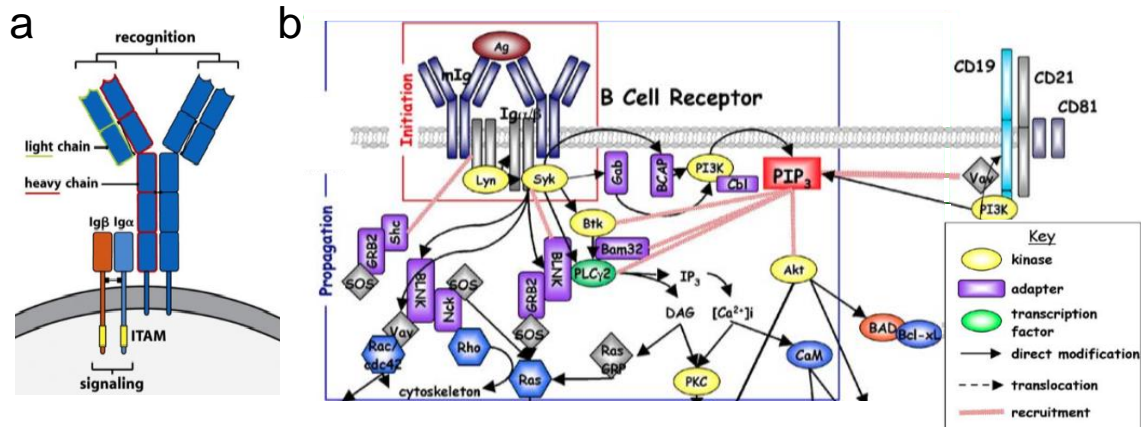
Figure 1.4. BCR structure, activation and signaling propagation. a) B cell receptor structure consisting of a light chain (highlighted in yellow) and a heavy chain (highlighted in red) non-covalently bound to transmembrane subunits containing ITAM signaling motifs. b) BCR signaling activation cascade induced by antigen engagement. Panel a taken from [5] and panel b taken and adapted from [21]. Images used with permission.

1.6.1 BCR configuration before and after activation

Two primary models describe the configuration of the resting BCR as either dispersed monomers [18, 19] or in an oligomeric configuration where nanoclusters of 60-80 molecules are tightly packed and surrounded by actin fences [26–29]. In the oligomeric configuration BCR remain in an auto-inhibited configuration within the clusters (Figure 1.5a). The crosslinking of BCR with antigen increases the spacing between these molecules and exposes their ITAM regions for phosphorylation by tyrosine kinases [30], thus inducing a signaling cascade. The activation of BCR signaling

induces actin remodeling, which increases the spacing between other BCR molecules, exposing their ITAMs and amplifying the signal. In the monomeric configuration, the crosslinking of BCR with antigen allows a more stable platform for kinases associated with lipid rafts (Figure 1.5b) to phosphorylate their ITAM regions. This signaling cascade induces actin remodeling which allows more BCR to aggregate, coalesce and form microclusters. A study using direct stochastic optical reconstruction microscopy (dSTORM) found that BCR of the IgM (Figure 1.5c) and the IgG class reside in highly heterogeneous clusters that vary in size and number [28]. This evidence supports both models and is likely that both configurations and processes occur in nature [31]. In both cases, actin remodeling is key for signaling amplification.
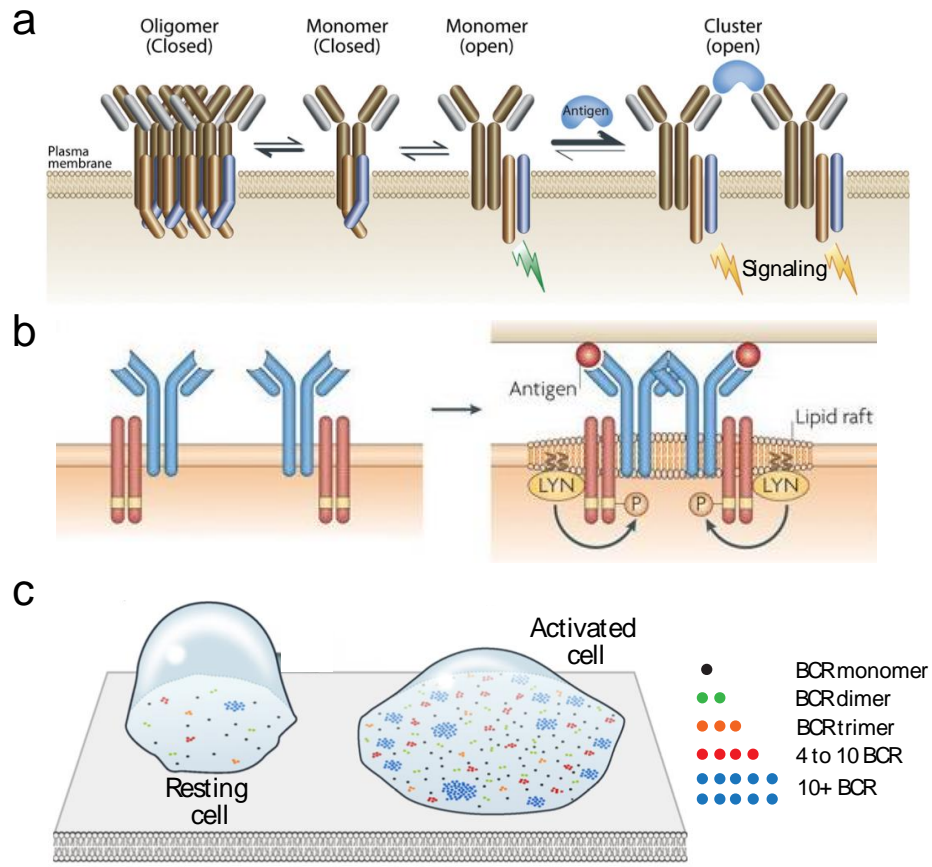
Figure 1.5. Nanoscale organization of BCR in resting and activated cells. a) Dissociation activation model where BCR resides in an auto-inhibited oligomeric configuration and antigen binding leads to increased space between BCRs exposing the ITAM. b) BCR crosslinking through antigen on the APC surface perturbs local lipid environment causing lipid raft coalescence and bringing kinase Lyn to the ITAM. c) IgM BCR nanoscale configuration in resting and activated B cells obtained from super-resolution imaging. Panel a was taken from [32], Panel b was adapted from [33] and panel c was adapted from [28]. Images used with permission.

1.6.2 Actin cytoskeleton modulates BCR signaling

BCR activation induces actin remodeling that serves different purposes at different time and length scales. On resting cells the actin cortex has been found to control the activation of BCR and its interaction with coreceptors like CD19 by defining barriers that limit receptor mobility [26, 27]. Cortical actin regulates the spatial distribution of memebrane receptors via the ezrin-radixin-moesin (ERM) family proteins which link the cytoskeleton to the plasma membrane [34]. Thus alteration of cortical actin can induce BCR signaling [26, 35]. BCR antigenic stimulation induces actin remodeling that leads to segregation of proteins at the plasma membrane. Actin polymerization is necessary for microcluster growth and coalescence [36, 37] which leads to signal amplification. This effect is likely mediated through Arp2/3 nucleation of branched actin networks [38]. B cell spreading onto the APC also depends on actin polymerization. During spreading, F-actin accumulates at the leading edge as shown in Figure 1.6a and actin polymerization foci co-localize with BCR microclusters inducing signal amplification [39, 40]. Centripetal movement of BCR clusters is driven by actin retrograde flow [41] and supported/accompanied by transport along microtubules by Dynein through association with the ubiquitin ligase Cbl and adaptor proteins Grb2 and Dok-3 [42]. The accumulation of BCR clusters at the center of the contact zone (also known as central cluster formation) together with the contraction of the cell (see figure 1.6b) leads to signal downregulation [19, 39, 43].

Spreading
Signaling amplification

Contraction
Signaling downregulation
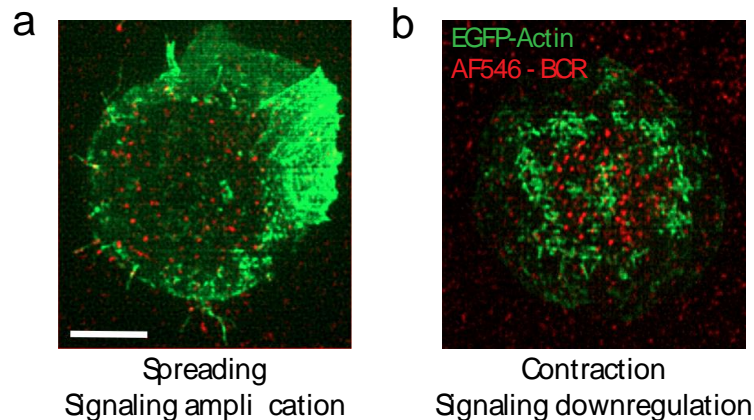
Figure 1.6. Actin mediated spreading and contraction modulates signaling. a) Instant structured Illumination Microscopy (iSIM) [44] images of activated EGFP-Actin A20 cells fixed on supported lipid bilayers at 3 minutes after activation (Spreading phase) and b) 6 minutes after activation (contraction phase). Scale bar is 5 μm.

The actin cytoskeleton has a large number of regulatory and adaptor proteins that have the ability to modulate BCR signaling. The actin binding factor cofilin severs actin filaments. BCR activation induces the dephosphorylation of cofilin which allows it to bind actin [45]. The severing of actin by cofilin promotes remodeling of the actin cortex and allows BCR clustering and interaction with signaling coreceptors. Furthermore, cofilin activation by Toll-like receptor stimulation sensitizes B cells and enhances signaling by reducing the spatial confinement of BCR [46]. In contrast to cofilin's positive regulation of signaling, the actin adapter molecule Actin-binding protein 1 (Abp1) assists BCR signal attenuation by promoting central cluster formation and recruitment of inhibitory signaling molecules [47].

17

The proteins of the WAS (Wiskott Aldrich Syndrome) family are well known actin regulators that promote Arp2/3 filament nucleation [48] and are very relevant in the adaptive immune response. WAS patients exhibit immune deficiency and high incidence of autoimmune diseases and lymphoid cancers [39]. During B cell spreading, activated WASP co-localizes with BCR microclusters and at the leading edge of the cell [37, 49] promoting actin polymerization associated with signaling enhancement. However, WASP-deficient B cells display reduced BCR internalization, which is a fundamental step in signal attenuation, thus suggesting that WASP can contribute to BCR signaling both by positive and negative feedback [50]. N-WASP is a close homolog of WASP with a more evident role in signaling downregulation. B cells from B-cell-specific N-WASP knockout mice display delayed contraction and impaired formation of central cluster and BCR internalization [50].

1.6.3 Lateral mobility of receptors: consequences and modulators

BCR signaling depends on the formation and maintenance of microclusters by aggregation of BCR molecules and changes in lipid composition of the membrane that are likely to modulate BCR mobility. Overall BCR diffusivity is decreased in activated B cells compared with un-stimulated B cells and single BCR molecules are more likely to reduce their diffusivity when they encounter a BCR cluster [51]. Signaling-activation induced reduction in BCR diffusivity was confirmed using a photoactivatable antigen to precisely control the timing of B cell activation [52]. Cortical actin restricts the

mobility of BCR on resting cells as shown in Figure 1.7a, b. Latrunculin treatment, which inhibits actin polymerization, on un-stimulated B cells leads to an increase in diffusivity of BCR that is accompanied by signaling reminiscent of activation [35]. Pre-treatment of ligands for toll-like receptors (TLR) sensitizes BCR signaling, thus requiring lower levels antigen to activate B cells [46]. Treatment with TLR ligands also leads to increased BCR diffusivity, which is linked to the remodeling of actin by cofilin.

The reduction in BCR lateral mobility can also be due to interactions with other molecules during activation (see Figure 1.7c). The BCR and the kinase Lyn become spatially correlated after antigen stimulation and this correlation is accompanied by a reduction in diffusivity of both molecules [53]. Interestingly, the signaling co-receptor CD19 displays an overall slower diffusivity than BCR, which is not affected upon disruption of the actin cortex in resting B cells [35]. In contrast with the slower mobility of CD19, the inhibitory co-receptors CD22 and FcγRIIB display higher diffusivities than that of BCR in activated cells [54, 55]. CD22 is organized in nanoclusters and Inhibition of BCR signaling by CD22 is linked to its high mobility, which allows a single BCR to interact with multiple BCRs [54]. Once CD22 comes into contact with BCR the phosphorylation of its immunoreceptor tyrosine-based inhibitory motif by Lyn provides a docking site for the phosphatase SHP-1 [56]. The mobility of the receptor FcγRIIB is also associated with its inhibitory function; a mutation in its trans-membrane domain reduces its diffusivity and is associated with the autoimmune disease lupus [55].

19

All the studies mentioned above report overall changes of diffusivities under different conditions. Given the heterogeneity in the nanoscale configurations of BCR and its complex interactions with co-receptors and signaling molecules, is likely that BCRs reside in different signaling states, with distinct diffusive properties during activation. Thus, a different approach that accounts for such diversity is needed. In the second chapter of this thesis I introduce the use of a machine-learning algorithm to classify the trajectories of single BCR molecules into different diffusive states. Constitutive loss or acute inhibition of the Arp2/3 regulator, N-WASP, which is associated with enhanced signaling, increased the proportion of BCR trajectories with lower diffusivity. Furthermore, loss of N-WASP reduced the diffusivity of CD19, a stimulatory co-receptor, but not that of FcγRIIB [57]. Correct regulation of the lateral mobility of BCR and co-receptors is thus of great importance for proper immune responses.
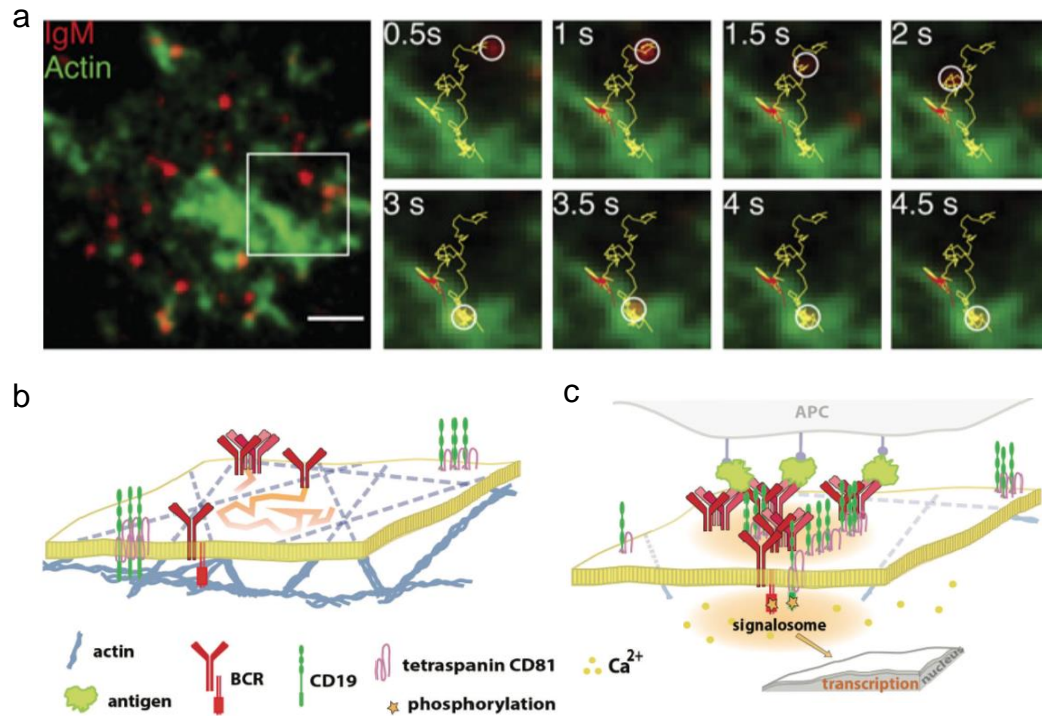
Figure 1.7. BCR mobility is modulated by actin cytoskeleton and by activation state. a) Snapshots of two-color TIRF imaging (Green F-actin, Red IgM BCR) showing the reduction in mobility of a BCR as it enters an actin-rich region. Scale bar is 1 μm. b) Cartoon depicting how BCR mobility and interaction with co-receptor CD19 is restricted by actin. c) After activation the BCR interacts with co-receptors and signaling molecules, which leads to a loss in mobility. Panel a was taken from [35]. Panels b and c were taken from [58]. Images used with permission.

1.7 Big things start small: The TCR and T cell activation

The cell-mediated response of the adaptive immune system requires efficient recognition of antigenic peptide for T cell activation. T cells sense the surface of

antigen presenting cells (APC) using small and dynamic protrusions called microvilli (Figure 1.8a) [59]. Peptide fragments are presented by the major histocompatibility complex (MHC I or II) receptor at the surface of APC [60]. T cells recognize antigen through the T cell receptor (TCR), which consists of a covalently bound α and a β polypeptide chain with a large extracellular part folded into two Ig-like domains – one variable and one constant [3]. The variable region corresponds to the antigen-binding site and its variability across T cells confers the adaptive immune system the capability of detecting a wide range of pathogens. The αβ heterodimer is non-covalently bound to CD3εY, CD3εδ and CD3ζζ dimers forming the TCR molecular complex.

The CD3 invariant chains contain ITAMs in their cytoplasmic region that are phosphorylated by lymphocyte-specific tyrosine kinase (Lck) upon TCR-MHC binding [61] as shown in Figure 1.8b,c. ITAM phosphorylation allows binding of the ζ-chain associated protein of 70 KD (Zap70), a cytoplasmic tyrosine kinase, and posterior phosphorylation of ZAP70 by Lck [62]. ZAP70 in turn, phosphorylates tyrosine residues in the cytosolic tail of the adaptor protein LAT (linker of activated T cells) and SH2 domain-containing leukocyte protein of 76 KD (SLP-76). LAT phosphorylation critically depends on actin polymerization by the formins mDia1 and mDia3 [63]. The assembly of SLP-76 and other microcluster associated proteins (see Figure 1.8c) leads to the recruitment and activation of phospholipase C (PLC) γ1 at the membrane. Once activated, PLCγ1 cleaves PIP2 into diacylglycerol and inositol triphosphate (IP3), which ultimately stimulates Ca^{2+} release, a hallmark of T cell activation and a

requirement for the initiation of gene transcription [64]. At different steps of the signaling cascade, actin remodeling and polymerization is induced, and is indispensable for the immune synapse formation, maturation and signaling regulation (see Figure 1.8c).
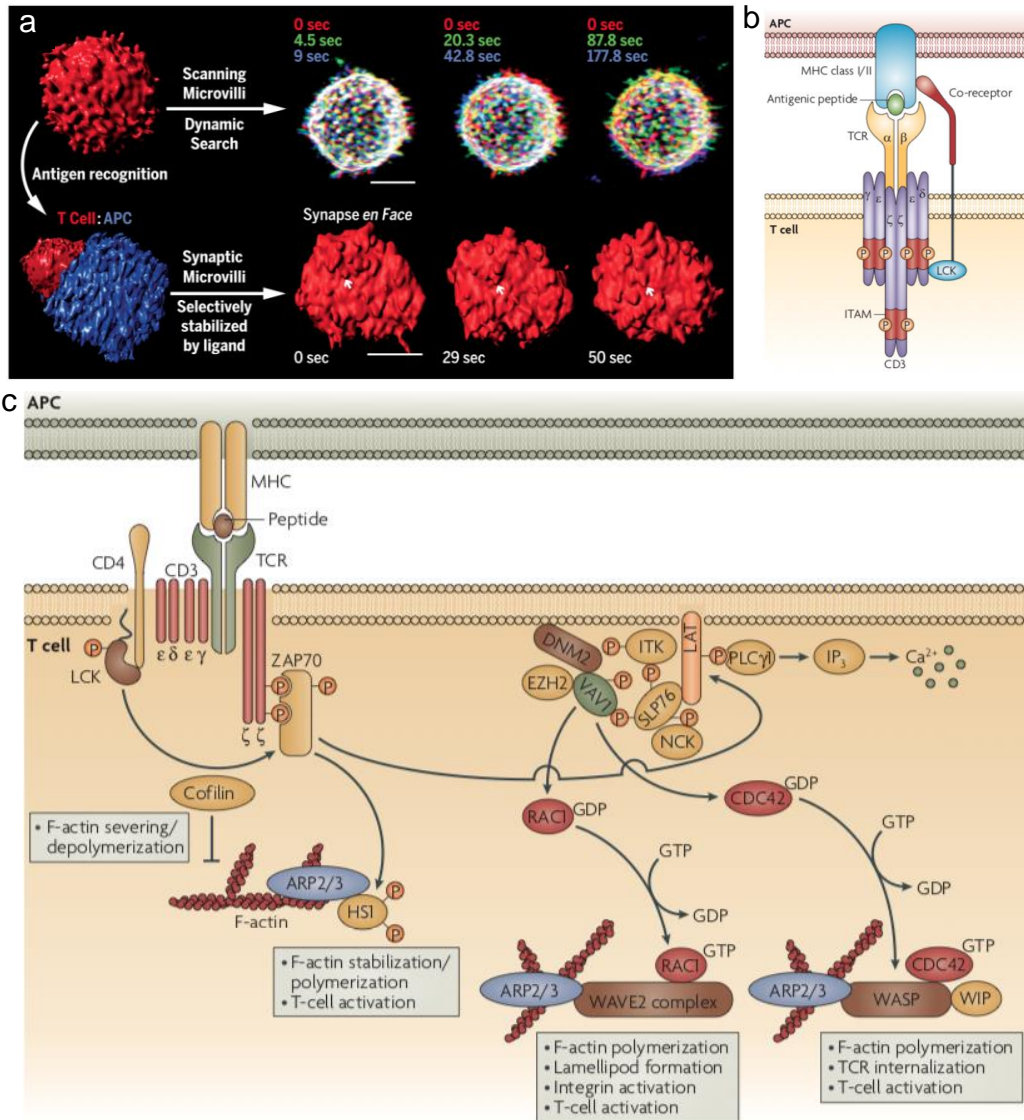
Figure 1.8. TCR structure, activation and signal propagation. a) Dynamic microvilli allow T cells to scan the surface of APCs, their fractal distribution permits consistent coverage across scales. Once microvilli engage with peptide-loaded MHC (pMHC) they become stabilized.   b) Schematic showing TCR-pMHC structure and binding. c) Signaling cascade originating from the binding of TCR to antigenic peptide. Panel a is from [59], panel b is from [65] and panel c is from [64]. Images used with permission.

1.7.1 Immune synapse formation: A macromolecular bull's eye pattern

The formation of the immune synapse (IS) starts with transient intercellular contacts between the T cell and the APC followed by the recognition and binding of surface expressed TCR with peptide fragments from pathogens bound to major histocompatibility complexes (pMHC) on the APC plasma membrane. This leads to the spreading of the T cell over the APC surface and further engagement through adhesion receptors, particularly the interaction between LFA-1 (leukocyte function-associated antigen 1) and ICAM-1 (intercellular adhesion molecule-1) [66, 67].

The TCR resides in nanoclusters of 35-70 nanometers in the resting cell [68, 69], starts to coalesce upon activation, and the newly formed microclusters are driven towards the center of the IS by actin retrograde flow [70, 71]. Centripetal movement of TCR microclusters leads to signaling attenuation as it disassociates from key adaptor molecules [72, 73]. As the cell spreads, actin is typically depleted at the center of the

24

contact zone. This actin depletion has a critical role in lytic granule secretion by cytotoxic T cells and secretion of cytokines by helper T cells [67, 74–76].

Due to the two-dimensional nature of the contact region between T cell and APC, the immune synapse is particularly suited for studies on planar substrates (stimulatory anti-CD3 coated glass and supported lipid bilayers), facilitating the use of high resolution fluorescence microscopy. The following IS description is based on studies of T cells interacting with stimulatory planar substrates. The accumulation of actin at the periphery of the IS and the accumulation of signaling microclusters at the center give rise to a bull's eye pattern that manifests as three concentric rings of membrane receptors with their underlying cytoskeletal and signaling proteins [71, 77, 78] as shown in Figure 1.9a. At the center lies the central supramolecular activation cluster (cSMAC), which concentrates the TCR and signaling co-receptors such as CD28. The next region is the peripheral SMAC (pSMAC) with integrins and sarcomeric-like acto-myosin structures. Lastly, the distal SMAC (dSMAC), which contains large ectodomain proteins, like CD45 and is characterized by a lamellipodial actin meshwork.

The actin cytoskeleton across the IS concentric regions is regulated by different regulatory proteins leading to the formation of actin networks with distinct morphologies. At the distal region (dSMAC), the actin ring is formed almost entirely by a branched actin meshwork nucleated by the Arp2/3 complex (see Figure 1.9b). The

assembly of this network drives the spreading of the T cell over the activating surface and is similar to the lamellipodium in crawling cells. The formation of this branched actin network occurs primarily by the recruitment and activation of the actin nucleation promoting factor (NPF) WAVE2, which promotes branched actin nucleation by Arp2/3 adjacent to the plasma membrane, driving cell spreading and actin retrograde flow [79–81]. This dense Arp2/3 nucleated network is largely disassembled at the dSMAC/pSMAC boundary, where the predominant actin structures are nucleated by formins of the Dia family. The peripheral region is rich in linear actin filaments generated mainly by the formin Dia1. Bipolar non-muscle myosin IIA filaments associate with these actin cables and organize them into a concentric structure [70] which functions as a contractile actomyosin network (Figure 1.9c). The actin arcs in the pSMAC region also contribute to the centripetal motion of TCR microclusters by a sweeping mechanism [70] and then disappear as they reach the central region (cSMAC). Actin structures at the cSMAC consist of actin foci embedded within both linear and branched filaments, but the overall actin density is highly reduced in this region. The role of these actin structures has been studied in cytotoxic T cells and natural killer cells, where their assembly helps regulate the release of lytic granules [82, 83]. Actin polymerization foci may also be found in the distal and peripheral regions [78]. These actin foci are assembled through WASP-mediated promotion of Arp2/3 nucleation and help amplify signaling activation [84]. Interestingly, actin dynamics vary in these different regions of the IS, with actin retrograde flow being fastest (~ 0.1 μm/s) at the distal region, slowing down at the peripheral region (~ 0.035 μm/s) and

26

finally, a complete loss of directed movement of actin features at the center [71, 85] (see Figure 1.9e, f).
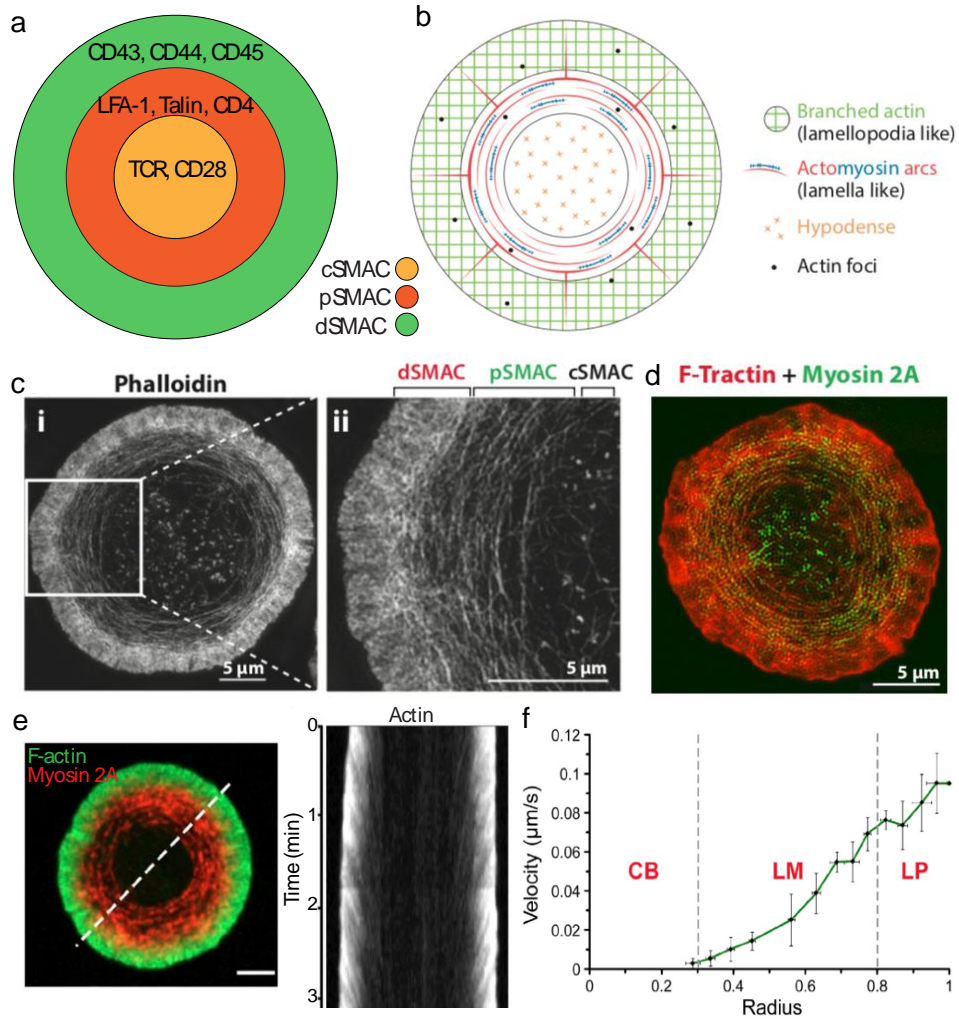
Figure 1.9. Two-dimensional architecture of the immune synapse. a) The three concentric regions that characterize the IS formation: dSMAC, pSMAC and cSMAC. b) Schematic showing the different types of actin networks at the T cell IS. c) TIRF-SIM images of Jurkat T cells fixed and stained with phalloidin to show the different

actin structures: foci, arcs and branched actin meshwork. d) TIRF-SIM image of a Jurkat T cell showing the overlap of actin and myosin 2A filaments at the peripheral region of the cell. e) Left panel: TIRF image of actin and myosin organization in a Jurkat T cell. Right panel: kymograph illustrating actin retrograde flows corresponding to the white dashed line on the left panel f) Distribution of F-actin velocity magnitudes across the IS radius for central body (CB), lamellar (LM) and lamellipodial (LP) regions. Panels a, b, c and d are adapted from [78]. Panels e and f are adapted from [85]. Images used with permission.

1.7.2 Centrosome repositioning at the IS: a coordinated effort

Along with the segregation of signaling and adaptor proteins at the immune synapse, the repositioning of the microtubule-organizing center (MTOC) towards the APC are hallmarks of T cell activation and required for sustained signaling. MTOC (or centrosome) translocation typically occurs within 3 to 6 minutes of TCR activation. The repositioning of the centrosome facilitates the directed delivery of lytic granules of CTLs towards target cells (Figure 1.10a), the recycling of TCR and LAT through vesicle delivery and the secretion of signaling molecules like interleukin-2 (IL-2)[75, 86–89].

Proper and timely translocation of the MTOC requires proper signaling propagation [86, 90] and reciprocal localization of the molecular motors dynein and myosin [91]. TCR activation and posterior phosphorylation of PLCϒ, which hydrolyzes PIP_2

28

yielding two second messengers IP$_3$ (the soluble headgroup) and diacylglycerol (DAG) the lipid remnant, leads to DAG accumulation at the IS. The localized accumulation of DAG induces the ordered recruitment of protein kinase C (PKC) which in turn drives the recruitment of dynein and redistribution of myosin (see Figure 1.10b). These molecular motors coordinate efforts with dynein pulling the centrosome towards the IS and myosin pushing it from behind [91]. Centrosome repositioning has also been described as a biphasic process. The first phase consists of a fast (~3.3 μm/min) polarization of the centrosome towards the IS and the second is a slow (~0.9 μm/min) docking phase, with this transition occurring within ~2 μm from the IS [75]. Interestingly, MTOC reorientation is independent of Arp2/3 mediated actin nucleation but requires the actin nucleating formins Dia1 and formin-like-1 (FMNL1) [92, 93].
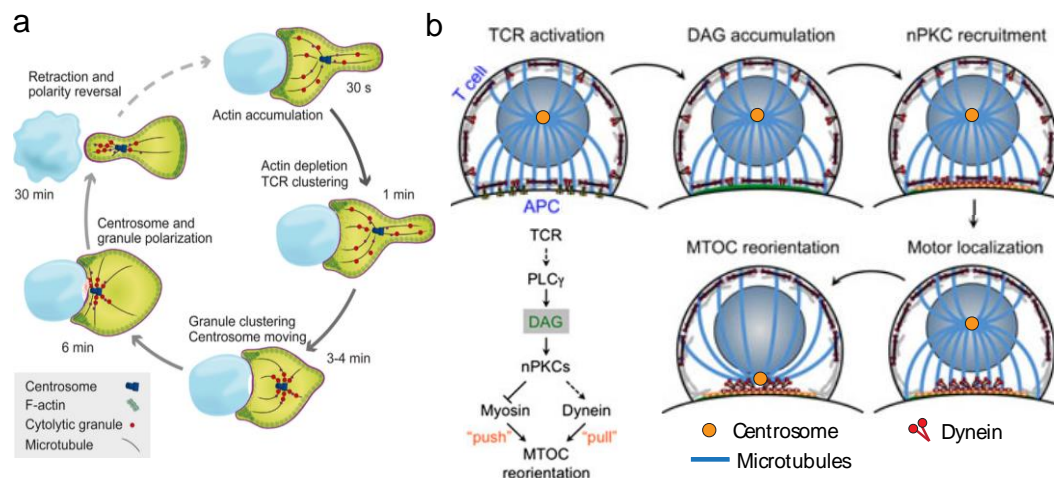
Figure 1.10. Centrosome translocation during IS formation. a) Sequence of events that lead to centrosome repositioning and granule secretion for cytotoxic T lymphocytes (CTLs). b) Schematics of the different steps involved in MTOC

reorientation. Panel a is from [89] and panel b is from [88]. Images used with permission.

1.7.3 Cytoskeletal crosstalk during the T cell immune synapse formation

The actin and microtubule cytoskeleton are essential for a large number of cellular processes. These cytoskeletal systems have been extensively studied in a variety of cellular contexts and it has become increasingly evident that their functional dynamic properties are often intertwined. Many proteins contain domains that allow direct binding to these filaments, or to regulators, thus mediating many of the interactions between actin and microtubules. Several of the ways in which actin and microtubules interact are described in Figure 1.11 a-e. Growing microtubules can be captured and guided along actin bundles through the interaction of actin-microtubule crosslinkers and microtubule end binding proteins [94]. Microtubules can be anchored and stabilized at the actin cortex through protein complexes, as is the case for the dynein-dynactin complex which plays a role in centrosome repositioning at the immune synapse [86]. Actin can also act as a physical barrier for microtubule growth. Disruption of the actin cortex with high doses of the actin polymerization inhibitor Latrunculin-A leads to microtubule bundling and long microtubule filaments protruding outside the cell [95]. Furthermore, interactions between microtubule associated proteins and actin regulators can lead to coordination between the two systems. For example, a protein complex of the plus TIP protein CLIP170 and the formin mDia1 promotes actin polymerization from microtubule plus ends [96].
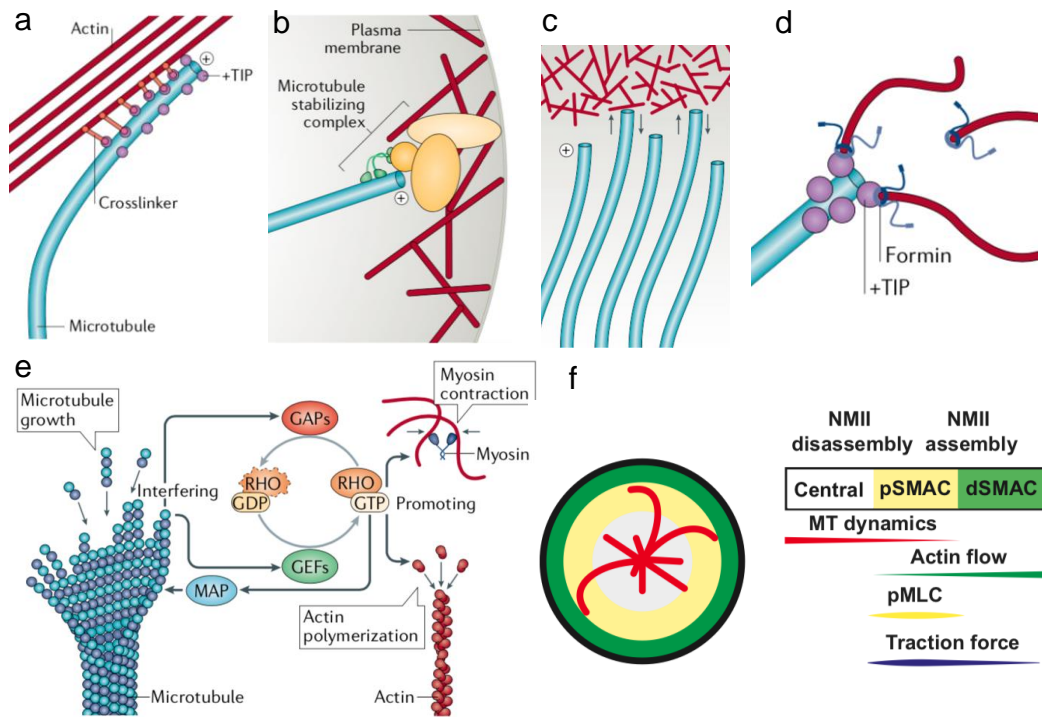
Figure 1.11. Microtubule and actin cytoskeleton crosstalk. a) Microtubule growth can be guided along actin fibers through interaction of +TIP and crosslinking proteins. b) Microtubules can be anchored and stabilized at the actin cortex through molecular complexes. c) Actin can act as a physical barrier for microtubule growth. d) The actin nucleator formin can associate with growing microtubules leading to microtubule-mediated stimulation of actin polymerization. e) Members of the family of RHO GTPases regulate both actin and microtubule dynamics. f) In T cells the higher density and dynamics of microtubules at the center regulate the contractile forces produced by actomyosin cytoskeleton. Panels a-e taken from [97]. Panel f taken from [98]. Images used with permission.

Actin and microtubules share regulators of their dynamics. Rho GTPases are proteins that regulate the dynamics of these cytoskeletal systems through their interactions with actin and microtubule associated proteins. Additionally, microtubules can contribute to regulation of actin dynamics by their influence on Rho activity. At the T cell immune synapse the microtubule density and dynamics is higher at the center and decreases towards the periphery where actin and myosin dynamics and concentration are higher. Thus MT-mediated suppression of RhoA activation regulates spatially the traction forces generated by T cells (see Figure 1.11 f) [98]. During the immune synapse formation the centripetal motion of TCR microclusters is produced by actin retrograde flow and actomyosin contractile arcs and is aided by TCR directly associated dynein motors walking along microtubule filaments [70, 99].

In the third chapter of this thesis I aim to elucidate the interactions between microtubules and actin at the immune synapse through high-resolution fluorescence microscopy of Jurkat T cells, using microscopy techniques described in Appendix A. In particular, I investigate the role of Arp2/3 and formin generated actin structures on MT growth and dynamics. I find that formin inhibition leads to a decrease in microtubule growth rates and that this effect is enhanced by integrin engagement. Interestingly Arp2/3 inhibition leads to a small increase in MT growth rates suggesting that actin networks nucleated by Arp2/3 act as a physical barrier that slows MT growth. I also find that microtubule filaments are more highly deformed and dynamic in the peripheral actomyosin rich region of the cell-substrate contact compared to the central

actin-depleted zone. Inhibition of formin and Arp2/3 as well as ROCK kinase resulted in decreased deformations of MT filaments suggesting that actin dynamics and actomyosin contractility play an important role in defining MT shapes.

Chapter 2: WASP family proteins regulate the mobility of the B cell receptor during signaling activation

The contents of this chapter have been published in the journal Nature Communications [57]. I was the main person involved in experimental design, sample preparation, data collection, image processing and data analysis, and writing of the manuscript.

2.1 Introduction

B cells are an important component of the adaptive immune system. B cells sense antigen using specialized receptors known as B cell receptors (BCRs) that trigger signaling cascades and actin remodeling upon binding antigen on the surface of antigen presenting cells (APC) [40, 58, 100]. Signaling activation results in spreading of the B cell on the APC surface leading to the formation of a contact zone known as the immunological synapse [101]. Antigen crosslinking aggregates BCRs in lipid rafts, enabling lipid raft-resident Src kinase to phosphorylate their immunoreceptor tyrosine-based activation motifs (ITAMs) [19, 43, 102]. Signaling BCRs assemble into microclusters, which grow via movement of BCRs and their incorporation into these microclusters [40, 103]. BCR clustering is dependent on the probability of receptor-receptor interactions at the plasma membrane [51], and is in part dictated by the lateral mobility of receptors. Thus, elucidating the mechanisms that regulate BCR movement in the cell membrane is critical for understanding BCR signaling.

The cortical actin network in cells is known to form juxtamembrane compartments that can transiently confine the lateral movement of membrane proteins [104–106], including BCRs in B cells [107]. Treanor et al.[107] showed that in unstimulated B cells, inhibition of actin polymerization leads to an increase in lateral diffusivity of BCR and is accompanied by signaling that is reminiscent of activation. The transient dephosphorylation of ezrin and actin depolymerization induced by BCR-antigen interaction results in the detachment of the cortical actin from the plasma membrane concurrent with a transient increase in the lateral movement of surface BCRs [108]. Activation of Toll-like receptors sensitizes BCR signaling, by increasing BCR diffusivity through the remodeling of actin by cofilin, an actin binding protein that disassembles actin filaments [46]. The sub-membrane actin cytoskeleton also modulates the concentration of inhibitory co-receptors [54, 55] in the vicinity of BCR microclusters, thereby ensuring the rapid inhibition of activated BCRs.

A consensus picture that emerges from these studies is that in resting B cells, the actin network serves as a structural barrier for BCRs, regulating their mobility by steric interactions. Beyond this structural role, considerable evidence points to a role for dynamic actin in regulating BCR signaling and activation. Our previous work has shown that inhibition of actin polymerization by low concentrations of Latrunculin A following antigen stimulation inhibits the growth of BCR microclusters [36], suggesting that actin dynamics plays a direct role in modulating BCR mobility. Furthermore, actin regulatory proteins are known to regulate signaling and have been

35

implicated in the control of microcluster formation. Wiskott Aldrich Syndrome protein (WASP) and Neural-WASP (N-WASP) are scaffold proteins which are activated downstream of BCR activation. They link receptor signaling to actin dynamics through the activation of the Arp2/3 complex to promote the growth of branched actin networks [109–111]. Liu et al. [50] found that N-WASP plays an important role in the deactivation or attenuation of BCR signaling. B cells from N-WASP conditional knockout mice exhibit delayed cell contraction and sustained signaling compared to control cells. However, these studies have largely focused on changes in the dynamics of cell spreading and BCR microcluster movement and coalescence on a global cell-wide scale. Whether and how actin dynamics directly modulate nanoscale BCR diffusion and signaling and the role of actin regulatory proteins in this process remain open questions [31].

Here, we used single molecule and super-resolution imaging to investigate the diffusive properties of the BCR, its stimulatory co-receptor, CD19, and its inhibitory co-receptor FcγRIIB [112, 113]. It is important to note that the diffusivities observed here are not entirely thermally driven (see Appendix B for more details). To obtain a better understanding of the diffusive properties of these receptors, we used a statistical algorithm to classify single molecule trajectories into states with distinct diffusivities and correlate these with potential signaling states. We used small molecule inhibitors of actin nucleators and regulators as well as B cells from WASP and conditional N-WASP knockout mice to investigate how altered actin dynamics manifest differences

36

in BCR signaling and diffusivity. We found that BCR and CD19 molecules had an overall lower diffusivity when actin dynamics were inhibited or WASP family proteins were inhibited or deleted. This reduction in diffusivity was due to a change in the proportion of receptors with low mobility. However, FcγRIIB receptors did not show a difference in diffusivity or state distribution upon inhibition of actin nucleators, suggesting that the effect of actin dynamics on BCR and CD19 mobility is not global for all membrane proteins during B cell activation. We found that inhibition of WASP family proteins also reduces actin flows, suggesting that the effect of WASP family proteins or downstream effectors on BCR mobility is actin mediated. Our findings reveal a role for actin dynamics in modulating nanoscale receptor diffusion, highlighting the importance of the dynamic actin network in regulating receptor mobility and signaling.

2.2 B cell receptor motion spans a wide range of diffusivity

Primary murine B cells were allowed to spread on a supported lipid bilayer coated with mono-biotinylated Fab' fragment of BCR-specific antibody (mbFab) that induces BCR. We used Interference Reflection Microscopy (IRM) to visualize the spreading and contraction of B cells on supported lipid bilayers (Figure 2.1a, top panels), and total internal reflection fluorescence (TIRF) microscopy to analyze the clustering of BCR and coalescence of BCR clusters during cell contraction (Fig. 1a, bottom panels). B cell receptor diffusivity was extracted from single molecule imaging of BCR trajectories obtained by TIRF imaging (Figure 2.1b-d). We verified that B cells

underwent signaling activation in our experimental conditions by labeling with phosphotyrosine as well by quantifying the intensity increase of BCR clusters due to coalescence (Figure 2.9 - Supplementary material). To label the BCR, Alexa Fluor (AF) 546 labeled mbFab was added to the imaging medium at low concentrations (<1 μM) so that only single molecules were detected [114]. Cells were imaged from the moment they contacted the bilayer and time-lapse movies (1000 frames at 33 Hz) were recorded. Figure 2.1c shows a representative frame of single BCR molecules in TIRF and the cell outline obtained from an interference reflection microscopy (IRM) image taken immediately after the time-lapse movie. Single molecules detected in each frame were localized with high precision (~20 nm) and linked frame by frame to generate tracks [115]. Only single molecules identified within the IRM based cell contour are taken into consideration. A representative compilation of the tracks obtained from a single cell during a 10-minute period is shown in Figure 2.1d. The tracks are color coded for short-time diffusivity, calculated using the covariance-based estimation method developed by Vestergaard et al [116]. The covariance-based estimator (CVE) is unbiased and does not need a regression analysis to estimate diffusion coefficients. Therefore, this method is ideal for obtaining diffusion coefficients from short single particle trajectories. The cumulative distribution of diffusion coefficients measured across the population of tracks show variation in diffusivity over several orders of magnitude. These results indicate that BCR exhibit a wide spectrum of diffusivities, which may be indicative of their signaling properties and their biochemical state. Moreover, we found that there was a larger proportion of BCR with higher mobility in

the first minute compared to later time points (Figure 2.1e), which is consistent with the onset of signaling [52]. This is reflected in the comparison of the diffusivity distributions measured at the indicated time points which shows that the diffusivity at minute 1 was significantly higher than at subsequent time points (Figure 2.1f). In contrast, B cells in contact with transferrin-tethered bilayers (non-activating control) exhibited an overall higher BCR diffusivity throughout the imaging period and did not show a progressive reduction over time (Figure 2.10a – Supplementary material)
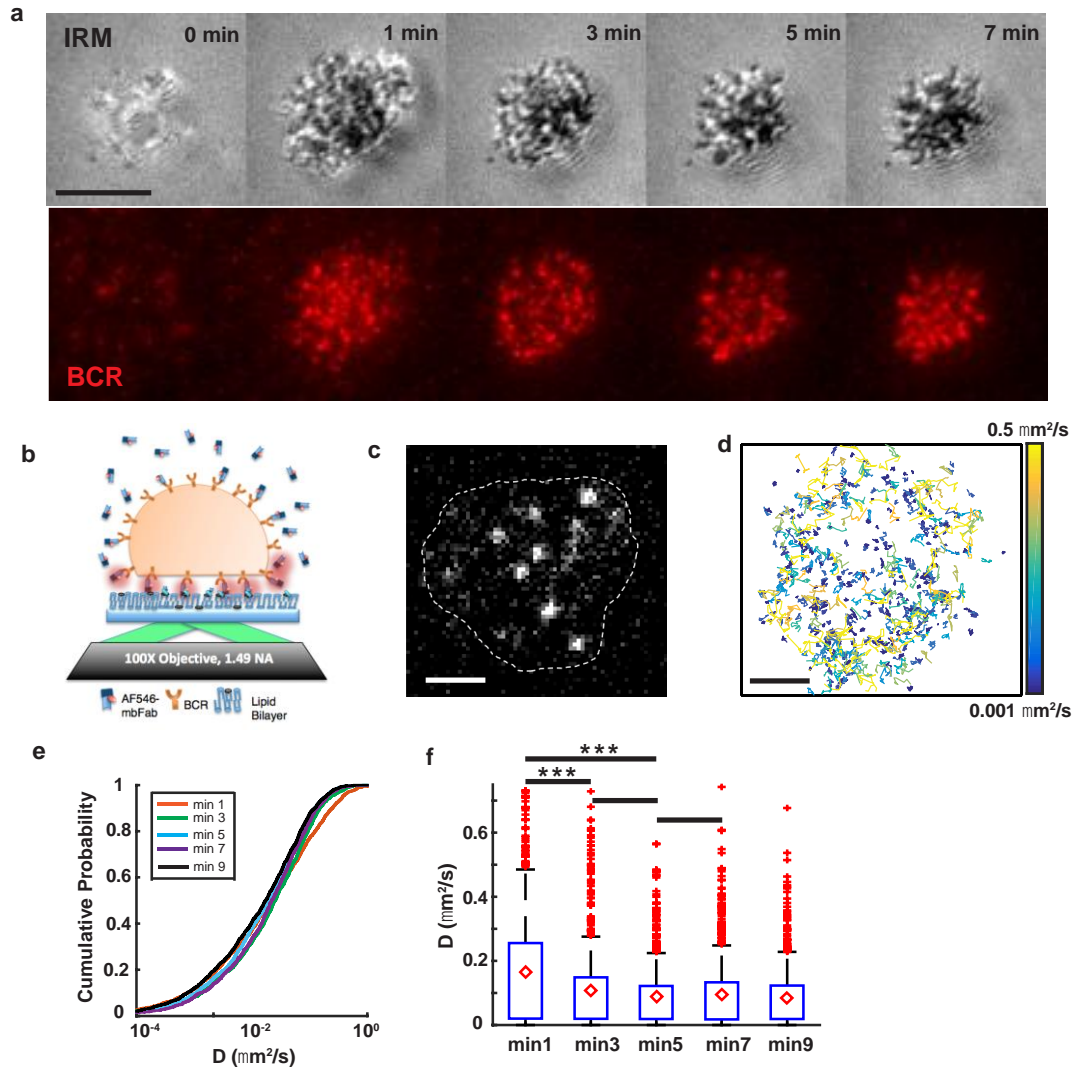
Figure 2.1. Single particle tracking reveals wide range of BCR mobility. **a)** Panel showing primary murine B cell spreading with IRM (above) and BCR clustering (TIRF, below). Scale bar is 3 μm. **b)** Experimental schematic, indicating activated murine primary B cells, placed on supported lipid bilayers coated with mono-biotinylated fragments of antibody (mbFab). Cells are imaged in TIRF mode and the concentration of AF546 labeled mbFab is kept low enough to image single molecule events. **c)**

40

Representative TIRF image with the bright dots representing single BCR molecules. The cell contour is obtained from an IRM image taken after TIRF imaging. Scale bar is 1 μm. **d**) The collection of tracks obtained for a control cell during a 10-minute period. The tracks are color-coded for diffusivity. Scale bar is 1 μm. **e**) Cumulative distribution function for the diffusivities measured at 1, 3, 5, 7 and 9 minutes after activation for BCR in B cells from control mice. **f**) Boxplot showing BCR diffusivities at the indicated time points where the mean is marked with red diamonds (N = 15 cells). Significance of differences was tested using the Kruskal-Wallis test *(***p < 0.001*; min 1 vs min 3, P = 0.0008; min 1 vs min 5*, p = 0.000038*; min 3 vs min 5*, p = 0.1767*; min 5 vs min 7*, p = 0.8614*).

2.3 Perturbation-Expectation Maximization analysis identifies distinct diffusive states for BCR

In order to obtain a better understanding of the diffusive properties of BCR, we employed a systems level classification algorithm, Perturbation-Expectation Maximization (pEM), which uses machine learning to extract the set of distinct diffusive states that best describes a diffusivity distribution [117, 118]. The premise underlying pEM is that various biochemical interactions of a protein lead to a finite number of distinct diffusive behaviors (diffusive states). pEM then determines the number of diffusive states in an unsupervised, statistically-correct fashion using the Bayesian Information Criterion (see Methods section for a more detailed rationale). Here, we used pEM-v2, which is a pEM version capable of accounting both for non-

41

normal diffusive modes and for the high heterogeneity of the cell membrane environment by splitting the trajectories into shorter segments and then identifying transitions between different diffusive states from one segment to the next. All the single molecule trajectories obtained were split into 15 frame segments and the classification analysis was performed on the set of all of these 15-frame-long tracks. pEM analysis of all BCR trajectories from B cells identified 8 distinct states, revealing a far greater complexity of diffusive behavior than is apparent from approaches that average over all tracks or that impose two diffusive states only [46]. A number of representative trajectories assigned to each of these states are shown in Figure 2.2a in a 1.5×1.5 μm^2 window.

In control cells, all the 8 states displayed simple diffusion, as the ensemble mean square displacement (eMSD) plot of each state was linear (Figure 2.2b). The mean diffusivity for all time points considered for each of these 8 states is shown in Figure 2.2c. For all states, the representative mean diffusivity was preserved over time. For each time point, we also calculated the fraction of tracks assigned to each state - the population fraction (Figure 2.2d). The population fraction of the fastest moving state, state 8, rapidly decreases within the first few minutes and then stabilizes. This corresponds to the decrease in diffusivity for the higher mobility fraction as seen in the cumulative distribution function in Figure 2.1e. The population fraction corresponding to most of the other states fluctuate over time but do not show a clear trend. To validate that these low mobility states resulted from BCR activation, we performed pEM analysis of single

42

molecule BCR trajectories for cells on transferrin-tethered bilayers. In B cells interacting with lipid bilayers through the transferrin receptor, there was a near complete loss of BCR trajectories in the lowest mobility states (States 1 and 2), while the population fractions of the fast mobility states (States 5-8) were higher than those in B cells interacting with lipid bilayers through the BCR (Figure 2.10b, c – Supplementary material).

In order to quantify the spatial distribution of the trajectories, the first position of each non-redundant trajectory (for each distinct particle) was used to compute the spatial pair correlation function as a function of distance, $g(r)$, between the localized spots (Figure 2.2e) [119]. $g(r)$ measures the normalized probability of finding a second localized fluorophore (initial point of a trajectory) at a given distance, r, from an average localized fluorophore. For the resulting curves, a value of 1 indicates that the receptors that occupy a given state are randomly organized, whereas values > 1 denote a higher probability of finding receptors in a given state at shorter distances, indicative of clustering. The range r over which $g(r) >1$ denotes the scale of clustering. To calculate the pair correlation functions from our data, we combined the trajectories belonging to pairs of states that are closest in diffusivity (e.g. States 1 and 2; States 3 and 4 and so on). We see from Figure 2.2e that the lowest mobility states, States 1 and 2, display $g(r)$ that is significantly larger than 1 for small values of r, suggesting that these trajectories are significantly more densely clustered compared to those of the other states. States 3 and 4 show a very small degree of clustering, while the other

43

higher mobility states display a largely homogeneous distribution. Of note, the slowest

diffusive states, States 1 and 2, appear to be the ones that correspond to BCR in clusters.
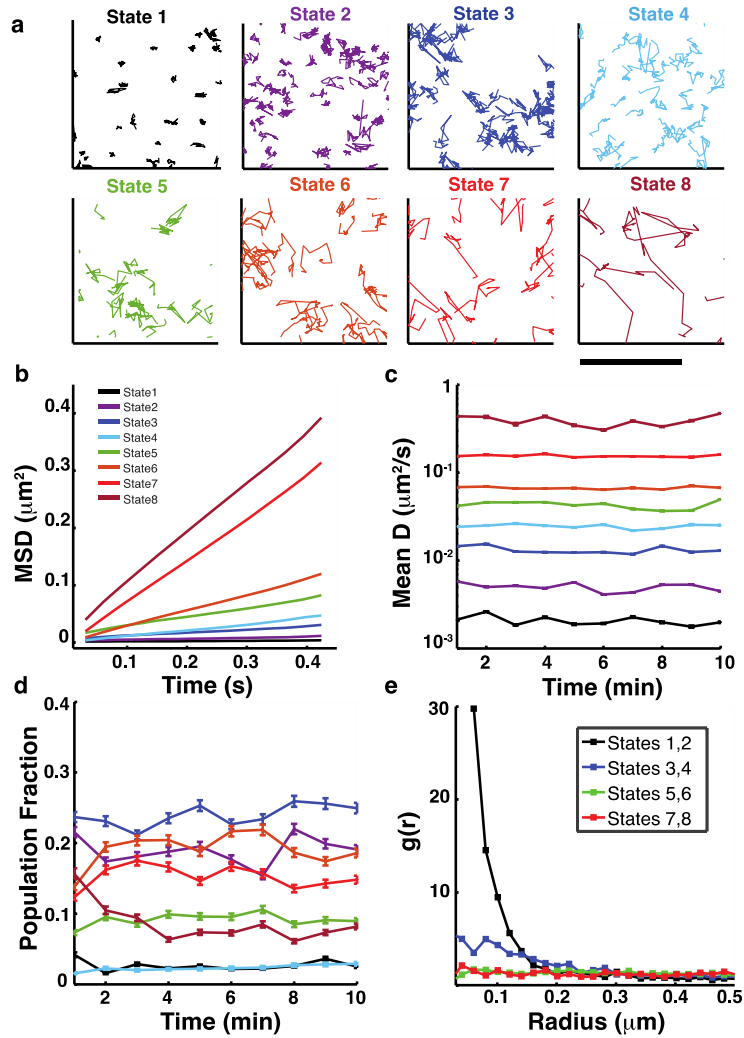
Figure 2.2. Perturbation Expectation Maximization analysis identifies eight distinct diffusive states for BCR in control cells. a) Characteristic tracks belonging to each of the BCR diffusive states identified by pEM. Diffusivity increases from state 1 (slowest) to state 8 (fastest). Scale bar is 1 μm. b) Ensemble mean square

displacement (eMSD) plots for each of the states. Colors corresponding to different states are as shown in the legend. The same color scheme is used for all subsequent figures. (N = 15 cells). c) Plot showing the mean diffusivity for the trajectories belonging to each state at every time point. Error bars represent the standard error of the mean. d) Plots showing the fraction of BCR tracks that are sorted in each state at every time point. Error bars represent a confidence interval of 95% on the population fraction calculation. e) Plot of pair correlation as a function of distance for all states.

2.4 Actin nucleating proteins regulate BCR mobility

In order to investigate how BCR diffusivity is modulated by actin dynamics, we studied the effect of small molecule inhibition of the two dominant actin-nucleating pathways on BCR diffusivity in activated B cells. Addition of CK666 (50 µM), a small molecule inhibitor of the Arp2/3 complex resulted in a decrease in the mobility of surface BCRs as compared to untreated cells (Figure 2.3a). We next investigated the effect of inhibiting formin, an actin nucleating protein that polymerizes bundled actin, on BCR mobility. B cells treated with the formin inhibitor, SMIFH2 (25 µM) also had BCR with lower mobility as compared to untreated cells (Figure 2.3a). The reduction in overall BCR diffusivity caused by formin inhibition was similar to that caused by Arp2/3 inhibition. pEM analysis was performed on the set of BCR tracks from cells treated with these inhibitors. Plots of the population fraction over time of BCRs in B cells treated with CK666 showed that the low mobility states, States 2 and 3, contribute to over 60% of all trajectories, compared to 40% in DMSO-treated control cells (Figure

45

2.3b, f). The distribution of population fractions for cells treated with SMIFH2 showed a slightly different behavior (Figure 2.3c, f), wherein only State 2 displayed an overall increase (35% of all trajectories) relative to non-treated controls (20% of all trajectories). The growth of branched actin networks by Arp2/3 requires its activation by the WASP family proteins. We next asked how inhibition of these actin regulators affects BCR diffusion by treatment with wiskotatin, an inhibitor of WASP family regulators. We found that application of wiskostatin (10 μM) resulted in a decrease in BCR diffusivity (Figure 2.3d) and an increase in the population fraction of BCRs in States 1 and 2 (Figure 2.3e, f). Overall, we found that inhibition of actin-nucleating proteins, Arp2/3 and formin, as well as upstream regulators reduced BCR diffusivity, along with an increase in the population fraction of the slow diffusive states as compared to DMSO-treated control cells. These results collectively implicate actin dynamics in maintaining the heterogeneity of BCR mobility and nanoscale organization.
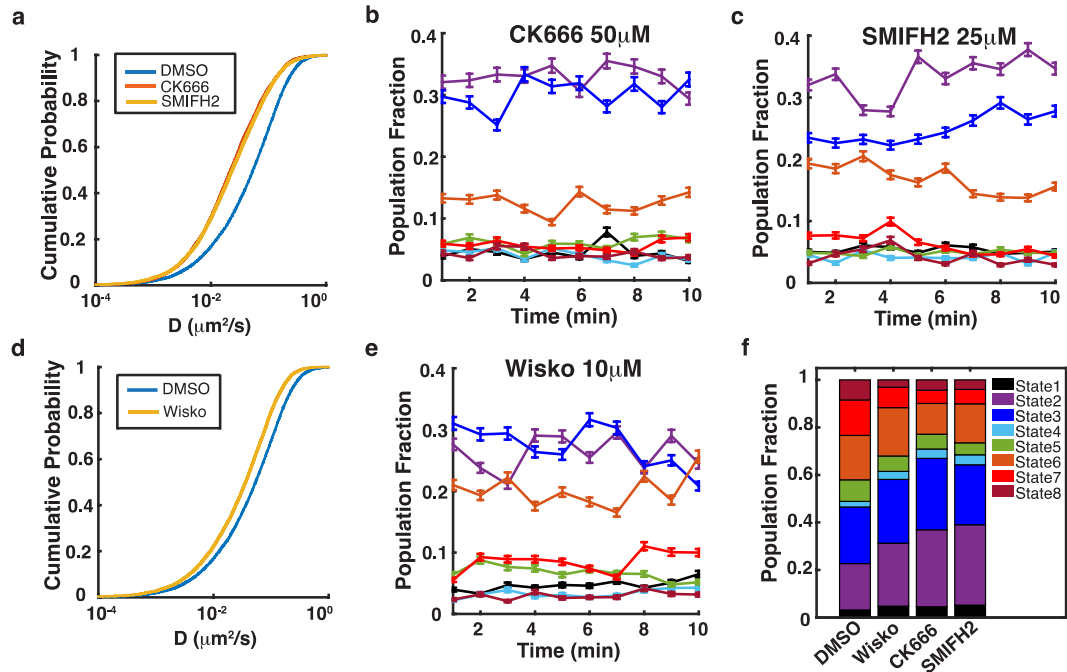
Figure 2.3. Inhibition of actin nucleation decreases BCR diffusivity. a) Plots of BCR diffusivity distributions for cells treated with CK666 (inhibition of Arp2/3 complex) or SMIFH2 (inhibition of formins). (*p* < 0.001, Kruskal-Wallis test for comparison between DMSO and CK666, or DMSO and SMIFH2). **b)** Population fraction over time for cells treated with CK666. **c)** Population fraction over time for cells treated with SMIFH2. **d)** BCR diffusivity distribution for cells treated with wiskostatin (Wisko) compared to DMSO control. *(p* < 0.01, Kruskal-Wallis test for comparison between DMSO and Wisko) **e)** Population fraction over time for cells treated with wiskostatin. Error bars in b, c and e represent a confidence interval of 95% on the population fraction calculation. **f)** Overall distribution of population fractions for cells treated with wiskostatin, CK666 and SMIFH2 (Number of cells: DMSO, N = 14; Wisko, N = 11; CK666, N = 10; SMIFH2, N = 16).

2.5 WASP family proteins modulate B cell receptor diffusivity

B cells, like all immune cells, express the hematopoietic-specific Arp 2/3 regulator, WASP as well as ubiquitous N-WASP. These two proteins have high homology and share many overlapping functions but N-WASP and WASP have distinct effects on B cell spreading, BCR signaling and microcluster formation [50]. Therefore, to test how WASP family regulators affect nanoscale BCR diffusion, we utilized B-cell–specific conditional N-WASP KO mice (cNKO) and WASP KO mice (WKO). We used the same single molecule imaging strategy to obtain tracks of single BCR over time as shown for cNKO cells in Figure 2.4a. The different track colors correspond to tracks with different diffusivity and show a preponderance of tracks with lower diffusivity (blue) as compared to BCR tracks in control cells. However, the decrease in diffusivity for the high mobility tracks in the first few minutes that was observed for control cells is not evident for BCR molecules in cNKO cells (Figure 2.4b).

To determine whether the differences in BCR diffusivities between control and cNKO cells are related to the known differences in BCR signaling in these two conditions, we used pEM analysis to assign BCR trajectories to diffusive states in cNKO B cells. The data containing the trajectories of BCR from control and cNKO cells was analyzed together and 8 different states were identified, as for the control case. Plots of the population fraction of BCR in cNKO cells as a function of time are shown in Figure 2.4c. The fraction of BCR in each state shows little change over time, and the eMSD

48

of every state displays simple diffusion in cNKO B cells (Figure 2.11 – Supplementary material). Figure 2.4d shows the pair correlation function plots of all states in cNKO cells. Similar to control cells, States 1 and 2 display clustering, States 3 and 4 show a somewhat non-homogeneous distribution, while the higher mobility states have a homogenous distribution.

Given that the diffusivity remains largely unchanged for times beyond 5 minutes in both types of cells, we compared the cumulative distribution of diffusion coefficients measured for times between 5 and 10 minutes for control and cNKO cells. We found that BCR in cNKO cells display much slower diffusivity than control cells (Figure 2.4e). This is also evident from the trajectories, which show a greater occurrence of tracks with lower diffusivity (blue color-coded tracks, in Figure 2.4a, compared to Figure 2.1d). We found that, similar to control B cells, the lower mobility states, States 1-3 are the most dominant states in cNKO cells. We next compared the population fractions (pooled across time) of the occupied states for control and cNKO cells. We found significant differences (see Table 2.1 – Supplementary material) in the population fractions between control and cNKO cells, with a significantly larger proportion of trajectories occupying the lowest mobility states (States 1-3) in cNKO cells (Figure 2.4f).

We next examined how WASP regulates nanoscale BCR mobility, by single molecule imaging of BCR in B cells from WKO mice to obtain BCR trajectories (Figure 2.12a – Supplementary material). We found that WASP deletion results in a reduction of

BCR diffusivity as shown by the CDF of diffusivities (Figure 2.4e). pEM analysis of BCR single molecule tracks in WKO B cells again led to the identification of 8 distinct states similar to control and cNKO cells, with the population fraction of each state not changing significantly over time (Figure 2.12b – Supplementary material). Pair correlation analysis of tracks again showed States 1 and 2 as being the most clustered (Figure 2.12c – Supplementary material). However, pEM analysis revealed qualitatively significant differences in the diffusive states between WKO and cNKO B cells. We found that WKO B cells had similar population fractions of States 1 and 2 as control B cells, unlike cNKO B cells (Figure 2.4f). This indicates that WASP and N-WASP have differential effects on the mobility and putative signaling states of BCR. Taken together, the predominance of lowest mobility states of BCRs in activated B cells and the increase in these lowest mobility states in cNKO B cells which have been shown to have higher levels of BCR signaling than control B cells, are consistent with a model in which the lower diffusivity of BCR corresponds to its signaling, clustering and activation state.

In addition to identifying diffusive states, pEM analysis can also determine the transitions between these states along individual trajectories (Figure 2.13a, b – Supplementary material). We thus selected longer tracks (>30 frames) and identified the state(s) to which the sub-tracks had been assigned and quantified the frequency of transitions from a given state to different states (Figure 2.13b-c – Supplementary material). We found that BCRs tend to remain in their current states or switch to an

50

adjacent one. BCR molecules in the three slowest diffusive states were the most stable in both control and cNKO cells, showing the least transition probability to other states. These observations suggest that fast diffusive particles will be more likely to encounter a cluster and be incorporated into it, thereby transitioning into the neighboring slower state. BCRs in cNKO cells showed an overall trend to transition towards slow diffusive states, especially towards States 2 and 3 (Figure 2.13c – Supplementary material). In addition, particles in fast diffusive states were less stable and transitioned into slower states more frequently in cNKO than in control cells. This result is consistent with the higher population fraction of BCR in slow diffusive states in cNKO cells.
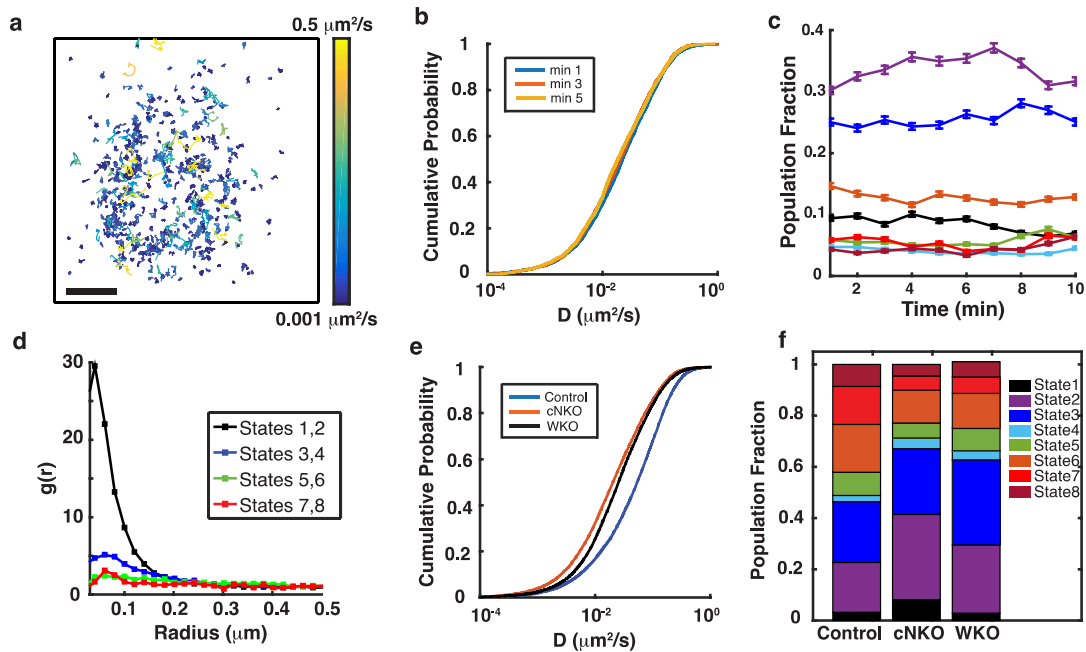
Figure 2.4. N-WASP knockout leads to predominance of BCR molecules in lower mobility diffusive states. a) Collection of tracks obtained from pEM analysis of BCR

molecules in a cNKO cell during a 10-minute period. The tracks are color-coded for diffusivity. Scale bar is 1 μm. **b)** Cumulative distribution function for diffusivities measured at 1, 3 and 5 minutes after BCR stimulation in B cells from cNKO mice. **c)** Plots of population fractions of eight distinct diffusive states as a function of time for BCR in cNKO cells. Error bars represent a confidence interval of 95% on the population fraction calculation. The colors corresponding to the different states are as shown in Figure 2b. **d)** Pair correlation function plots of the trajectories in different diffusive states for cNKO cells. **e)** The distribution of diffusivities from the 5-10 minute time period after activation, for BCR in control, WKO and cNKO cells. The distributions for control are significantly different from WKO and cNKO cells (control cells N = 15, WKO cells N = 21 cells, $p < 0.001$ and cNKO cells N = 17, $p < 0.0001$ Kruskal-Wallis test). **f)** Comparative population fractions for BCR in different states over the entire time period in control, WKO and cNKO cells. Significance levels for the differences are in Table 2.1.

2.6 N-WASP modulates the diffusivity of the stimulatory co-receptor CD19 in activated cells

To better understand the nature of the BCR diffusive states that were enhanced in cNKO activated cells, we next investigated how the diffusivity of CD19, a stimulatory co-receptor [120], is affected by the lack of N-WASP. CD19 is recruited to the BCR upon antigen binding, which enhances BCR activation. A previous study using super-resolution imaging found that in resting B cells, CD19 resides in nanoclusters separated

52

from IgM BCR nanoclusters, while in activated B cells, CD19 and BCR nanoclusters are colocalized [26, 27]. Thus, single molecule studies of CD19 have the potential to reveal additional insight into signaling BCR states. We used instant Structured Illumination Microscopy (iSIM) [44] which enables super-resolution imaging with a lateral resolution of 145 nm and an axial resolution of 350 nm to simultaneously image CD19 and BCRs. Consistent with previous reports, CD19 and BCR microclusters co-localized to within our resolution limit of 140-150 nm in activated B cells (Figure 2.5a, b, Figure 2.14a – Supplementary material). Furthermore, these microclusters moved together towards the center of the contact zone (Figure 2.14b – Supplementary material). To identify the diffusive states in which CD19 resides, we performed single molecule imaging of CD19 using AF594 labeled anti-CD19 antibody at low labeling concentrations and with the same methods as for single molecule imaging of BCR. By analyzing a collection of CD19 tracks in a control cell during the 10-minute imaging period (Figure 2.5c), we found that the diffusivity of CD19 is lower than that of the BCR, given the abundance of short tracks (blue) and fewer longer tracks (yellow) (compared to Figure 2.1d). pEM analysis of CD19 tracks again resulted in eight distinct states with mean diffusivities preserved over time (Figure 2.5d). The pair correlation analysis of CD19 molecules in both control and cNKO cells show higher correlations of States 1 through 4 at shorter distances than the other states, indicative of a clustered configuration (Figure 2.5e, f). As observed for BCRs, trajectories from States 1 and 2 of CD19 show the highest degree of clustering at short distances, while the faster moving states show a more homogeneous distribution.

Interestingly, the cumulative distribution plots of the diffusivities showed that CD19 diffusion in cNKO cells is significantly lower than in control cells (Figure 2.5g). The diffusivities of the eight states found for CD19 were very similar to those found for BCR, allowing us to compare the population fractions of these states between these two receptors (Figure 2.5h). States 1, 2, 4 and 8 are more predominant for CD19 while States 3, 6 and 7 are more populated for BCR in control cells. The population fraction of the lowest mobility states (States 1 and 2) for CD19 show a significant increase in cNKO cells compared to control cells (Figure 2.5i), as observed for BCR. These results suggest that N-WASP knockout affects the diffusivity of BCRs and CD19 in a similar way, slowing down their overall mobility and likely maintaining their interactions inside signaling clusters. We next examined the roles of different actin nucleating factors and regulatory proteins on CD19 diffusivity using inhibitors. All the actin nucleation inhibitors used caused a reduction in overall CD19 diffusivity as compared to vehicle control (Figure 2.14c – Supplementary material). For all cases, the population fraction of States 1, 3 and 6 showed a significant increase (Figure 2.14d – Supplementary material). These data suggest that BCR and CD19 in States 1 and 2 are likely to be in a signaling state.
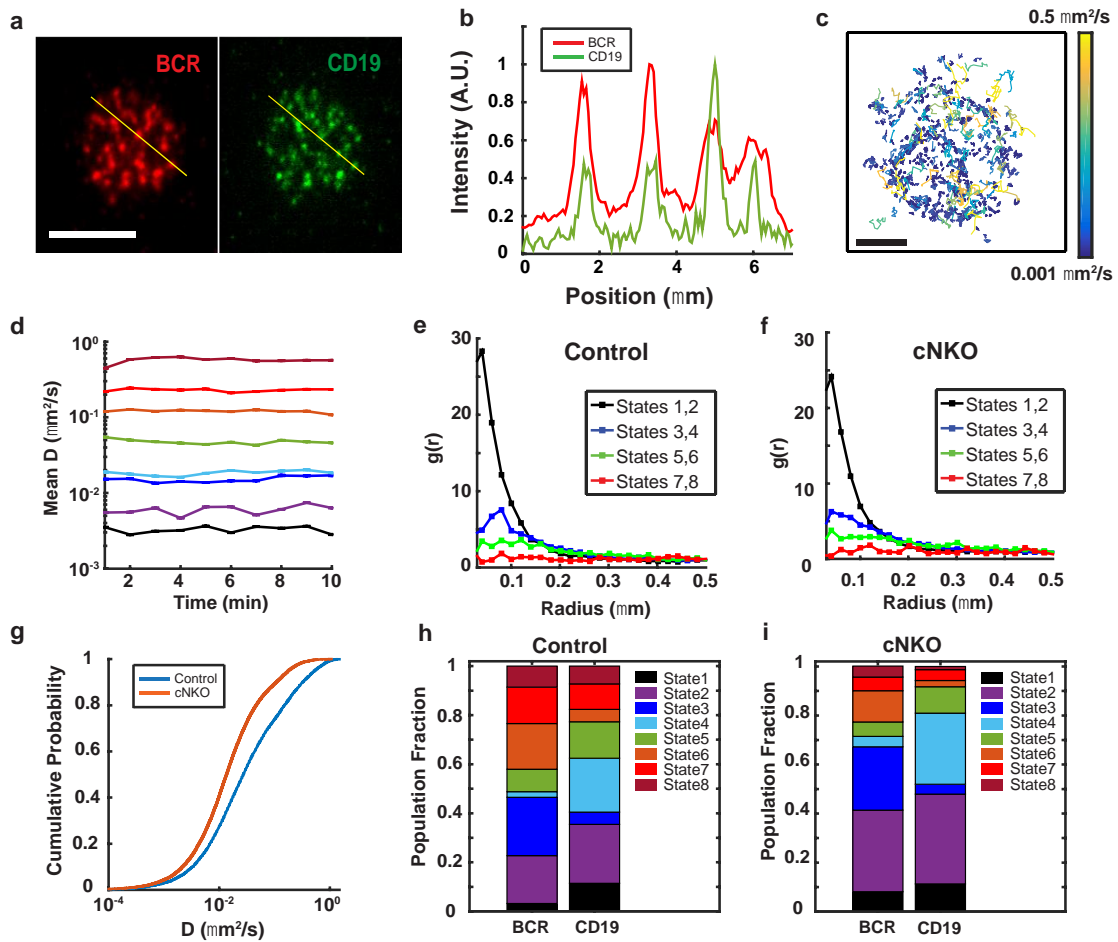
Figure 2.5. N-WASP expression modulates CD19 diffusivity. a) Instant SIM images of activated B cell, showing that AF546 labeled BCR (red) and AF488 labeled CD19 (green) reside in clusters that colocalize to within the ~150 nm resolution limit. Scale bar is 5 μm. **b)** Intensity profiles for BCR (red) and CD19 (green) fluorescence along the yellow lines as drawn in a). **c)** Compilation of CD19 tracks over a 10-minute period in an activated control B cell. Scale bar is 1 μm. **d)** Plot showing the mean diffusivity of each of the eight diffusive states obtained from pEM analysis as a function of time. The colors corresponding to the different states are as shown in Figure 2B. Error bars

represent the standard error of the mean. **e, f)** Pair correlation function plot for all states for control and N-WASP-KO cells respectively. **g)** Cumulative Probability distribution of diffusivities showing that mobility of CD19 in cNKO cells is significantly lower than in control cells (control cells N = 10, cNKO cells N = 11, P = 0.0013 Kruskal-Wallis test). **h, i)** Comparison of population fractions of BCR and CD19 in different states for control and cNKO cells respectively.

2.7 N-WASP KO has a limited effect on FcγRIIB diffusivity

To determine whether actin-mediated modulation of mobility is specific to BCRs and its stimulatory co-receptor CD19 or reflects a more general change in the diffusive properties of the membrane environment due to changes in the cortical actin network, we next tested whether the mobility of FcγRIIB, an inhibitory co-receptor of the BCR, is similarly affected by the lack of N-WASP. The FcγRIIB receptor is a transmembrane receptor that is expressed in B cells and is known to inhibit BCR signaling by the recruitment of phosphatases such as SHIP (SH2-domain containing inositol polyphosphate 5' phosphatase) [121] and BCR clustering [122], when it is colligated with the BCR by antibody-antigen immune complexes. FcγRIIB is known to exhibit relatively high diffusivity in quiescent B cells and its mobility is altered by mutations associated with autoimmune diseases [55]. In the absence of colligation, the mobility of FcγRIIB has the potential to yield important insight into the generic diffusion properties of transmembrane receptors.

We studied the diffusivity of FcγRIIB in activated B cells using the same methods used for the other receptors. Figure 2.6a shows a compilation of FcγRIIB tracks in a control cell over a 10-minute period. Our analyses showed that in contrast to the significant slowdown of BCR diffusivity in cNKO cells, FcγRIIB diffusivity is minimally affected as shown by the cumulative distribution plot of the diffusivities (Figure 2.6b). pEM analysis of the sets of all single molecule trajectories showed 7 states with stable mean diffusivities (Figure 2.6c). Pair correlation analysis of tracked FcγRIIB molecules for all states in control and cNKO cells are shown in Figure 2.6d and e respectively. As with the other receptors studied so far, States 1 and 2 display signs of clustering, States 3 and 5 also display clustering but to a lesser degree, while all other states display a more homogeneous distribution. Moreover, inhibition of actin nucleators (Arp2/3 and formins) or WASP family proteins did not result in altered FcγRIIB mobility as shown by the CDFs (Figure 2.15a-c – Supplementary material) nor change the population fraction of BCR trajectories in different diffusive states (Figure 2.15d – Supplementary material). As FcγRIIB mobility does not undergo the drastic changes observed in BCR and CD19 mobility in the absence of N-WASP or inhibitors of actin nucleation, this result suggests that N-WASP mediated regulation of receptor mobility is specific to the BCR.
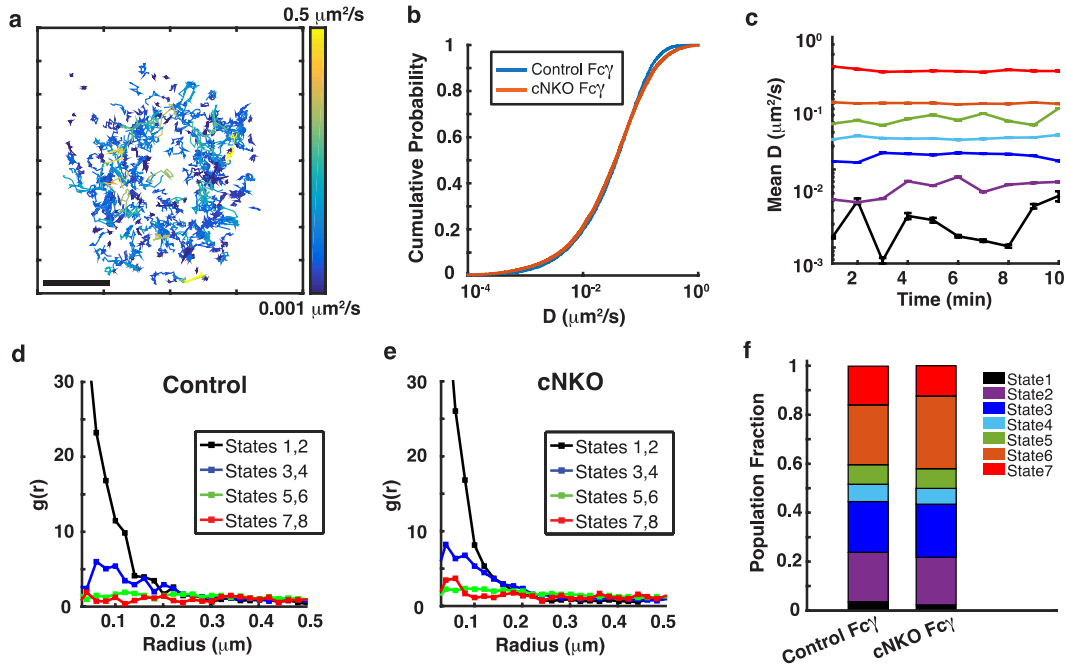
Figure 2.6. FcγRIIB mobility is mildly affected by the lack of N-WASP. a) A set of single molecule tracks of FcγRIIB from an activated B cell over a 10-minute period. Scale bar is 1 μm. **b)** Cumulative distribution plots for diffusivity of FcγRIIB molecules in control and cNKO cells (control cells N = 12, cNKO cells N = 12). **c)** pEM analysis of single FcγRIIB molecule trajectories uncovered 7 states. Plot shows the mean diffusivity of each state at every time point. Error bars represent the standard error of the mean. **d, e)** Pair correlation function plot for all states in control and cNKO states respectively. **f)** Comparison of the population fraction of different diffusive states of FcγRIIB in control and cNKO cells.

2.8 WASP-family proteins regulate actin dynamics during B cell signaling activation

58

To test whether the changes in BCR mobility and nanoscale organization induced by inhibition of actin regulators are associated with alterations in actin dynamics, we used primary B cells from Lifeact-EGFP transgenic mice activated on supported lipid bilayers. We imaged these cells using iSIM to obtain high spatial resolution images amenable to quantitative analysis for determining actin flows and compare these in the presence and absence of different inhibitors of actin nucleation and upstream regulators. In primary B cells, the actin network is organized into highly dynamic foci (indicated by blue arrows) and a thin lamellipodial region at the cell periphery (indicated by yellow arrows) in both untreated and wiskostatin treated cells (Figure 2.7a). We used Spatiotemporal Image Correlation Spectroscopy (STICS) [123] to estimate the speed and directionality of actin flows (Figure 2.7b). We extracted the information from the actin flow velocity vector maps and generated heat maps showing the magnitude of actin speeds and the direction of flow relative to the center of the cell. The magnitude of actin flow speed did not display any systematic spatial dependence in either wiskostatin treated or untreated cells (Figure 2.7c). However, wiskostatin treated cells displayed a significant reduction in actin flow speed (Figure 2.7d), suggesting that upstream regulators of Arp2/3 are required for generating a dynamic actin network.

To determine the directionality of actin flow vectors, the directional coherence was defined as the cosine of the angle relative to a vector pointing to the centroid of the cell. Thus, flows towards the cell center have value 1 and flows away from the center have

59

value -1 with all other angles spanning intermediate values within this range. The spatial maps of directional coherence values revealed that actin flows were not spatially correlated over large regions of the cell-substrate interface for cells either treated with wiskostatin or untreated (Figure 2.7e). We next determined whether the directional coherence measure evolved over time and whether this evolution differed between control and wiskostatin-treated cells. Probability distribution functions of the directional coherence values over the entire contact zone showed that during the early stage of activation (0-5 min), actin flows were predominantly directed either inwards or outwards (relative to the cell centroid) with no significant difference between control and wiskostatin-treated cells (Figure 2.7f). However, during the late stage of activation (5 -10 min), wiskostatin-treated cells displayed greater inward actin flows towards the center of the cell and less outward flows compared to control cells (Figure 2.7g).

In order to more directly examine the effect of the actin nucleation inhibitors Arp2/3 and Formin, we used iSIM imaging to visualize the actin dynamics in cells treated with CK666 and SMIFH2 (Figure 2.16a – Supplementary material). The actin organization and dynamics appear to be qualitatively different in cells treated with inhibitors with the presence of more linear bundle-like structures in CK666 treated cells and the apparent loss of these structures in SMIFH2 treated cells (Figure 2.16a – Supplementary material). Using STICS analysis to quantify actin flows in these cells, we found that actin flow speeds show a significant decrease in both CK666 and

SMIFH2 treated cells as show in the comparison of the CDF of actin speeds with respect to DMSO control (Figure 2.16b – Supplementary material).
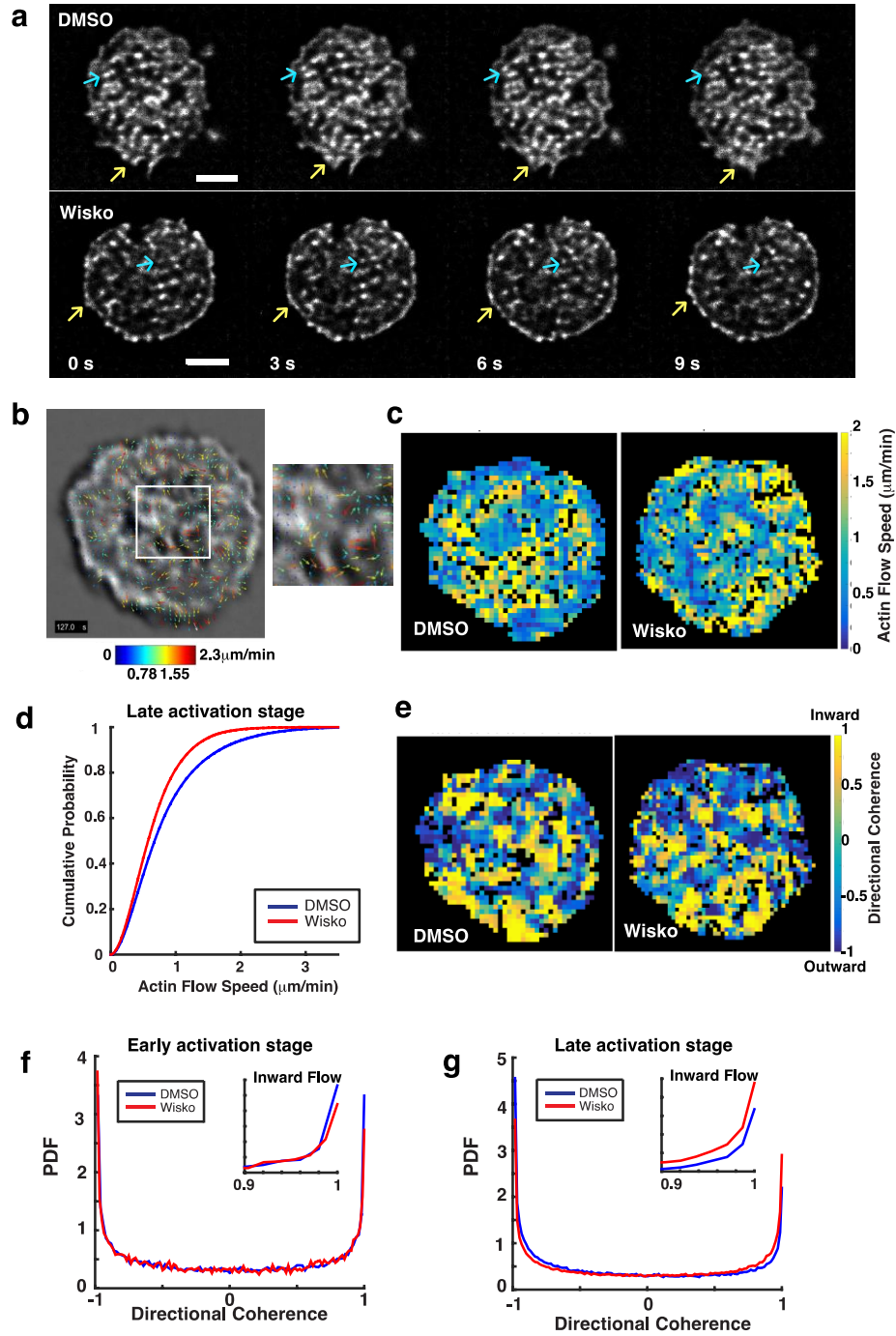
Figure 2.7. Effect of actin regulators on actin dynamics in activated B cells. a) iSIM images of activated Lifeact-EGFP B cells at consecutive time points for two conditions: DMSO carrier-control and wiskostatin (10 μM concentration). The initial time corresponds to 5 min after spreading initiation. The blue arrows in the images indicate the emergence of actin foci and the yellow arrows point to spreading and contraction of the lamellipodial region of the cells. Scale bars are 2 μm. **b)** STICS (Spatio-Temporal Image Correlation Spectroscopy) vector map showing actin flows represented by velocity vectors indicating flow direction and color coded for flow speed. In the zoomed region, the velocity vectors show the flow direction and flow speed. The vector map is overlaid on top of a grayscale image of Lifeact-EGFP. **c)** Pseudocolor map of actin flow speeds corresponding to 2 minutes after cell spreading for representative DMSO control and wiskostatin treated cells. **d)** Cumulative distribution of actin flow speeds for DMSO control cells (blue, N = 11 cells) and cells treated with wiskostatin (red, N = 12 cells). *(p = 0.00074, Kruskal-Wallis test).* **e)** Directional coherence maps indicating the flow directions, which ranged from inward (1) to outward (-1). **f, g)** Probability distribution function plots showing directional coherence values of actin flow in cells during the early stage of activation **f)** or cells in the late stage of activation **g)**, with subplots highlighting the flow fraction defined as inward flow (see methods). During early stage, fraction of inward flow is 0.143 for DMSO and 0.1425 for Wisko treated cells *(p = 0.5188 - not significant)*; during late stage the fraction of inward flow is 0.113 for DMSO and 0.1518 for Wisko treated cells *(p < 0.001).*

2.9 Discussion

Here, we used single molecule and super-resolution imaging and a novel machine learning based analysis method called perturbation Expectation Maximization (pEM) to obtain a better understanding of the diffusive properties of BCR during activation. These methods allow us to classify single molecule trajectories into states with distinct diffusivities and correlate BCR diffusivity states with its potential signaling states. We found that activation resulted in a reduction of BCR mobility with a larger fraction of BCRs in low mobility diffusive states, suggesting that signaling BCRs have low diffusivity. Using pair correlation analysis to quantify the degree of clustering exhibited by BCRs and relate them to their local mobility, we found that BCRs in states with low diffusivities display a greater degree of clustering. Inhibition of actin nucleating proteins using small molecules reduced both BCR diffusivity and actin flows, suggesting that the reduced BCR mobility is actin mediated. Consistently, using B cells from conditional N-WASP knockout mice (cNKO) and from WASP knockout mice (WKO), we found that loss of WASP and N-WASP, upstream activators of actin dynamics, also resulted in overall lower BCR diffusivity compared to control cells. In order to further relate BCR signaling and diffusivity, we took advantage of the fact that B cells from cNKO mice [50] have been shown to display enhanced signaling. We found an increase in the fraction of low mobility states in cNKO B cells. We further found that the stimulatory co-receptor, CD19, also showed similar reduction of mobility and enhancement of low mobility states in cNKO B cells, suggesting that the low diffusivity states correspond to signaling states. In contrast, the inhibitory co-

receptor, FcγRIIB [112, 113], did not show a difference in diffusivity or distribution across mobility states between control and cNKO B cells, suggesting that the effect of N-WASP on BCR and CD19 mobility is not global for all membrane proteins during B cell activation. Our studies further showed that both N-WASP knockout and inhibition of the Arp2/3 complex, which nucleates branched actin networks, resulted in an overall reduction of BCR diffusivity, suggesting that the effect of N-WASP on nanoscale BCR mobility is likely mediated through activation of Arp2/3-mediated actin nucleation. Overall, our study reveals the link between BCR diffusion and signaling and suggests that actin dynamics, mediated by WASP family proteins, regulate BCR signaling by modulating the diffusivity of BCR and its co-receptors and their nanoscale organization during activation.

We also found that inhibition of formin resulted in reduced BCR mobility, but with somewhat different effects on the diffusive states as compared to the effects of Arp2/3 inhibition. The effect of SMIFH2 could arise due to direct reductions of linear actin structures produced by formin or by alterations of the branched actin networks produced by the cooperation of Arp2/3 and Diaphanous formins. Studies have shown that formation of branched filaments by Arp2/3 requires an existing actin filament and a nucleation-promoting factor to start polymerizing actin [7]. The formin, mDia1, can generate mother filaments that set the basis for the formation of the actin meshwork that underlies the formation of different types of cell protrusions. Such cooperative interactions have been observed between the formin mDia1 and Arp2/3 for the

64

generation of lamellipodia and ruffles on HeLa cells [124] and the formation of proper actin architecture at the fusion site during invasive podosome formation in fruit flies [125]. Furthermore, T cells from mDia1-knockout mice cannot form lamellipodia or ruffles, and exhibit defective cell motility [126]. In summary, our studies suggest that optimal BCR signaling requires homeostatic balance between actin networks generated by multiple nucleating proteins.

Extending previous studies showing that N-WASP knockout is associated with enhanced signaling [50], our observations suggest that low mobility BCR trajectories are associated with signaling states. Using both pair correlation and pEM analysis, we showed that the low diffusivity of BCRs on the surface of cNKO B cells is accompanied by a lower diffusivity of its stimulatory co-receptor CD19, again strengthening our hypothesis that signaling states of BCRs correlate with those that display decreased mobility. Stone et al. showed that the spatial positions of the BCR and Lyn, a signaling kinase, become correlated after antigen stimulation, and this correlation is accompanied by a reduction in diffusivity of both molecules [53]. Using a photoactivatable antigen, Wang et al. [52] measured the diffusivity of BCR on the same set of cells before and after activation and found a decrease in BCR diffusivity following antigenic stimulation. During activation, conformational changes of ITAM-containing receptors, changes in local lipid environment and interactions with other proteins may alter the mobility of membrane receptors [127]. For instance, stimulation of mast cells through FcεRI receptor crosslinking, induces the clustering of FcεRI and a concomitant

reduction of its diffusivity that depends on the average number of receptors in the cluster [128]. The clustering of FcεRI receptor is accompanied by the redistribution of the signaling proteins Lyn kinase and Syk kinase into clusters [129]. Thus, our findings are broadly consistent with prior studies that link receptor diffusivity and clustering with their signaling state.

A well-accepted model of the regulation of BCR diffusion by the actin cytoskeleton in resting B cells posits that the actin network imposes diffusional barriers on BCR and other receptors and signaling proteins [35, 108]. Activation leads to the dissolution of these barriers either by severing of actin filaments [46] or removal of cytoskeletal/membrane anchors [108], thereby enhancing BCR diffusion, leading to further activation. However, previous models have not considered an active role for actin dynamics in signal regulation. Based on our observations, we suggest that in contrast to prior models, the role of the actin cytoskeleton in BCR signaling goes beyond providing a mechanical barrier for receptor diffusion. Specifically, we propose that non-equilibrium, rapidly changing actin flows may serve to 'stir' the cytoplasm adjacent to the membrane, thus changing the reaction environment of receptors and signaling molecules, and modulating the reaction rates in the juxta-membrane regions of the cytoplasm [130]. Actin regulatory proteins modulate the level of non-equilibrium actin dynamics and thereby alter receptor mobility and their signaling states.

According to our new model, we propose the following dynamics of early BCR signaling. At rest, BCRs are confined within membrane compartments defined by the actin cytoskeleton (Figure 2.8a). Early BCR signaling leads to the loss of these barriers, as well as increased actin dynamics (Figure 2.8b). Our imaging studies have revealed that B cell actin dynamics is not characterized by spatially coherent directional flows. Rather, actin dynamics are highly complex, with sharp changes in speed and directionality, both spatially and temporally. This dynamics may also be associated with the formation of non-equilibrium actin structures such as asters and foci [84, 131]. This active stirring, combined with the release of BCRs from diffusion traps, may drive receptors into clusters and facilitate receptor interactions with activating kinases [31]. At later stages, further increases in actin dynamics and increased outward actin flows could decrease reaction rates between BCRs and activating kinases or increase reaction rates between BCRs and inhibitory co-receptors, making signaling states more unstable, facilitating down-regulation of signaling (Figure 2.8c top). Inhibition or loss of upstream regulators of actin nucleation results in a reduction of actin dynamics (Figure 2.8c bottom). This may decrease actin-mediated mixing of BCRs in the membrane, likely enabling BCR to enter and remain in signaling states (clusters) leading to enhanced signaling and preponderance of low mobility states (or conversely increased interactions with phosphatases leading to signaling inhibition).

Based on our observations, we suggest that actin dynamics in the cell may be used to fine-tune the levels of signaling activation. Modulation of the structure and dynamics

67

of actin networks, by changing the expression levels or spatial distribution of actin regulatory proteins, may provide the cell with a powerful way to regulate signaling over rapid timescales. These properties are likely to be a general feature of cells in the immune system whose function depends on rapid response to external stimuli, and illustrate general principles of immune receptor signaling.
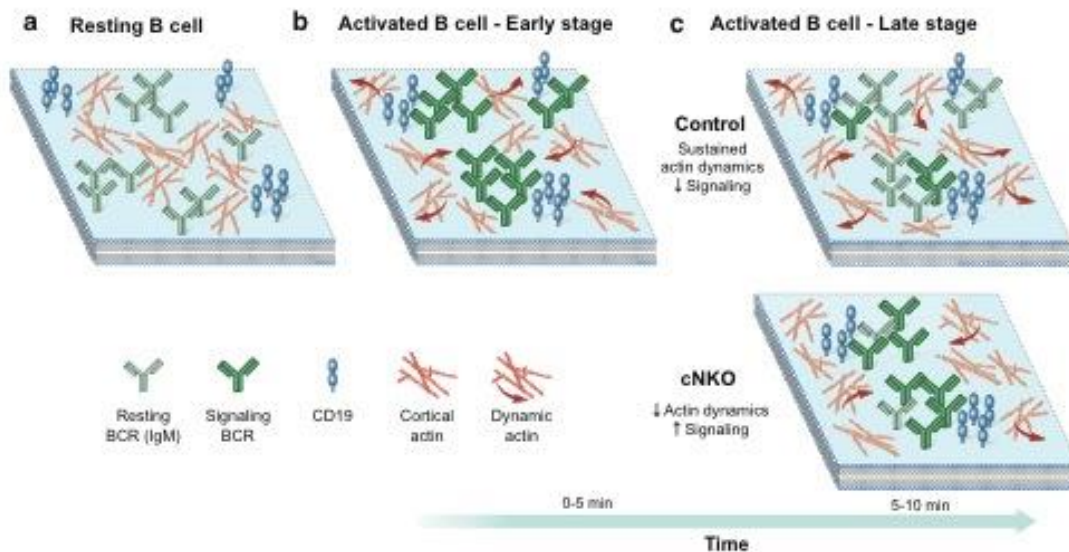
Figure 2.8. The actin cytoskeleton regulates B cell receptor mobility and signaling in different stages. Representative cartoon showing receptor distributions on a section of the B cell membrane: **a)** Resting B cell membrane: Actin networks restrict receptor lateral movement and interactions. **b)** B cell membrane at the early signaling activation stage. Actin remodeling enhances receptor mobility allowing for interactions between receptors, specifically BCR and CD19, enhancing signaling. Actin flows towards the center and edge of the immune synapse in similar proportions. **c)** B cell membrane at later activation stages. Top: Actin flows stir the cytoplasm at the membrane vicinity,

68

increasing the mixing of receptors in the membrane and thereby allowing signal inhibitory molecules to down-regulate BCR signaling. Bottom: N-WASP knockout reduces actin dynamics and changes the balance of actin flow directionality at later stages (5-10 min) of activation, leading to enhanced signaling. The arrows accompanying the dynamic actin are used to indicate the balance between inward and outward actin flows at each activation stage and under each condition.

2.10 Methods

2.10.1 Mice and cell preparation

B-cell– specific N-WASP knockout (CD19$^{Cre/+}$ N-WASP$^{Flox/Flox}$, cNKO) mice and control mice (CD19$^{+/+}$ N-WASP$^{Flox/Flox}$) were bred as previously described [32]. Transgenic Lifeact-EGFP mice are as described before [132]. Mice selected for experiments were between 2 to 4 months old with no gender preference. Naïve primary B cells were isolated from mouse spleens using a negative selection procedure as described before [114]. After extraction, cells were kept at 4 ˚C and cell aliquots were pre-warmed at 37 ˚C for 5 minutes before being added to the bilayer. All experiments involving animals have been approved by the University of Maryland Institution Animal Care and Usage Committee.

2.10.2 Fluorescent antibodies and inhibitors

For inhibition of formin and Arp2/3, cells were incubated with inhibitors for 5 minutes at 37 ˚C before being added to the imaging chamber, which had the inhibitor at the same concentration used for incubation. SMIFH2 (Sigma-Aldrich) was used at a 25 μM concentration. Arp2/3 complex inhibitor I, CK-666 (Calbiochem) was used at 50 μM. For N-WASP inhibition, wiskostatin B (EMD Bioscience) was used at 10 μM to incubate the cells for 1 hour at 37 ˚C. Mono-biotinylated fragment of antibody (mbFab'-anti-Ig) was generated from the $F(ab')_2$ fragment (Jackson Immuno Research, West Grove PA) using a published protocol [133]. FcγRIIB (CD32) antibody (BD Biosciences) was conjugated with Alexa Fluor 546 using Molecular Probes Protein labeling kits (Invitrogen) following manufacturer protocols. For labeling of CD19 we used the Alexa Fluor 594 anti mouse CD19 antibody (BioLegend).

2.10.3 Sample preparation for single particle tracking

Glass slides were kept in Nanostrip (Cyantek) overnight and then rinsed with dd-H_2O and dried with filtered air. Supported lipid bilayers were prepared by incubating slides with 10 μM DOPC/DOPE-cap-biotin liposome solution for 10 minutes at room temperature. The slides were rinsed with filtered PBS (1X) and then incubated for 10 minutes with 1 μg/ml solution of streptavidin. Slides were rinsed again with PBS and then incubated with unlabeled mono-biotinylated fragment of antibody (mbFab) solution at 18 μg/ml. PBS was replaced with L-15 (CO_2 independent media with 2% FBS) before imaging. 0.75 μl of 0.05 mg/ml AF546 labeled mbFab was added to a 250 μl volume of media in the imaging chamber.

As non-activating controls, streptavidin coated lipid bilayers on coverslips were incubated with biotinylated transferrin (Jackson) (16 μg/ml) for 10 minutes at room temperature. Slides were rinsed with PBS and then the PBS was replaced with L-15 (CO_2 independent media with 2% FBS) before imaging. Cells were added to transferrin-coated lipid bilayers and incubated for 5 minutes. For single particle imaging, 0.75 μl of 0.05 mg/ml AF546 labeled mbFab is added to a 250 μl volume of media in the imaging chamber.

2.10.4 Microscopy

For single molecule imaging of BCR we used an inverted microscope (Nikon TE2000 PFS) equipped with a 1.49× NA 100 lens for TIRF imaging and an electron multiplying charge coupled device (EMCCD) camera (iXon 897, Andor). In order to image single molecules on the cell membrane for extended periods of time we add a low concentration of the fluorescent antibody in solution as shown in Figure 1. Cells are imaged from the moment they reach the bilayer and time-lapse movies (1000 frames acquired at 33 Hz) representative of each minute are taken. Figure 1B shows a representative frame where the cell outline is obtained from an IRM image taken after the single molecule movie. The molecules detected at each frame are localized with high precision (~20 nm) and linked frame by frame to create tracks [118] using a MATLAB routine. Taking into account motion blur, pEM estimates localization precision to range between 20 nm (slowest states) to 80 nm (fastest state). Imaging of

71

Lifeact-EGFP expressing murine primary cells spreading on supported lipid bilayers was performed using instant Structured Illumination Microscopy (iSIM) [44], with a 60X 1.42 N.A. lens (Olympus), a 488 nm laser for excitation with 200 ms exposure times and a PCO Edge camera. Images obtained are post-processed with background subtraction and deconvolution. The final lateral resolution for deconvolved images is between 140-150 nm. Spreading cells were imaged at 2 second intervals and spread cells were imaged at 5 frames per second. The Richardson-Lucy algorithm is used for deconvolution, and run for 10 iterations. The PSF used was simulated by a Gaussian function but based on parameters obtained from measurement, i.e. the FWHM of the PSF used is the same as the FWHM measured.

2.10.5 Data analysis

The traditional approach for determining diffusion coefficients is to fit the experimental mean-square displacement (MSD) versus delay time to a linear function, yielding the diffusion coefficient as the slope. However, Flyvbjerg et al. [116] showed that this method is inferior to approaches based on the covariance of particle displacements. We find that on an ensemble level, this method yields diffusion coefficients that differ by at most a factor of two from published studies [51] (Figure 2.17 – Supplementary material). For individual tracks, even covariance-based methods lead to diffusivities that suffer from significant errors, because of the limited duration of tracks (due to photobleaching), and because measured particle positions are themselves subject to significant errors, both as a result of the limited number of photons from each

fluorescent particle and because of the motion blur that inevitably occurs for a non-zero exposure time. In principle, it is possible to mitigate the noise inherent to individual trajectories by averaging over multiple tracks. However, in the heterogeneous cellular environment, the diffusive properties of different trajectories are likely to vary and are unknown a priori. Thus, to employ ensemble averaging, it is necessary to sort trajectories into sub-populations that share diffusive properties. Freeman et al. [46] sought to account for heterogeneity by employing a two-state Hidden Markov model to separate trajectories into high diffusivity segments and low diffusivity segments. However, the choice of two diffusive states was imposed by fiat, rather than emerging from the data.

Therefore, in order to obtain a better understanding of the diffusive properties of the BCR, we have employed a newly-introduced methodology, Perturbation-Expectation Maximization (pEM), which sorts a population of trajectories into discrete diffusive states, simultaneously determining the optimal covariance values for each state. Perturbation-Expectation maximization version 2 (pEM v2) was used to classify single molecule tracks derived from different receptors [117]. To perform pEM analysis all tracks must have the same length. Given the 33 Hz imaging rate, the optimal track length was found to be 15 frames long due to the tradeoff between accurately identifying diffusivities and minimizing the number of state transitions that the particle may undergo over a single trajectory [118]. All single molecule trajectories obtained were split into 15 frame segments and the classification analysis was performed on the

73

set of all these track segments. Trajectories larger than 105 frames or shorter than 15 frames were discarded. The tracking routine interrupts the creation of a trajectory whenever two particles cross paths. To avoid an over counting of slow-moving molecules (which have lower probability of crossing paths with other molecules) we discarded trajectories longer than 105 frames. The data was then separated according to the receptor type and PEM v2 was run for all data sets using 20 re-initializations, 150 perturbations, 14 covariance parameters and allowing the system to explore up to 15 states. This set of parameter values was chosen to ensure convergence to the global maximum. For all conditions, the average track length was 40 frames and typically 100 tracks were obtained per cell per time point. The maximum posterior probability value was used to assign a track uniquely to a particular state as shown in Supplementary Figure 2.18a for BCR in control cells. For BCR, 186959 tracks corresponding to all inhibitor treatments, DMSO control and cNKO cells were analyzed together. For CD19, 35062 tracks corresponding to control and cNKO were pooled together and analyzed, and for FcγRIIB receptor, 24969 tracks were analyzed. For all the receptors and conditions 8 diffusive states were identified. The states were compared across different receptors based on a comparison of their diffusivity distributions (Figure 2.18b – Supplementary material).

STICS analysis of actin flows was implemented on iSIM images taken at 2-second intervals. Sub-regions of 8×8 pixels were selected with a shift of 2 pixels between sub-regions. Immobile filtering was set to 20 frames and the time of interest (TOI) was

chosen as 5 frames with a shift of 3 frames between TOIs. Velocity flow vectors that exceeded the sub-region threshold were discarded, giving place to the 'black pixels' observed in the decomposed maps of speeds and directions. To determine the directionality of the flow, the centroid of the cell was calculated and a vector from each of the sub-regions pointing towards the centroid was obtained. The directional coherence was then determined as the cosine of the angle between velocity vector and the vector pointing to the centroid. Directionality plots were generated using the MATLAB function histcounts and using probability density function (PDF) as normalization type. In order to compare directionality between DMSO and wiskostatin treated cells the fraction of inward flow (values larger than 0.9) and the fraction of outward flow (values less than -0.9) was determined. The comparison of fraction of flow in either direction between the two conditions was tested using the z-test where the null hypothesis is that both fractions are equal.

For receptor diffusivity studies 12 control and 9 cNKO mice were used. For actin dynamics studies, 3 Lifeact-EGFP mice were used.

2.10.6 Statistical analysis

The Kruskal-Wallis test was used to assess the difference between the diffusivity distributions corresponding to different conditions. We used this test for most comparisons because is a non-parametric method for testing whether two data samples originate from the same distribution. The test was performed over smaller data subsets

selected randomly and implemented using the kruskalwallis function in MATLAB. The

pair wise *z*-test was used to determine the difference in proportions of diffusive states

across different conditions.

2.11 Supplementary Materials
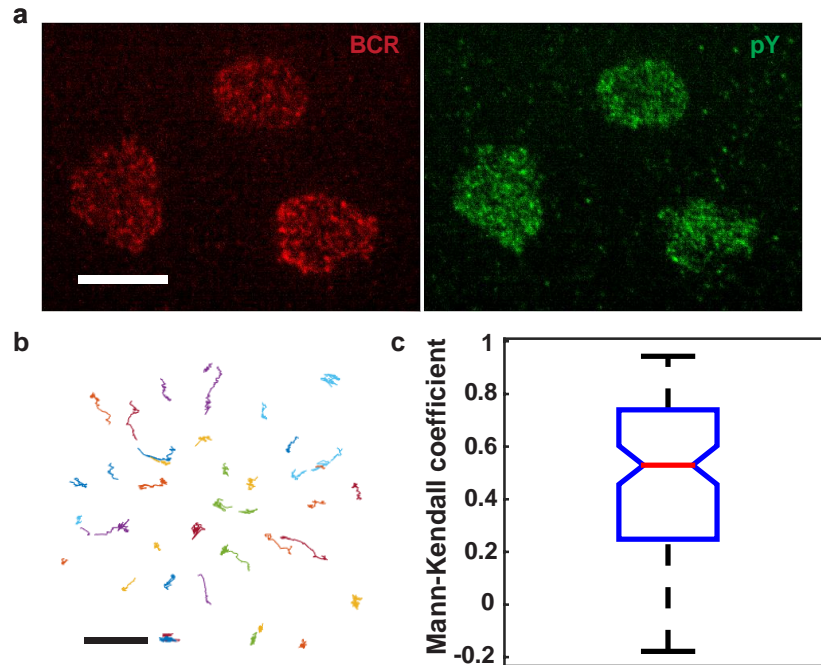
Figure 2.9. B cells become activated in the single molecule imaging experiments.

a) iSIM images of fixed cells (fixed after 3 min of spreading initiation) activated under

the same conditions as the single molecule experiments. The red color corresponds to

AF546 BCR labeled microclusters while the green is AF488 labeled phosphorylated

tyrosine, which also accumulated in clusters. Scale bar is 5 μm. b) BCR microlusters

were tracked as they moved towards the center of the cell during the first 200 seconds

after the cell contacted the bilayer. Scale bar is 1 μm. c) The intensity within clusters

over time was quantified (N = 10 cells) and the Mann-Kendall coefficient was calculated to show the overall increase in intensity over time (MK > 0).
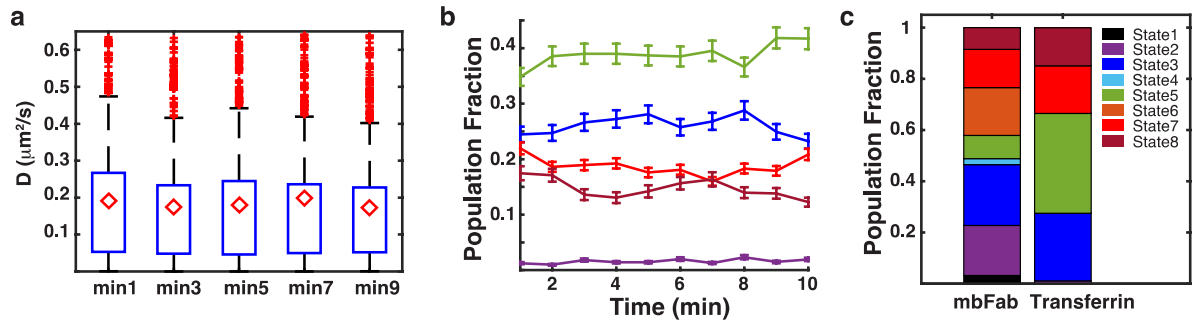
Figure 2.10. Progressive reduction in BCR mobility is specific to BCR activation.
a) Boxplot showing BCR diffusivity for cells on a non-activating transferrin coated bilayer measured at 1, 3, 5, 7 and 9 minutes after adding cells. Red diamonds represent the mean (data obtained from 16 cells). b) Population fractions over time for BCR in cells on non-activating substrate. c) Comparative population fractions for BCR in distinct states over the entire time period that cells were imaged for cells on activating (mbFab) and non-activating (transferrin) conditions.
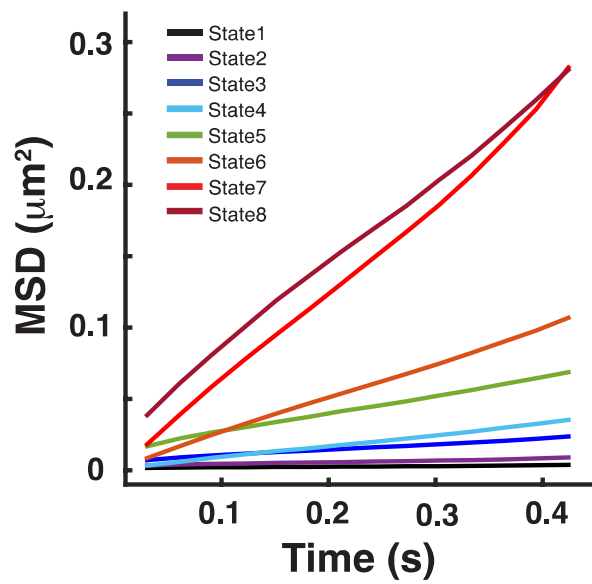
Figure 2.11. eMSD for cNKO cells. Ensemble mean square displacement (eMSD) plots for the 8 states identified for BCR in cNKO cells.
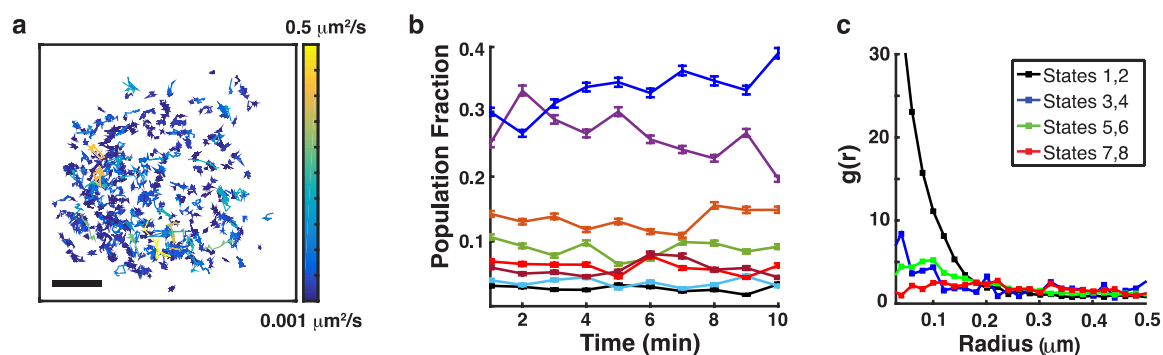
Figure 2.12. Single molecule tracking and pEM analysis of BCR in WASP knockout B cells. a) Tracks of BCR molecules in a WKO cell during a 10 minute period. The tracks are color-coded for diffusivity. b) Plots of population fractions over time for the diffusive states identified in WKO cells. Error bars represent a confidence interval of 95% on the population fraction calculation. c) Plot of pair correlation as a function of distance for all states.
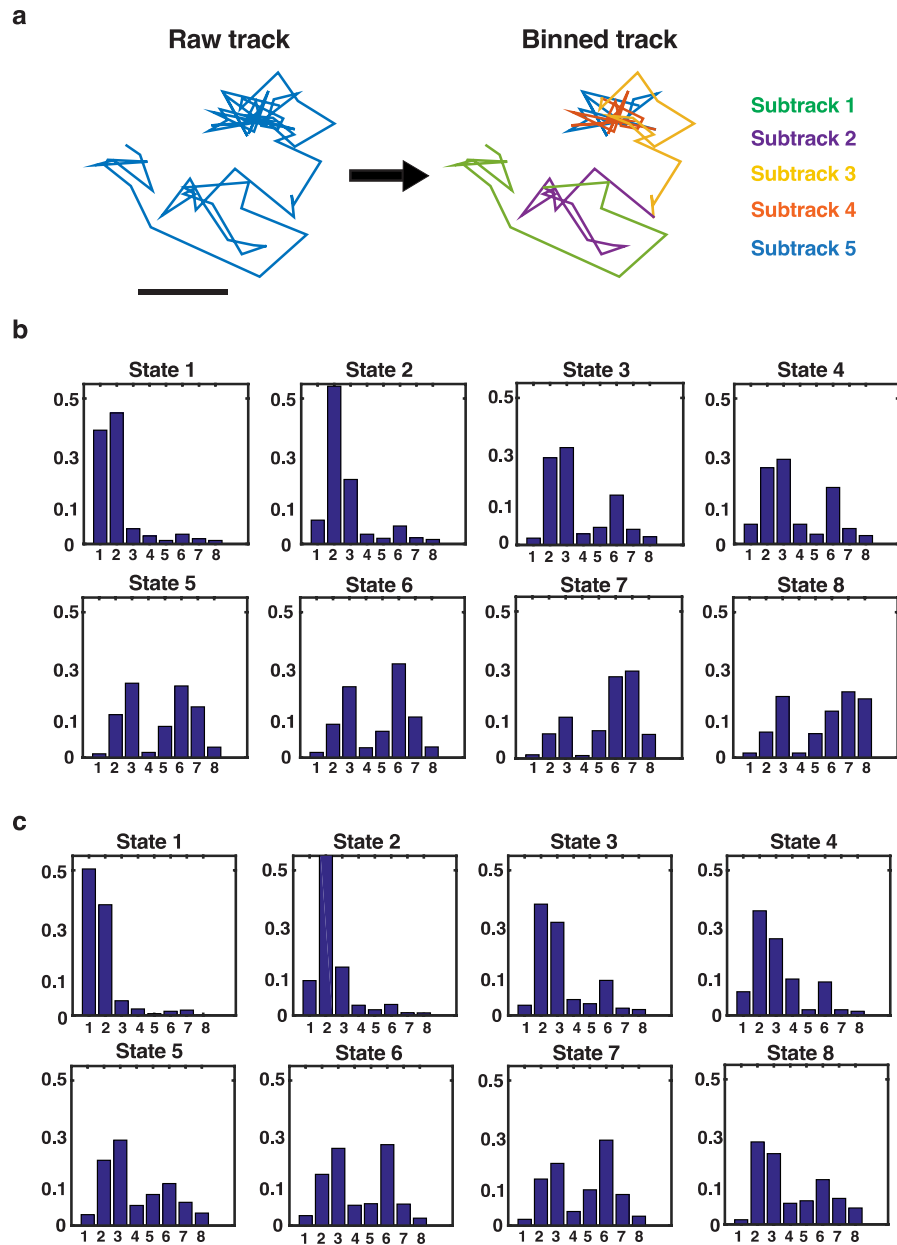
Figure 2.13. Transitions between diffusive states within single particle trajectories. a) All single BCR molecule trajectories are split into 15 frame long sub-tracks. pEM analysis is performed over the set of 15 frame long binned tracks and then the original trajectories are reconstructed to obtain information about the transitions of

molecules across different states. Scale bar is 1 µm. b) Plots showing the fraction of transitions made from each state to itself and to all others in control cells. Numbers on the x-axis indicate the state to which the transitions are being made. c) Plots showing the fraction of transitions made from each state to itself and to all others in cNKO cells.
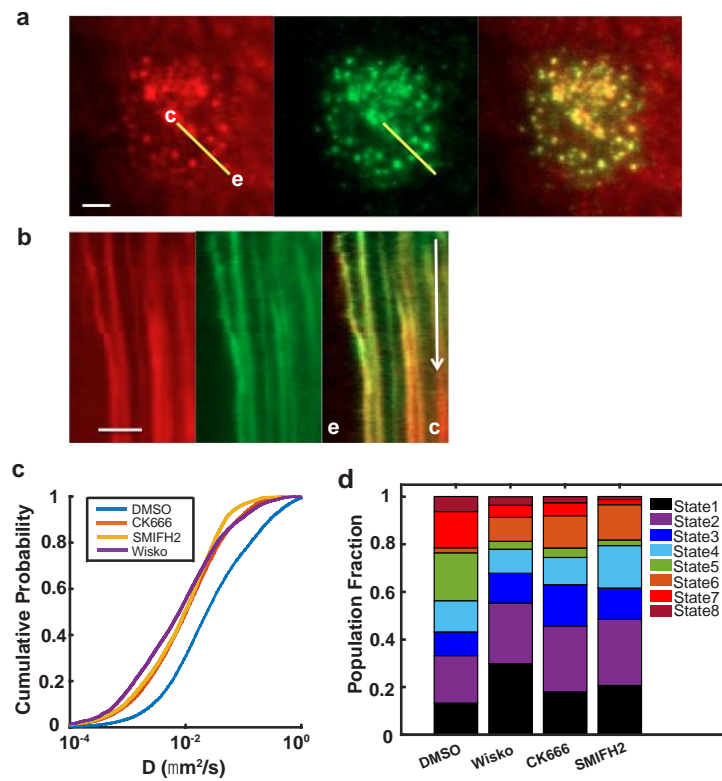
Figure 2.14. CD19 co-localize with BCR during signaling activation and its mobility is modulated by actin regulators. a) TIRF images of BCR (red) and CD19 (green) microclusters and the overlay of both channels. b) Kymograph generated along the line indicated in a) showing the inward movement of the microclusters and their

superposition as they move. **c** marks the center of the cell and **e** the cell edge. c) Comparison of the cumulative distribution function of CD19 diffusivity in control cells and cells treated with inhibitors of actin regulatory proteins (CK666, SMIFH2, wiskostatin). d) Comparison of population fractions of CD19 diffusivity in control and inhibitor treated cells.
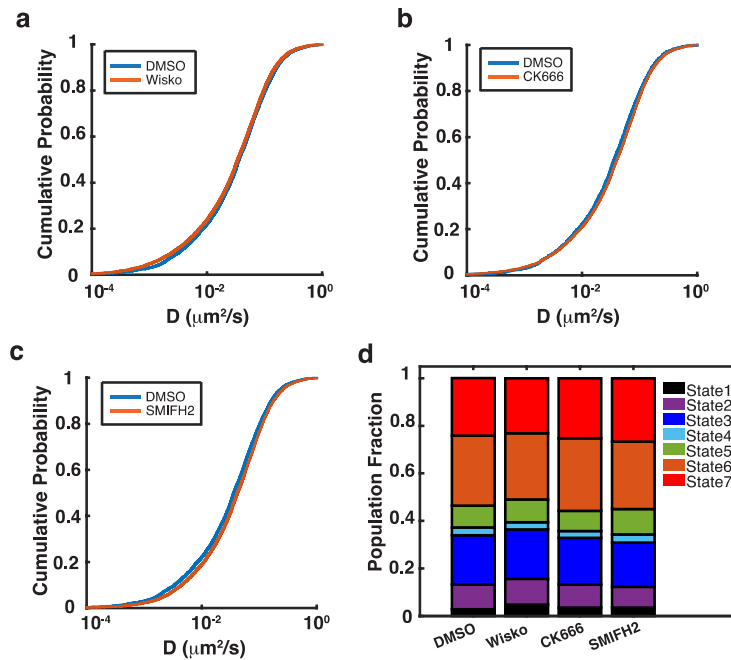
Figure 2.15. Inhibition of actin nucleators does not affect FcγRIIB diffusivity. Cumulative probability plots comparing FcγRIIB diffusivity for control cells with vehicle control DMSO with cells treated with a) Wiskostatin (10 μM), b) CK666 (50 μM) and c) SMIFH2 (25 μM). (Differences were not significant). d) Population fraction comparison of FcγRIIB diffusivity in control and inhibitor treated cells (DMSO N=9, CK666 N=10, Wisko N=8, SMIFH2 N=11).
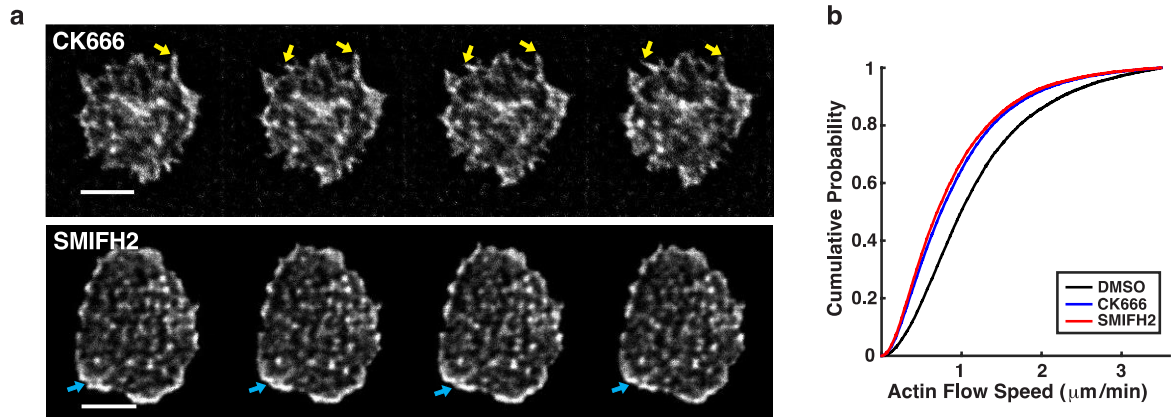
Figure 2.16. Inhibition of actin nucleators reduces actin dynamics. a) iSIM images of activated Lifeact-EGFP B cells at consecutive time points for two conditions: Top: Arp2/3 inhibitor CK666 (50 μM concentration), showing linear actin structures (yellow arrows); Bottom: formin inhibitor SMIFH2 (25 μM concentration), showing loss of actin bundles (blue arrows). The initial time corresponds to 5 min after spreading initiation. Scale bar is 3 μm. b) Cumulative distribution function of actin flow speeds obtained from STICS analysis of 1 minute long movies (at 2 second intervals) for cells treated with DMSO, CK666 and SMIFH2 (N=7 for each case). Actin flow speed is significantly different for cells treated with DMSO compared with CK666 and SMIFH2 ($P < 0.0001$ KS test).
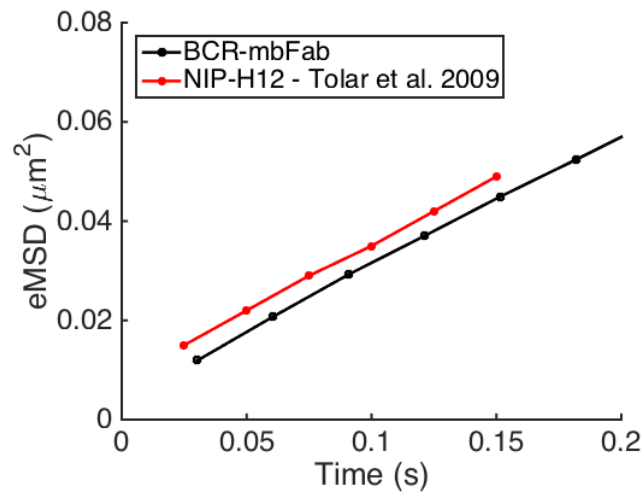
Figure 2.17. Ensemble MSD comparison with published data. Plot showing an overlay of the data points from the ensemble Mean Square Displacement (eMSD) for BCR of B cells activated with monovalent antigen (NIP-H12) from Tolar et al.[51] (black) with our data (red). The overlaid plot shows that both curves have the same slope (with different Y-intercepts possibly due to a difference in acquisition equipment).
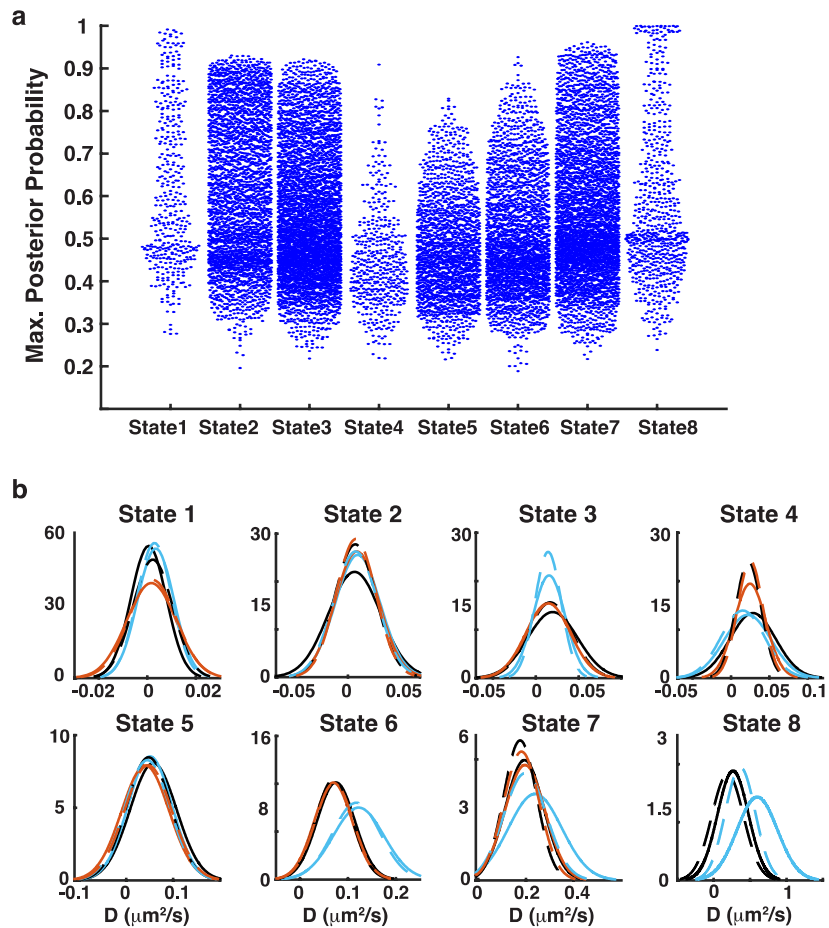
Figure 2.18. Comparison of diffusive states across receptors and conditions. a) Beeswarm plots showing the maximum posterior probability used to assign a track to a particular state for BCR in control cells. Each point represents a 15 frame long track. b) Plots of diffusivity distributions for each state used to compare across conditions. Black curves correspond to BCR, blue to CD19 and orange to FcγRIIB. The solid lines correspond to control cells and the dashed lines to cNKO cells.

Table 2.1. Statistical test for the comparison of population fractions using the Z test between control, cNKO and WKO. The percent change is obtained by comparing the different conditions against control.

WT v/s cNKO	State 1	State 2	State 3	State 4	State 5	State 6	State 7	State 8
Percent change	153.14	70.61	8.46	75.61	-35.72	-31.60	-62.69	-46.99
p	< 0.001	< 0.001	0.01500	0.0324	< 0.001	< 0.001	< 0.001	< 0.001

WT vs WKO	State 1	State 2	State 3	State 4	State 5	State 6	State 7	State 8
Percent change	-10.39	35.13	38.28	49.53	-5.23	-27.48	-57.14	-31.27
p	0.02	< 0.001	<0.001	<0.001	0.96	< 0.001	< 0.001	< 0.001

WKO v/s cNKO	State 1	State 2	State 3	State 4	State 5	State 6	State 7	State 8
Percent change	182.52	26.25	21.56	17.44	32.16	-5.68	-12.93	-22.87
p	< 0.001	< 0.001	<0.001	<0.001	< 0.001	0.003	< 0.001	< 0.001

Chapter 3: Actomyosin dynamics modulate microtubule deformation and growth during T cell activation

I was the main person involved in experimental design, sample preparation, data collection, image processing and data analysis, and writing of the manuscript.

3.1 Introduction

T cells play a major role in the adaptive immune system. Upon stimulation of the T cell receptors (TCR) by engagement of antigens presented by antigen-presenting cells (APC), T cells spread over the APC. The junction formed between the two cells is known as the immunological synapse (IS). This process is characterized by polarization of the T cell and dramatic remodeling of the actin cytoskeleton with accumulation of filamentous actin at the periphery of the cell-cell contact [74, 76, 86]. T cell polarization is also accompanied by reorganization of the microtubule cytoskeleton and reorientation of the centrosome towards the contact zone, a process that occurs within minutes of TCR stimulation. Centrosome reorientation requires the coordination of the actin and microtubule cytoskeletons, and is important both for the release of cytolytic granules in cytotoxic T cells and for the secretion of cytokines in T-helper cells [67, 74, 81].

The formation of the T cell IS has been extensively studied using antigen coated flat substrates to mimic the APC, facilitating the use of fluorescence microscopy. A remarkable feature of the immunological synapse is the bull's eye pattern produced by

the spatial reorganization of several signaling and associated proteins. This pattern manifests as three concentric rings of membrane receptors with their underlying cytoskeletal and signaling proteins [134]. At the center lies the central supramolecular activation cluster (cSMAC), which is depleted in actin and concentrates the TCR and signaling co-receptors such as CD28. The next region is the peripheral SMAC (pSMAC) with integrins and sarcomeric-like acto-myosin structures. Lastly the distal SMAC (dSMAC), which contains large ectodomain proteins, like CD45 and is characterized by a lamellipodial actin meshwork. These different regions appear to be differentially regulated by actin regulatory proteins. The Arp2/3 complex, which nucleates branched actin networks, is largely localized in the dSMAC, while the pSMAC is rich in formin-mediated actin linear structures that associate with myosin bipolar filaments to generate a contractile ring [71, 131, 135]. Arp2/3 and formin have been found to compete for the available pool of actin monomers in several cell types [136, 137]. In Jurkat T cells, inhibition of Arp2/3 leads to an increase of formin-mediated actin arcs or cables, while inhibition of formins abolishes actin arcs and enhances the Arp2/3-generated lamellipodial actin meshwork [70]. Thus, these actin-nucleating proteins mutually regulate each other.

While the role of actin at the IS has been studied extensively, the role of microtubule dynamics during IS formation has been less well examined. The microtubule end binding protein 1 (EB1) has been shown to interact directly with the CD3 ITAM. EB1 knockdown alters TCR dynamics and prevents propagation of TCR activation signal to

LAT [138]. Dynein motors co-localize with TCRs and TCR microclusters move along MTs towards the center of the immune synapse in a dynein dependent manner [99]. Hui et al. found that the traction force generated by T cells is regulated by dynamic MTs through suppression of RhoA activation, myosin bipolar filament assembly and actin retrograde flow [98]. MTs are also involved in centrosome reorientation towards the activation surface which occurs within the first 5 minutes of cell activation and is known to require the coordination of myosin and dynein motors [75, 86, 91]. Interestingly, formin is also required for centrosome polarization in T cells [92, 93] and IQGAP1 (a protein with binding domains for actin and MTs) plays a major role in centrosome repositioning in B cells after signaling activation [139]. Both findings point to an interesting connection between actin and microtubules and highlight the importance of crosstalk between these two cytoskeletal systems.

Despite extensive research on signaling events at the immune synapse, how different cytoskeletal components coordinate to establish the immune synapse upon T cell activation is not well understood. In this work we aim to elucidate the interactions between microtubules and actin at the IS with high-resolution fluorescence microscopy of Jurkat T cells. In particular, we investigate the role of Arp2/3 and formin generated actin structures on MT growth and dynamics using chemical perturbations. We characterized MT dynamics (growth rates and filament shapes) in the different regions of the immune synapse. We find that MT growth is slower in the distal actin-rich region and MT tip trajectories were less radial and more likely to change direction. Formin

inhibition lead to a moderate decrease in MT growth rates. Integrin engagement did not have any visible effects on MT growth dynamics. However, formin inhibition in cells activated on VCAM-1 coated wells caused a strong reduction in MT growth rates while Arp2/3 inhibition lead to an increase in MT tip speeds. We also found that microtubules filaments are more highly deformed and more dynamic in the peripheral actomyosin rich region of the cell-substrate contact compared to the central actin-depleted zone. Inhibition of formin and Arp2/3 as well as ROCK kinase resulted in decreased deformations and shape fluctuations of MT filaments suggesting that actin dynamics and actomyosin contractility play an important role in defining MT shapes. Our results indicate an important mechanical coupling between the actomyosin and microtubule systems where different actin structures influence microtubule dynamics in distinct ways.

3.2 Spatial distribution of cytoskeletal components in the immune synapse

The T cell immune synapse characteristically forms three concentric regions (cSMAC, pSMAC and dSMAC) which are distinguished by the accumulation of distinct sets of membrane proteins (TCR, coreceptors, integrins and phosphatases) [77, 78]. Actin dynamics and architecture has also been shown to have spatial variations across these different regions of the IS. Actin retrograde flow decreases as it goes from the periphery towards the center of the cell -- fastest at the lamellipodium (distal region, normalized radius >= 0.8), its speed decreases across the lamella (peripheral region 0.3 < radius <

0.8) and the actin structures at central region (radius<0.3) do not display directed motion [85].

In order to characterize the distribution of cytoskeletal components at the contact zone, we allowed Jurkat T cells to spread on anti-CD3 coated coverslips and fixed them after 10 minutes after activation. The cells were stained for f-actin (with rhodamine phalloidin), non-muscle myosin 2A (with an antibody for the heavy chain of NM2A) and tubulin (with an antibody for beta-tubulin), and imaged using TIRF (Total Internal Reflection Microscopy) as shown in Figure 3.1a. For all cells, an IRM (interference reflection microscopy) image was taken to identify the contact zone of the cell and detect the cell contour and centroid. Fifty lines were drawn radially across the cell and the intensity profile for each line was obtained for each of the cytoskeletal proteins. Averaging the intensity profiles reveals patterns of intensity variations across the contact zone for all three cytoskeletal elements (Figure 3.1b). Based on the mean intensity profile of these proteins, we characterized the IS by three regions as shown in Figure 3.1c (also marked by the dashed lines in Figure 1b), and roughly consistent with earlier studies [85]. The central region (normalized radius < 0.4) largely depleted in actin and myosin, the peripheral region (0.4 < radius < 0.8) enriched in myosin and formin nucleated actin filaments [70] and the distal region (radius > 0.8) enriched in branched actin networks. The mean intensity of F-actin (Figure 1d), myosin (Figure 3.1e) and tubulin (Figure 3.1f) are significantly different across these regions.

91
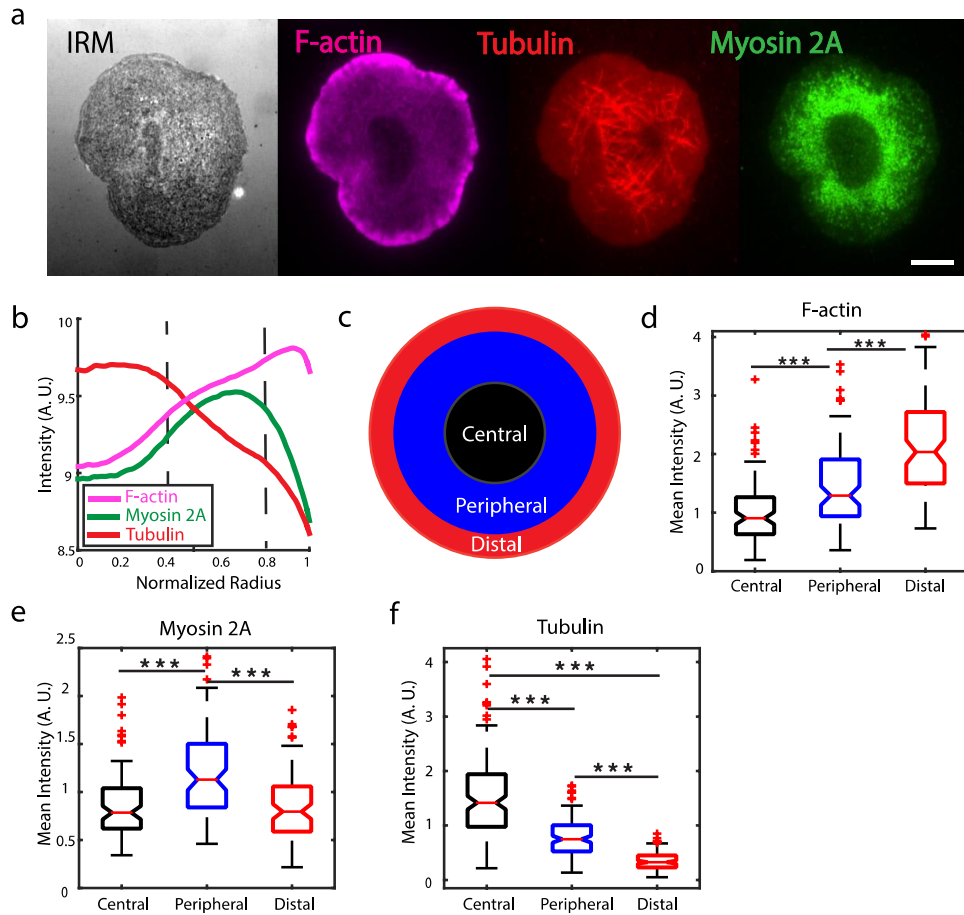
Figure 3.1. Cytoskeletal proteins are differentially distributed across the immune synapse. a) Interference reflection microscopy (IRM) and representative TIRF images of WT Jurkat T cells fixed 10 minutes after being activated on anti-CD3 coated glass coverslips. Cells were stained for filamentous actin (magenta), tubulin (red) and non-muscle myosin 2A (green). Scale bar is 5 μm. b) Average intensity profiles for the cytoskeletal proteins shown in a). The dashed lines demarcate regions with different characteristics of these cytoskeletal proteins. N = 90 cells. c) Schematic showing the three regions: the central region largely depleted in actin and myosin, the peripheral

region enriched in myosin and formin nucleated actin filaments and the distal region enriched in Arp2/3 nucleated actin meshworks. d) Mean intensity of F-actin at the contact zone measured in fixed cells for the regions defined in c: central (black), peripheral (blue) and distal (red) regions. e) Non-muscle myosin 2A mean intensity measured in fixed cells for the regions defined in c. f) Mean intensity of tubulin measured in fixed cells for the same regions. Significance of differences was tested using the Kolmogorov-Smirnoff test (***$p < 0.001$).

3.3 Microtubule growth rates are differentially modulated across different regions and by Arp2/3 and formin mediated actin architectures

Having defined specific regions at the IS, we next investigated whether microtubule growth rates are affected by the presence of different actin structures. We transiently transfected Jurkat T cells with EGFP-EB3, a microtubule-plus-end binding protein, and Td-Tomato-F-tractin, which labels polymerized actin filaments [140] to correlate MT growth and actin dynamics. The cells were activated on anti-CD3 coated coverslips and imaged with TIRF microscopy 5 minutes after being activated (Figure 3.2a). Cells were imaged for 5 minutes at two second intervals. We observed that the EB3 comets slowed down as they reached the actin-dense lamellipodial region (white arrow in the zoomed region of Figure 3.2a). To quantify the growth rates of MTs we tracked EB3 comets using the MATLAB-based tracking routine U-track [141]. To correlate EB3 dynamics with different IS regions, the inter-frame displacements were assigned to a specific region based on the coordinates of the final position at the second frame (Figure 3.2b).

93

We defined the instantaneous speed as the displacement between two consecutive frames divided by the time elapsed (2 seconds). We found that the instantaneous speeds of EB3 are similar in the central and peripheral regions (Figure 3.2c), but MT tips slow down as they reach the distal region with significantly lower instantaneous speed compared to central and peripheral (median speed: 0.053 μm/s in distal region, 0.082 μm/s in central region, 0.086 μm/s in peripheral region). From the time lapse movies we additionally observed a qualitative change in the direction of the EB3 tracks in the distal region. In order to quantify the directionality persistence of growing MT tips, we defined the "instantaneous angle difference" (Figure 3.2d) as the difference in angle between two consecutive displacements (as defined from an arbitrary line of reference). Figure 3.2e shows the cumulative probability of the instantaneous angle difference measured in each region. We found the distribution of angles in the central and peripheral regions to be nearly identical. However, the distal region presented significantly larger angles indicating that EB3 was more likely to change direction in the extreme periphery of the cell, leading to more curved tracks.

In order to examine how MT growth is affected by local actin dynamics in each region, we quantified the degree to which MT growth is radial. We defined the radial angle as the difference between the angle formed during an inter-frame displacement and the angle formed by a line connecting the centroid of the cell with the initial position of that displacement (Figure 3.2f). Small angles correspond to largely radial inter-frame

94

displacements while larger angles correspond to non-radial displacements. Figure 3.2g shows the cumulative probability distribution of the radial angle in the three regions. The distal region shows the largest angles indicating that MT growth is least radial in this region. We next investigated whether EB3 instantaneous speed depended on its direction. We classified the instantaneous speed as 'radial' whenever its radial angle was less than or equal to 45° and 'non-radial' for radial angles larger than 45°. We found that the non-radial speeds were significantly higher than the radial speeds in the distal region (Figure 3.2h), while the radial and non-radial speeds were similar in central and peripheral regions (Figure 3.6a, b – Supplementary material). The lower EB3 radial speeds observed in the distal region may be the attributed to the opposing force produced by the centripetal actin retrograde flow, which is highest in this region [85].

We next investigated how perturbing actin network dynamics affected EB3 instantaneous speeds. We used the small molecule inhibitors CK666 (5 minute incubation at 50 μM) for Arp2/3 inhibition and SMIFH2 (5 minute incubation at 25 μM) for formin inhibition. Figure 3.2i shows the cumulative distribution of EB3 instantaneous speeds for all regions in CK666, SMIFH2 and DMSO treated cells. The overall distributions show no significant differences between these conditions. We then examined the effect of these inhibitors at the previously defined regions. We found that in the peripheral region inhibition of Arp2/3 caused a moderate increase of speeds and that formin inhibition led to a modest but significant decrease in EB3 speeds (Figure

95

3.2j) but did not significantly change the speeds in the central region (Figure 3.6c –

Supplementary material) or in the actin-dense distal region (Figure 3.6d –

Supplementary material). Interestingly, the inhibition of these actin nucleators had

opposing effects on MT growth: formin inhibition led to a significant increase in radial

angles while Arp2/3 inhibition led to decreased radial angle (Figure 3.2k). This effect

was strongest at the distal region (Figure 3.2k) but qualitatively similar to the effect on

the peripheral region, while the effect on central region was negligible (Figure 3.6e, f

– Supplementary material). Finally, we found that neither formin nor Arp2/3 inhibition

had an effect on the distribution of instantaneous angle differences for any of the

regions (Figure 3.6g-i – Supplementary material).
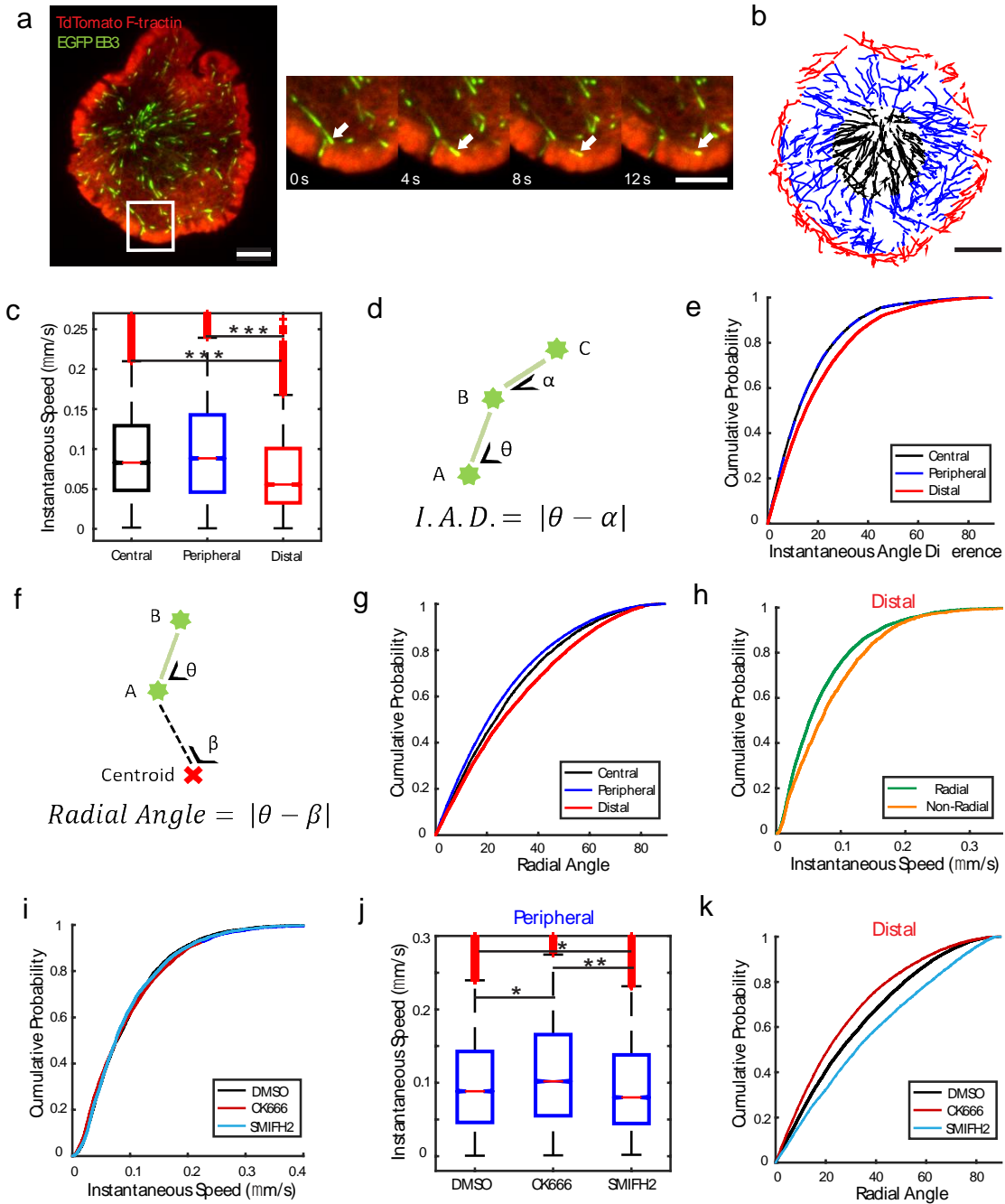
Figure 3.2. Microtubule growth rates are differentially modulated across different regions and by Arp2/3 and formin mediated actin architectures. a) Representative two-color image of a Jurkat cell transiently transfected with TdTomato-Ftractin (red)

and EGFP-EB3 (green). Scale bar is 5 μm. Higher magnification views at different time points of the region enclosed by the white square in the left-hand image are shown on the right. The white arrow points to a microtubule tip whose movement is drastically reduced once it reaches the actin-rich distal region. Scale bar is 3 μm. b) EB3 tracks color-coded for the region of the synapse where they occurred: central (black), peripheral (blue) and distal (red). c) Comparison of instantaneous speeds of EB3 across the three regions considered. N=11 cells. d) Diagram illustrating how the instantaneous angle difference is calculated from two consecutive inter-frame displacements within a trajectory (point A is the starting point and C the ending point). e) Cumulative distribution of instantaneous angle differences of EB3 tracks as a measure of directionality persistence in different regions. f) Diagram illustrating how the radial angle is calculated for an inter-frame displacement with respect to the cell centroid (represented by the red cross). g) Cumulative distribution of radial angles calculated from inter-frame displacements of EB3 tracks for the different regions. h) Cumulative distribution of instantaneous EB3 speeds in the distal region classified as radial (radial angle $\leq 45°$) or non-radial (radial angle $> 45°$). i) Cumulative distribution of EB3 instantaneous speeds for all regions in cells treated with the actin nucleation inhibitors CK666 (Arp2/3) or SMIFH2 (formin) compared with DMSO control. N = 11 cells for DMSO, N = 11 for CK666 and N = 16 for SMIFH2. j) Box plot of EB3 instantaneous speeds measured in the peripheral region comparing the same conditions as in i. k) Cumulative distribution of radial angles in the distal region for cells treated with

CK666, SMIFH2 compared with DMSO (carrier control),. Significance of differences was tested using the Kolmogorov-Smirnoff test ($***p < 0.001$, $**p < 0.01$, $*p < 0.05$).

3.4 Integrin engagement enhances the effect of formin inhibition on MT growth

Motivated by the observation that non-radial EB3 instantaneous speeds were higher in the distal region, where actin retrograde flow speed is highest, we next examined whether actin retrograde flow modulates MT growth. Integrin engagement, through linking of the integrin VLA-4 with VCAM-1, is known to reduce the speed of actin retrograde flow in Jurkat T cells [142, 143]. We thus decided to study the effect of integrin engagement, and subsequent slowdown of actin flow, on EB3 dynamics and how this was influenced by different actin architectures. We activated Jurkat T cells on coverslips coated with anti-CD3 and VCAM-1 and fixed the cells 10 minutes after activation (Figure 3.3a). Analysis of the IRM images showed that integrin coating did not affect the spread area of the cells when compared to cells on anti-CD3-only substrate (Figure 3.7a – Supplementary material). We characterized the actin and myosin distributions by immunostaining and found that the dense lamellipodial region had shrunk significantly as indicated by the white arrows in Figure 3.3a. The average actin and myosin intensity profiles along the normalized cell radius (Figure 3.1b) show a loss of the previously defined actin-rich distal region. We therefore classified the contact zone into two regions: the central region was defined as before (radius < 0.4, dashed line in Figure 3.3b) and the peripheral region (radius > 0.4, which combines the previously defined peripheral and distal regions, Figure 3.3c). Myosin is significantly

99

more abundant in the peripheral region (Figure 3.3d) while F-actin accumulation is not significantly different between the two regions (Figure 3.3e), in contrast to the case for anti-CD3 coating alone which showed significant differences for all three proteins in the different regions. Interestingly, the presence of VCAM-1 on the activating substrate induced a significant increase in the amount of F-actin over the entire contact zone (Figure 3.3f).

We next imaged live cells activated on coverslips coated with anti-CD3 and VCAM-1 and tracked EB3 tips as described before. We found that the instantaneous speed distribution of EB3 across all regions was similar for CD3 and CD3+VCAM-1 cases (Figure 3.7b – Supplementary material). Furthermore, comparison of instantaneous speeds between the two regions also showed no significant differences (Figure 3.3g). We next investigated the influence of actin nucleation inhibitors on MT growth rates for cells activated on anti-CD3+VCAM-1 coated coverslips. Figure 3.3h shows the cumulative probability distribution of EB3 instantaneous speeds across all regions for cells treated with CK666 or SMIFH2 compared with DMSO control. Cells treated with CK666 displayed slightly but significantly higher speeds than DMSO while SMIFH2 caused a strong reduction in the speeds as compared to control. The effect described was also observed for both the central and peripheral regions as shown in Figure 3.3i and Figure 3.3j respectively. We had observed an 8% reduction in the median speed for SMIFH2 treated cells in the peripheral region for cells on anti-CD3 substrates (DMSO median speed 0.086 μm/s, SMIFH2 median speed 0.079 μm/s). Upon integrin

engagement with VCAM, we found that SMIFH2 treatment resulted in a significantly larger reduction (34% - DMSO median speed 0.084 μm/s, SMIFH2 median speed 0.055 μm/s). Our results thus suggest that integrin engagement enhances the effect of formin inhibition on MT tip dynamics. We also found that formin inhibition led to larger changes in direction and less radial trajectories, as measured by instantaneous angle difference and radial angle distributions respectively for both peripheral (Figure 3.3k, l) and central regions (Figure 3.7c, d – Supplementary material).

Taken together, these results show that integrin engagement, upon addition of VCAM-1 to the activating surface, led to significantly larger changes in speed and directionality with Arp2/3 or formin inhibition, in contrast to anti-CD3 only engaged cells.
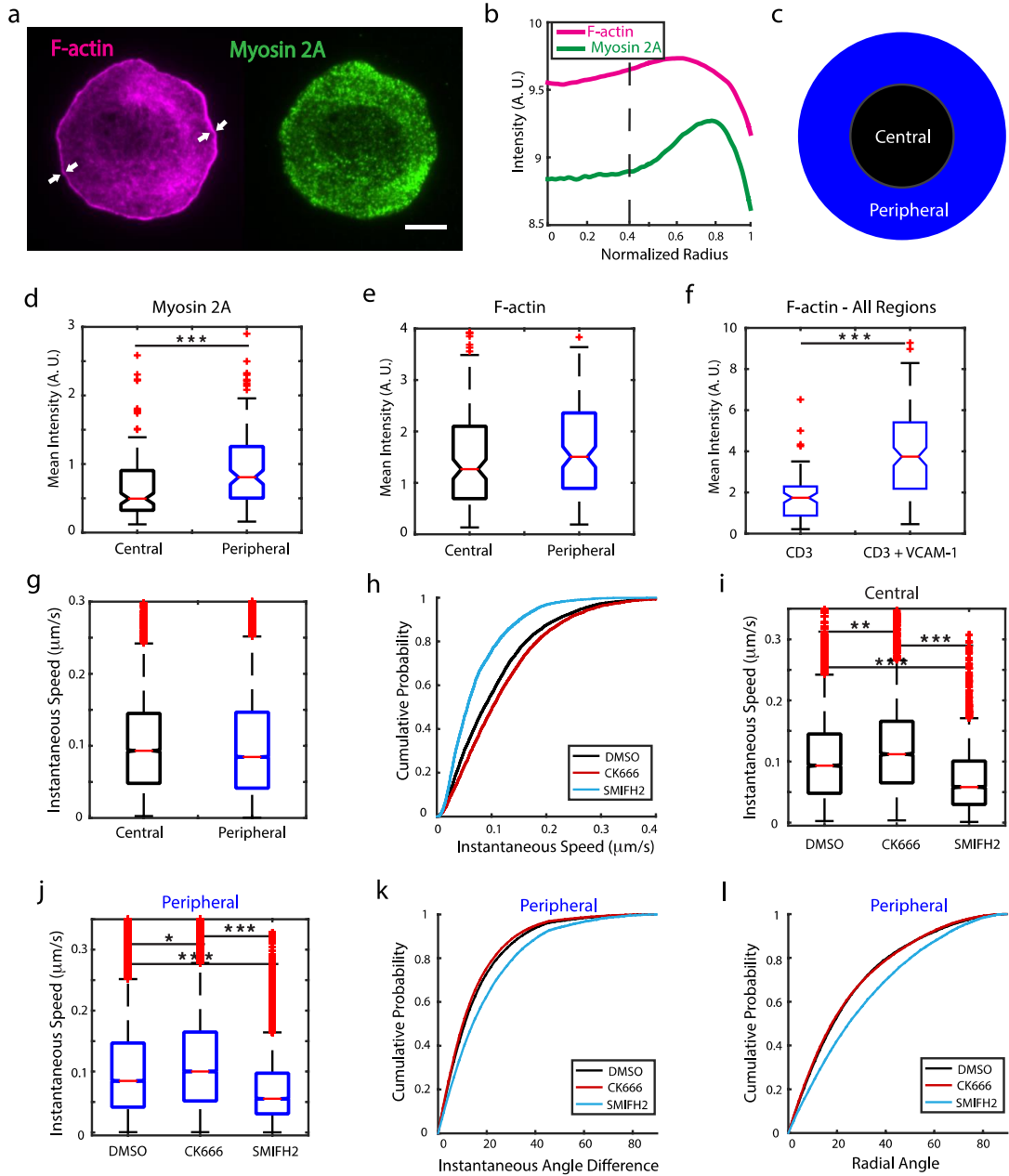
Figure 3.3. Integrin engagement enhances the effect of formin inhibition on MT growth. a) Representative TIRF images of WT Jurkat cells fixed 10 minutes after activation on a glass substrate coated with anti-CD3 and VCAM-1 and immunostained for filamentous actin (magenta) and non-muscle myosin 2A (green). White arrows

point to the narrow lamellipodial region typically displayed by cells under these conditions. Scale bar is 5 μm. b) Average intensity profile for the cytoskeletal proteins shown in a. The dashed line denotes the empirical choice of boundary between the central and peripheral regions. N = 134 cells. c) Schematic showing two regions: the central region depleted in myosin and peripheral region enriched in myosin and actin. d) Mean fluorescence intensity of myosin at the contact zone for central (black) and peripheral (blue) regions. e) Comparison of the F-actin mean intensity for central (black) and peripheral (blue) regions. f) Comparison of the level of F-actin at the contact zone of the whole cell as measured by rhodamine-phalloidin mean intensity for cells activated with anti-CD3 alone and activated with anti-CD3 + VCAM-1. N = 90 cells for CD3 and N = 134 cells for CD3+VCAM-1. g) Comparison of EB3 instantaneous speeds measured at central and peripheral regions in cells activated on CD3+VCAM-1 substrates. h) Cumulative distribution of instantaneous speeds of EB3 across all regions for cells treated with CK666 or SMIFH2 compared with DMSO control. N = 12 cells for DMSO, N = 16 cells for CK666 and N = 20 cells for SMIFH2. i) EB3 instantaneous speeds in the central and j) peripheral region for cells treated with actin nucleation inhibitors CK666 and SMIFH2. k) Cumulative distribution of instantaneous angle differences and l) radial angles in the peripheral region for cells treated with CK666 and SMIFH2 as compared to DMSO (carrier control). Significance of differences was tested using the Kolmogorov-Smirnoff test (***$p < 0.001$, **$p < 0.01$, *$p < 0.05$). For h) SMIFH2 is significantly different from DMSO

($p<0.0001$) and CK666 is different from DMSO ($p<0.01$). For k) and i) SMIFH2 is significantly different from DMSO and CK666 ($p<0.001$).

3.5 Actomyosin dynamics regulates MT filament dynamics

Previous work suggests that fluctuations induced by actomyosin forces on MT tip growth lead to overall fluctuations and shape changes of MT filaments [144, 145]. These forces may in turn be dependent on the local architecture of the actin networks induced by different nucleating proteins. In order to better understand the interaction between the different actin networks and microtubules, we visualized microtubule filament shape and dynamics and examined the effect of perturbing specific actin network architectures. Jurkat T cells were transiently transfected with EGFP-EMTB (ensconsin microtubule-binding domain), a microtubule associated protein that does not modulate MT dynamics [146]. Cells were activated on anti-CD3 coated coverslips and imaged five minutes after activation at 2 second intervals using instant Structured Illumination Microscopy (iSIM) [44] to obtain highly resolved images of MT filaments. We observed that MTs at the periphery of the cell (equivalent to the peripheral plus distal region defined in Figure 3.1 were more dynamic than those at the center (equivalent to central region in Figure 3.1). Figure 3.4a shows the maximum intensity projection of a 30-frame time-lapse movie of MTs color-coded for time. In the central region of the cell, the filaments appear white due to the superposition of the filaments at different time points while the filaments at the periphery appear at different positions and colors, indicating their higher dynamics. In order to quantify MT filament dynamics, we chose two ROIs of 3x3 μm at the center and at the periphery of each cell (as indicated by the boxes in Figure 3.4a). We computed the temporal autocorrelation of the intensity profile along each row of pixels in the boxed region. The typical

correlation amplitude curves obtained for a central ROI are shown in Figure 3.4b and for a peripheral ROI in Figure 3.4c. For all curves obtained, the correlation amplitude decays over time, reaching roughly zero (no correlation) at later times. We noticed that the correlation amplitude decays faster at the periphery, which is consistent with the visually observed higher dynamics of the filaments in this region. To characterize the correlation decay we calculated the average correlation curve for an ROI and fit the curve to a double exponential of the form: $C(t) = ae^{-bt} + ce^{-dt}$. We set the fit parameter a equal to 1 since it corresponds to the correlation at $t = 0$, then parameter b provides the correlation decay rate. Our data was well fit by this relation as shown by sample fits in Figure 3.4d and 3.4e corresponding to individual ROIs and as evaluated by the distribution of fit residuals, which is normal, narrow and centered on zero (Figure 3.8a – Supplementary material) in contrast to the right skewed residuals obtained from a single exponential fit (Figure 3.8b – Supplementary material). We found that the correlation decay time (as evaluated for two ROIs per region of each cell) was significantly higher in the central region of the cell than in the peripheral region as shown by the distribution of values of parameter b^{-1} in Figure 3.4f. The distribution of values for fit parameters c and d, which correspond to the correlation amplitude and decay rate at later times, was very similar for central and peripheral regions and across all the conditions explored (Figure 3.8c, d – Supplementary material). We next investigated the effect of the actin nucleation inhibitors CK666 (Arp2/3 inhibition) and SMIFH2 (formin inhibition) on MT filament dynamics as shown in Figure 3.4g. We found that perturbing either actin network induces a significant increase in the correlation decay time (implying decreased dynamics) for ROIs at the periphery of the cell, with little effect on MT dynamics in the central region. This indicates that both Arp2/3 and formin mediated networks are important to sustain MT filament

dynamics. Notably, while the correlation decay time at the periphery was reduced for CK666 and SMIFH2 treated cells, in both cases the correlation decay time was still larger than that at the center, indicating that MT filaments are more dynamic at the cell periphery even with inhibition. In order to explore the role of myosin in MT filament dynamics we used the ROCK kinase inhibitor Y27632, which prevents myosin phosphorylation and associated cell contractility. Cells treated with Y27632 also displayed less dynamic microtubules, particularly at the periphery, as measured by the significant increase in correlation decay time (Figure 3.4h), indicating that myosin contractility modulates MT dynamics. Finally, we asked whether actin retrograde flow influences MT filament dynamics. We applied the same analysis to time-lapse movies of activated cells on anti-CD3+VCAM-1 coated coverslips and found that the correlation decay time is significantly lower for MTs at the periphery compared with MTs at the central region (Figure 3.4i). Interestingly the MT dynamics in both regions were very similar to that observed in the corresponding regions of cells on anti-CD3 coverslips (data not shown). Thus integrin engagement does not appear to alter filament dynamics.
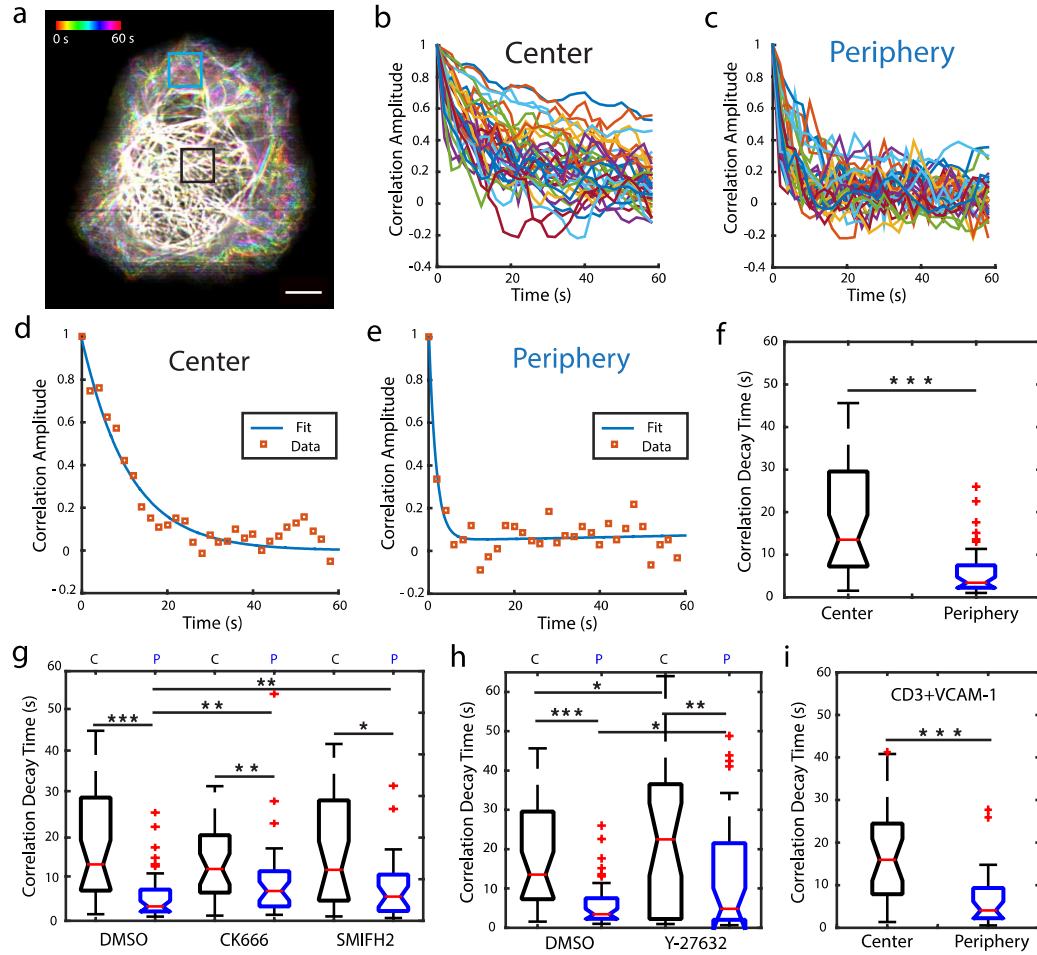
Figure 3.4. Actomyosin dynamics regulate MT filament dynamics. a) Maximum intensity projection of a 30-frame time-lapse movie, taken at 2 second intervals, color-coded for time. Scale bar is 5 μm. b) Representative plots of the correlation amplitude decay of the fluorescence intensity per pixel row over time for the region enclosed in black in panel a, corresponding to the center and c) for the peripheral region (blue square in a. d) Ensemble average correlation values calculated from a sample ROI in a cell (red squares) from the center and e) from the periphery. Solid lines show double-exponential fits to the data. f) Comparison of correlation decay times, obtained from

the fits, for the central and peripheral regions. N =18 cells, 2 ROIs per cell for each region. g) Comparison of the distribution of correlation decay times for central and peripheral regions in cells treated with CK666 and SMIFH2 with DMSO (vehicle control). N = 18 for DMSO, N= 19 for CK666 and N = 15 for SMIFH2. h) Box plots of correlation decay times comparing cells treated with the Rho-kinase inhibitor Y-27632 and with DMSO (vehicle control). N = 18 for DMSO, N=17 cells for Y-27632. i) Comparison of correlation decay times in the center and periphery for cells in CD3+VCAM-1 substrates. N=14 cells. Significance of differences was tested using the Kolmogorov-Smirnoff test (***$p < 0.001$, **$p < 0.01$, *$p < 0.05$).

3.6 MT filament deformation is modulated by actin dynamics and myosin contractility

From the movies taken for the filament dynamics analysis, it was evident that the filaments in the peripheral region exhibited more deformed shapes than those at the center. We therefore investigated the spatial distribution of microtubule filament deformations at different regions and under different perturbations to elucidate the role of actomyosin dynamics on filament shapes. For this analysis we used timelapse iSIM images, as shown in Figure 3.5a. For each cell, we manually traced individual MT filaments from three image frames taken 30 seconds apart (to ensure that MT shapes were uncorrelated). Each filament traced was assigned to the central or peripheral region of the cell based on the coordinates of its center of mass. Figure 3.5b shows a collection of filaments traced from different superimposed cells with the peripheral

108

filaments shown in blue and the central ones shown in black. The filaments traced in both regions have a similar distribution of lengths (Figure 3.5c). To quantify MT deformations, we first calculated the deformation index, which is the ratio of the filament contour length to the end-to-end distance. We found that filaments at the periphery have a significantly higher deformation index than those at the center as shown in Figure 3.5d. In order to examine in more detail the filament shapes in both regions, we quantified the local curvature (see Methods) over segments of ~ 0.4 μm in length. The distribution of local curvatures is shown in Figure 3.5e and confirms our qualitative observations that MTs at the periphery display higher deformation than those at the center. A visual representation highlighting this difference is shown in Figure 3.5f, where the filaments in Figure 3.5b have been plotted with each segment color coded for the local curvature value. Higher deformations (yellow) are observed mostly at the periphery while lower curvature values (blue) are observed at the center. We then investigated the effect of CK666 and SMIFH2 treatments on filament shapes. We found that both inhibitors reduced the local curvatures for filaments at the periphery, with SMIFH2 showing a stronger effect (Figure 3.5g), indicating that both types of actin networks play a role in modulating MT filament shape. Central microtubule shapes were largely unaffected by these inhibitions, though CK666 caused a small but significant increase in deformation (Figure 3.9a – Supplementary material). Given the known role of myosin in the generation and maintenance of formin-mediated cable-like actin filaments, we next investigated the role of myosin in filament deformation. We inhibited myosin activity using the ROCK kinase inhibitor Y27632

which prevents myosin phosphorylation. We found that inhibition of myosin activity significantly reduced the local curvature distribution of filaments at the periphery (Figure 3.5h) and to a lesser extent at the center (Figure 3.9b – Supplementary material) as compared to DMSO control. Figure 3.5i shows the collection of filaments traced in cells treated with Y27632 color-coded for curvature. The filaments exhibit lower local curvature (as seen from the higher fraction of blue in the plot) than those in Figure 3.5f. Our results suggest that filament deformation is highly influenced by acto-myosin contractility.
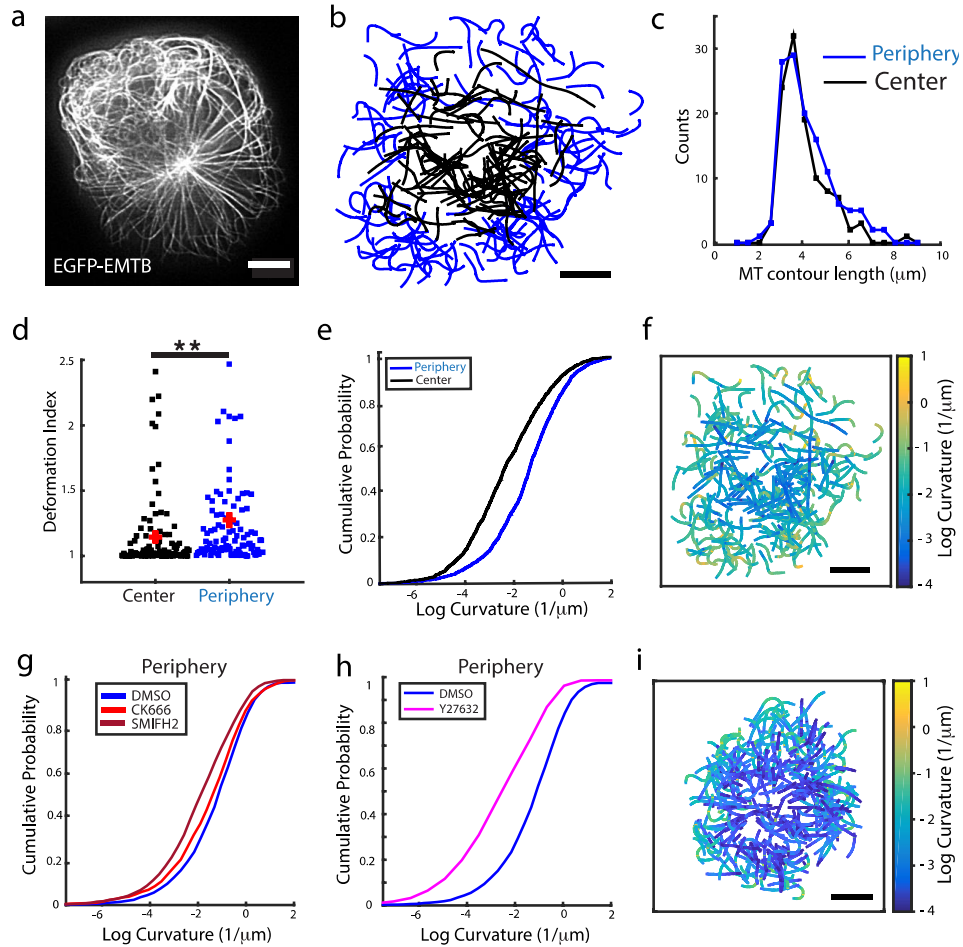
Figure 3.5. MT filament deformation is modulated by actin dynamics and myosin contractility. a) Representative iSIM image of a Jurkat T cell transiently transfected with EGFP-EMTB. b) Segmented MT filament traces from different cells color-coded for the region they belong: black for center and blue for periphery. c) Histogram of the distribution of the MT contour lengths for the traces used for analysis. d) Comparison of the deformation index (ratio of contour length to end-to-end distance) for filaments in the center and periphery. e) Cumulative probability plots of local curvature distributions of central and peripheral filaments. f) Plot of the filaments shown in panel

b color-coded for the local curvature. g) Cumulative probability plots of local curvature distribution of peripheral filaments in cells treated with CK666 (red) and SMIFH2 (brown) as compared to DMSO control (blue). N = 18 for DMSO, N= 19 for CK666 and N = 15 for SMIFH2. h) Cumulative distribution plot comparing the local curvature of peripheral filaments in cells treated with Rho-kinase inhibitor Y27632 (magenta) with DMSO control cells (blue). N = 17 for Y27632. i) Plot of filaments traced in cells treated with Y27632 color-coded for the local curvature. All scale bars are 5 μm. Significance of differences was tested using the Kolmogorov-Smirnoff test ($**p < 0.01$). For e) curvatures in the periphery and center are significatively different ($p<0.0001$). For g) the difference between curvatures in DMSO and CK666 is significant ($p<0.05$) and the difference between DMSO and SMIFH2 is significant ($p<0.001$). For h) the curvatures in DMSO and Y-27632 are significantly different ($p<0.0001$). All scale bars are 5 μm.

3.7 Discussion

Here, we used high-resolution fluorescence microscopy and quantitative image analysis to characterize the growth and shape deformation dynamics of microtubules across the different regions of the immune synapse and under chemical perturbations of specific actin architecture networks. I would like to highlight that the imaging techniques used in this study, TIRF and iSIM, have allowed us to push the boundaries and look at cytoskeleton dynamics with high spatial and temporal resolution. More detailed information regarding the imaging techniques employed in this study is

112

provided in Appendix A of this thesis. The spatially segregated cytoskeletal architecture displayed by activated T cells makes them an ideal model system to explore the influence of different actin networks on microtubule dynamics. We found that microtubule growth rates were reduced in the actin-dense distal region. Additionally, MTs growing in this region showed lower directionality persistence and were less radial. The actin cortex of Jurkat cells is about 200 nm thick [147] and TCR activation induces actin polymerization and enrichment at the contact zone - particularly at the lamellipodial (distal) region, further increasing the actin density. It is thus likely that the slowdown of MT tips in this region is the result of crowding by the actin meshwork, leading to spatial and temporal constraints on MT filament growth and possibly reducing the diffusivity of tubulin dimers and other proteins involved in MT filament polymerization. Furthermore, the fact that neither formin nor Arp2/3 inhibition caused changes in MT tip speeds in this region suggests that crowding or confinement is the dominant factor independent of the prevalence of either actin architecture. Interestingly, MT growth rates were differentially modulated by the actin nucleators formin and Arp2/3 in the peripheral region of the cell. Arp2/3 inhibition caused a moderate increase in speeds of the MT tip marker EB3 while formin inhibition led to slower EB3 speeds. There exists a balance between the actin networks produced by Arp2/3 and formin - inhibition of one of these nucleators leads to enrichment in actin structures formed by the other. Thus, formin inhibition leads to an increase in branched actin meshworks produced by Arp2/3 [70] leading to a more intricate network that may enhance the physical barrier for microtubule growth. The FH2 and DAD

113

domains of formins allow them to interact directly with microtubules and MT associated proteins [10]. Indeed MT growth can be guided along actin bundles [94] and formins can nucleate actin from growing microtubule ends [96]. It is thus possible that the observed increase in MT growth rates after Arp2/3 inhibition is not only caused by the removal of a physical barrier but also due to a synergistic interaction between MTs and formin nucleated actin cables.

We found that integrin engagement changes the morphology of the actin cytoskeleton in activated T cells. Jurkat cells activated on VCAM-1 coated substrates displayed a much thinner lamellipodial region, more homogeneous actin distribution across the contact zone and higher F-actin density (two-fold increase in the median) compared to cells activated on CD3-only substrates. Interestingly, the inhibition of formin upon integrin engagement with VCAM caused a strong reduction in MT tip speeds (higher than the effect of formin inhibition in cells on CD3-only substrates), fewer radial EB3 trajectories and decreased persistence in directionality. This effect was evident across both regions (central and peripheral) of the cell. Arp2/3 inhibition of integrin-engaged cells led to faster growing tips, again showing the opposite effect compared to formin inhibition. Our results suggest that formin inhibition leads to the increase of Arp2/3 nucleated actin networks and a more-dense physical barrier for MT growth. It is intriguing that integrin engagement enhances the effect of formin inhibition in MT growth dynamics. The higher actin density may play a role; however since the increased actin density did not affect overall growth dynamics in untreated cells, this

114

suggests the balance between the two actin architectures and their spatiotemporal organization may be the most relevant factor in determining MT growth speeds.

Microtubule filaments in the peripheral actomyosin-rich region are more dynamic and display more deformed shapes than those located in the central region. MT density is highest in the central region, which is likely due to the docking of the centrosome near the center of the contact zone. Microtubules in this region appear more bundled and their proximity to the centrosome is likely to restrict their movement. However, we qualitatively observed similar spatial effects on the dynamics and deformations of peripheral and central filaments even in cells for which the centrosome had not polarized (the centrosome was not near the contact zone – data not shown). This suggests that the differences in MT dynamics cannot be attributed only to centrosome positioning. Furthermore, the inhibition of actin nucleators and myosin affected the dynamics and shapes of peripheral microtubules but not central ones. Thus, the deformation of MTs and their shape fluctuations are modulated by the actomyosin cytoskeleton. The inhibition of Arp2/3 and formin had similar effects, resulting in less dynamic microtubules at the periphery as reported by the increase in correlation times. Interestingly, integrin engagement and associated reduction in actin retrograde flow did not have an impact on the correlation times of fluctuating MTs. This suggests that a different dynamic property of the actin cytoskeleton modulates MT dynamics. Actomyosin contractility is likely to be responsible since inhibition of myosin activity led to significantly less deformed and less dynamic microtubules in the peripheral

115

region and to a lesser extent in the central region. Actin architecture plays an important role in the transmission of forces produced by associated myosin motors and the spatial arrangement and physical properties of the actin network are key to tension regulation [148, 149]. Thus, the decrease of MT dynamics caused by inhibition of formin or Arp2/3 is likely associated with an overall disruption of actin network connectivity and the resultant decrease in myosin-generated tension and contractility.

Post-translational modification of microtubules can influence their physical properties and dynamics. TCR activation leads to detyrosination of the α-tubulin subunit, which requires the formin INF2. Detyrosinated microtubules are more stable and facilitate centrosome repositioning [150]. TCR signaling also induces transient deacetylation of MTs at early times (2-5 min) and enhanced acetylation at later times [151]. Tubulin acetylation is performed by acetyltransferase TAT1 in the lumen of filaments. Acetylated microtubules are mechanically more resistant due to their higher plasticity [152]. We found that the ratio of acetylated tubulin to total tubulin did not change (Figure 3.10a, b – Supplementary material) across the IS regions (central, peripheral and distal), thus microtubule acetylation is uniform and unlikely to be responsible for the differences in curvatures between peripheral and central microtubules.

The high curvature displayed by peripheral MTs was decreased upon inhibition of Arp2/3 and formin. The latter had a stronger effect suggesting that the deformation is associated with the contractility produced by actomyosin arcs. This is supported by the

116

even stronger reduction in curvatures produced by the inhibition of myosin activation. The dense actin network surrounding microtubules allows them to withstand compressive forces [153]. It is interesting that the actin networks which facilitate the transmission of the forces produced by myosin also provide mechanical reinforcement to the microtubules counteracting these forces. Our results indicate that there is a mechanical balance between the microtubule and actin cytoskeleton and that different actin architectures modulate microtubule dynamics in distinct ways.

3.8 Methods

3.8.1 Substrate preparation

Coverslips attached to 8 well Labtek chambers were incubated in Poly-L-Lysine (PLL) at 0.01% W/V (Sigma Aldrich, St. Louis, MO) for 10 min. PLL was aspirated and the slide was left to dry for 1 hour at 37 °C. T cell activating antibody coating is performed by incubating the slides in a 10 μg/ml solution of anti-CD3 antibody (Hit-3a, eBiosciences, San Diego, CA) for 2 hours at 37 °C or overnight at 4 °C. For VCAM-1 coating, the coverslip was first washed with 1X PBS to remove excess antibody and then incubated with VCAM-1 solution (Sino Biological) at 2 μg/ml concentration for 2 hours at 37 °C. Excess anti-CD3 or VCAM-1 was removed by washing with L-15 imaging media right before the experiment.

3.8.2 Cell culture and transient transfections

E6-1 Jurkat cells were cultured in RPMI 1640 supplemented with 10% fetal bovine serum and 1% Penn-Strep antibiotics. For transient transfections we used the Neon (ThermoFisher Sci.) electroporation system two days before the experiment. The protocol is as follows: $2x10^5$ cells are resuspended in 10 µl of R-buffer with 0.5-2 µg of the plasmid. The cells are exposed to 3 pulses of 1325 V amplitude and 10 ms duration in the electroporator. Cells are then transferred to 500 µl of RPMI 1640 supplemented with 10% fetal bovine serum and kept in the incubator at 37 °C. EMTB–3×EGFP was a gift from William Bement (Addgene plasmid # 26741). The TdTomato-F-tractin plasmid was a gift from Dr John A Hammer and the EGFP-EB3 was a gift from Dr Robert Fisher.

3.8.3 Immunofluorescence

Cells were activated on anti-CD3 coated coverslips and fixed after 10 minutes of activation using 4% paraformaldehyde (PFA) for 10 minutes at room temperature and then washed thoroughly with 1X PBS. Cells were then permeabilized for 5-10 minutes with a 0.15 % Triton X solution and blocked with a BSA (0.02 g/ml) and Glycine (0.3 M) in 1X PBS solution for 1 hour at room temperature. For incubation periods and concentrations of primary and secondary antibodies, we followed the manufacturers recommendations. For F-actin labeling, we used Acti-stain 670 phalloidin from Cytoskeleton. For labeling Myosin 2A we used the heavy chain non-muscle myosin 2A antibody from Biolegend. For microtubule labeling we used the beta tubulin antibody from Invitrogen.

118

3.8.4 Microscopy

TIRF imaging was performed on an inverted microscope (Nikon Ti2000 PFS) equipped with a 1.49 numerical aperture 100× lens for TIRF imaging and a Prime BSI camera (Photometrics). Imaging protocols were implemented using the software Elements from Nikon and images were cropped using Fiji before further analysis using MATLAB scripts. Imaging of EGFP-EMTB expressing Jurkat cells was performed using iSIM, with a 1.42 numerical aperture 60× lens (Olympus), a 488 nm laser for excitation with 200 ms exposure times and a PCO Edge camera. Cells were added to the activating substrate and allowed to spread for 5 minutes, then time-lapse images were taken at 2 s intervals. Images obtained were post processed with background subtraction and deconvolution. The final lateral resolution for deconvolved images is between 140 and 150 nm. The Richardson–Lucy algorithm is used for deconvolution, and run for ten iterations. The PSF used was simulated by a Gaussian function but based on parameters obtained from measurement, i.e., the FWHM of the PSF used is the same as the FWHM measured.

3.8.5 Inhibitor experiments

For all inhibitor experiments, cells were incubated for 5 minutes in an inhibitor and L-15 solution at 37° C and at the indicated concentration. After the incubation period cells were added to the imaging chamber, which had L-15 and the inhibitor at the same

concentration. Cells were allowed to spread for 5 minutes before imaging. CK666 (Calbiochem) was used at 50 µM, SMIFH2 (Sigma-Aldrich) was used at 25 µM and Y27632 (Calbiochem) was used at 100µM. For vehicle control experiments, cells were incubated for 5 minutes in a DMSO and L-15 solution at 0.01 % concentration and the same concentration was kept in the imaging chamber.

3.8.6 Data analysis

For image analysis all cell images were cropped using Fiji and then post-processed and analyzed using MATLAB custom scripts. For cytoskeletal profile analysis, the IRM image was used to generate a mask and detect the cell contour. Based on this mask the fluorescence intensity in the other channels (corresponding to F-actin, tubulin and myosin) was quantified. To determine the intensity per region, we assigned each pixel to a region based on its location. The distance between each pixel within the mask and the cell centroid was computed. Then we computed the distance between the cell centroid and a point along the cell contour that was closest to the pixel in question to obtain an effective radius. The pixel is then assigned to a region based on the ratio of the pixel-to-centroid distance and the effective radius.

EB3 speeds were analyzed using the MATLAB-based routine U-track [141] was used. First, the timelapse movie of EB3 tip dynamics was saved as an image sequence using Fiji. Images were loaded into U-track by adding them as a new channel in their Movie editing window. For particle detection the Comet Detection option was selected, with

a low-pass of 4 pixels and high-pass of 7 pixels for the Gaussian standard deviation. For the tracking portion of the routine, the maximum gap to close (number of frames that a particle is allowed to disappear) selected was 2 frames and the lower and upper bound for the frame-to-frame linking were 3 and 8 pixels respectively. No segment merging or splitting was selected. For analysis of tracks to obtained relevant quantities we used a customized MATLAB routine. EB3 tracks shorter than 4 frames were rejected. The inter-frame displacements were assigned to a region based on the coordinates of the final position of the two-frame displacement and using the criteria described above for assigning a pixel to a region.

For microtubule shape analysis, filaments were traced by hand using the segmented line tool in Fiji. The spline fit option was selected to obtain a smoothed filament and the coordinates of the filament were imported to MATLAB. To assign a filament to a region, the image from which the filaments were traced was segmented and processed to obtain the cell contour and centroid. The distance between the centroid of the cell and the filament centroid D_{C-MT} was calculated (Figure 3.11a – Supplementary material). Then the distance between the centroid of the cell to the closest point to the MT centroid along the cell edge D_{C-CE} was calculated. If the ratio D_{C-MT}/D_{C-CE} is equal or less than 0.4 the filament is assigned to the central region, otherwise is assigned to the peripheral region (Figure 3.11b – Supplementary material). To calculate the curvature of microtubules the filament coordinates were coarse-grained to an average spacing of 7 pixels (0.385 µm) using a custom algorithm to reduce the contributions

121

from errors during data collection procedures [154]. Filament curvature was calculated

using the equation $\kappa = \left| \frac{\Delta\theta(s)}{(\Delta s_1 + \Delta s_2)/2} \right|$, where κ is the local curvature, $\Delta\theta(s)$ is the angle

between two adjacent filament segments and Δs_1, Δs_2 are the segment contour lengths

[155].

3.8.7 Statistical analysis

For statistical comparisons the two-sample Kolmogorov-Smirnov test was applied,

which compares whether two data samples come from the same continuous distribution

[156]. The test was implemented over 200-500 values data subsets randomly extracted

from the distributions for comparison. To compare data from conditions 1 and 2, for

example, two randomly selected data subsets were extracted for condition 1 and one

subset from condition 2. Then the test was applied comparing each subset from

condition 1 to the subset from condition 2 and then against each other. The size of the

data subset was chosen such that it qualitatively overlaps with the original distribution

and the mean and median were similar.

3.9 Supplementary Material
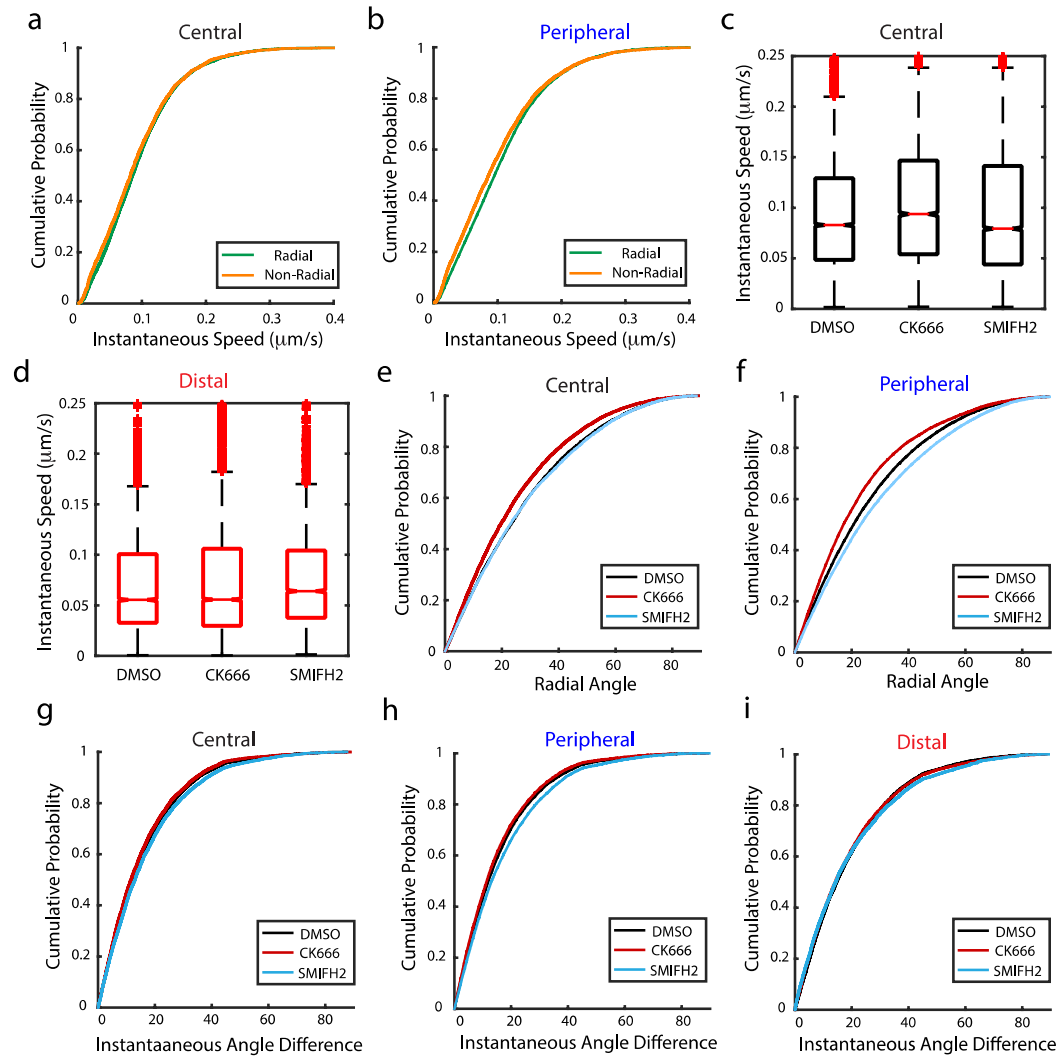
Figure 3.6. Cumulative distributions of instantaneous EB3 speeds classified as radial (radial angle $\leq 45°$) or non-radial (radial angle $> 45°$) for central (a) and peripheral (b) regions in DMSO control cells. c) Comparison of EB3 instantaneous speed measured in the central and d) peripheral region for cells treated with actin nucleation inhibitors CK666 or SMIFH2 with DMSO control. e) Cumulative distribution of radial angles for cells treated CK666 and SMIFH2 as compared to DMSO control in the central and f)

peripheral regions. g, h, i) Cumulative distribution plots of instantaneous angle differences for central, peripheral and distal regions respectively. Significance of differences was tested using the Kolmogorov-Smirnoff test. For e) CK666 was significantly different from DMSO and SMIFH2 ($p<0.01$) and for f) DMSO, CK666 and SMIFH2 were significantly different from each other ($p<0.01$).
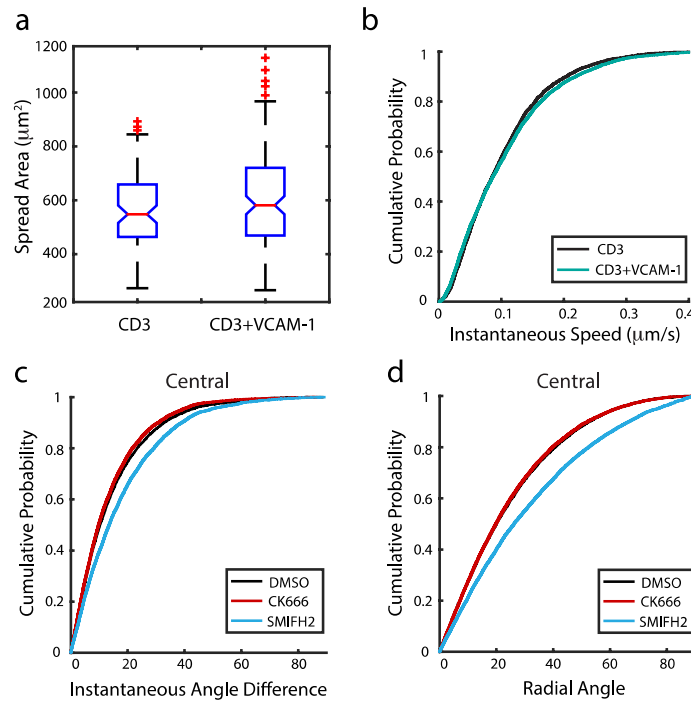
Figure 3.7. a) Plots of the spread area measured with IRM of cells fixed on anti-CD3 and on glass coated with anti-CD3 + VCAM-1. b) Cumulative distribution of instantaneous speeds of EB3 across all regions for cells activated on CD3 or CD3+VCAM-1 substrates. c) Cumulative distribution of instantaneous angle difference and e) radial angles in the central region for cells treated with CK666 and SMIFH2 as compared to DMSO (carrier control). Significance of differences was

124

tested using the Kolmogorov-Smirnoff test. SMIFH2 was significantly different from DMSO and CK666 ($p<0.001$) for both, radial and instantaneous angle differences.
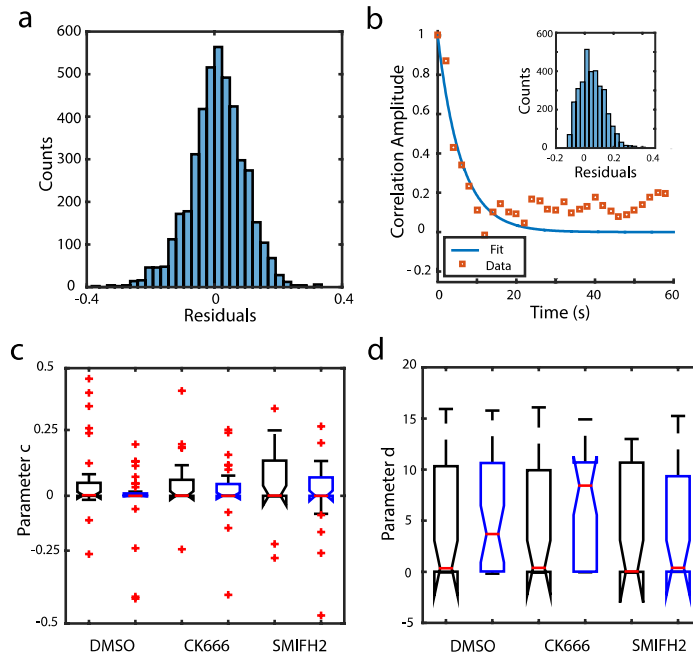
Figure 3.8. a) Distribution of residuals from double-exponential fit to correlation curves from DMSO cells. b) Sample single exponential fit for a correlation curve from the peripheral region of a DMSO-treated cell. Inset plot shows the distribution of residuals from single-exponential fit to correlation curves from DMSO cells. c) Plots of the amplitude of the second component (Parameter c) of the double exponential fit for central (black) and peripheral (blue) regions for cells treated with DMSO, CK666 and SMIFH2. d) Plots of the second correlation time (Parameter d) for the conditions described above.
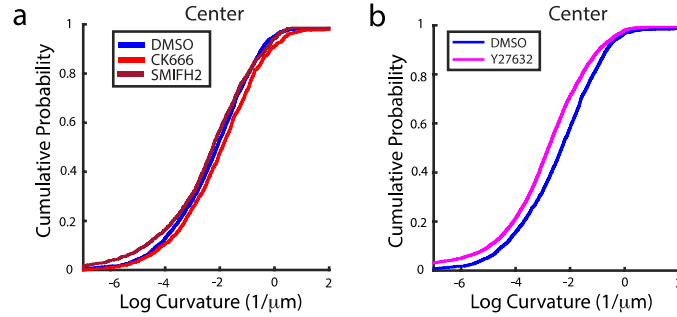
Figure 3.9. a) Cumulative probability plots of local curvature distribution measured for central MT filaments in cells treated with DMSO (control), CK666 and SMIFH2. b) Cumulative distribution plot comparing the local curvature of central filaments in cells treated with Rho-kinase inhibitor Y26732 (magenta) with DMSO control cells (blue).
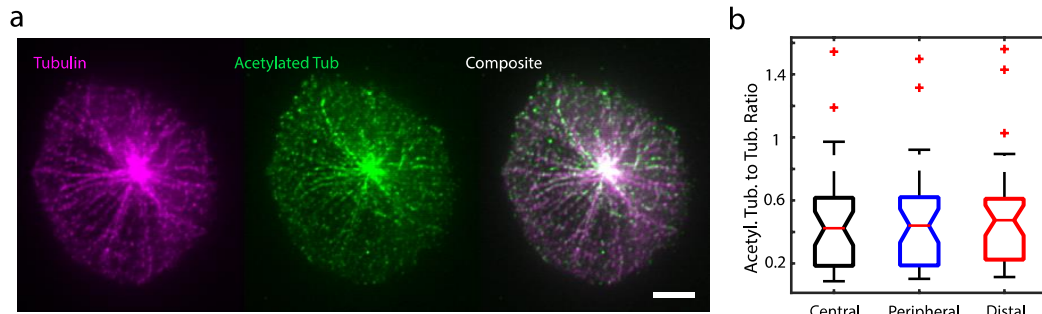
Figure 3.10. a) iSIM images of cells fixed 10 minutes after activation and immunostained for tubulin (magenta) and acetylated tubulin (green). b) Comparison of the fluorescence intensity ratio of acetylated-tubulin to tubulin in each region (central, peripheral and distal) of the cell-substrate contact zone for cells as described in a. N=50 cells.
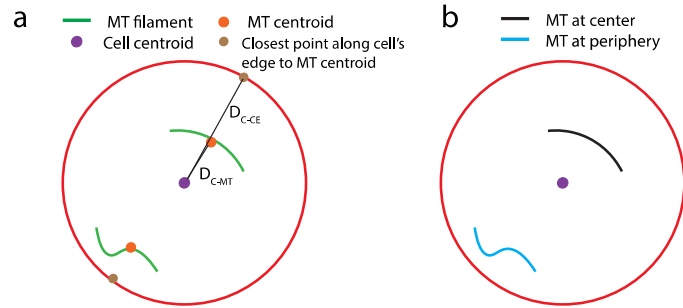
Figure 3.11. a) Schematic illustrating the process to assign a microtubule (MT) filament to a given region. The distance between the centroid of the cell and the filament centroid D_{C-MT} is calculated. Then the distance between the centroid of the cell to the closest point to the MT centroid along the cell edge D_{C-CE} is calculated. If the ratio D_{C-MT}/D_{C-CE} is less or equal to 0.4 the filament is assigned to the central region and b) plotted in black otherwise it is assigned to the peripheral region and plotted in blue.

Chapter 4: Conclusions and outlook

The formation of the immunological synapse is a critical step in the adaptive immune response carried out by B cells and T cells through interactions with antigen presenting cells. The proper formation and maturation of the IS relies on the coordination between different cytoskeletal systems. Posterior downregulation of signaling depends heavily on sustained and spatially regulated actin dynamics. In the second chapter of this dissertation I showed how actin dynamics play an important role in regulating the diffusivity of the B cell receptor and its signaling state. In the third chapter I investigated the interactions between actin and microtubules during T cell activation, specifically, how different actin architectures and actomyosin contractility regulate microtubule dynamics.

In the second chapter I used single molecule imaging to study how actin dynamics regulates BCR diffusion and signaling initiation by examining the role of the actin nucleators and nucleation promoting factors of the WASP family in regulating the diffusivity of surface BCRs and its stimulatory and inhibitory co-receptors. It is important to note that the diffusivities observed here are not entirely thermally driven (see Appendix B for more details). Analysis of single molecule trajectories was performed using pEM, a machine learning based classification algorithm that looks across a population of particle tracks and identifies unique diffusive behaviors or states. I found that BCR resides in 8 distinct states, of which the four slowest correspond to

128

BCR in clusters and are associated to signaling states. Disruption of actin dynamics, by inhibition of Arp2/3 or formin or constitutive loss of NWASP, leads to a reduction in BCR diffusivity and an increase in the number of BCR tracks in signaling states. A similar effect is observed in the signaling co-receptor CD19 but perturbation of actin dynamics does not affect the inhibitory co-receptor FcγRIIB, which suggests that the modulation of receptor diffusivity by actin is specific. These observations suggest that actin dynamics play an active role in downregulation of BCR signaling. I hypothesize that actin works as a catalyzer of the biochemical reactions at the membrane-proximal cytoplasm by stirring the cytoplasm, increasing effective diffusive rates of substrates or by reducing the interaction time between proteins by dragging them away. These results highlight the important role of actin in downregulating signaling. While this connection had been shown before, the results presented here make a more direct connection between actin dynamics and BCR mobility and signaling.

The eight distinct diffusive states described here for BCR provide a novel and more detailed picture of BCR signaling states. These states could be indicative of different signaling configurations, such as different stages of signaling maturation. Given that different receptors may become activated at different times, the use of a photoactivatable antigen to trigger the activation of BCR would be a powerful tool to synchronize the signaling stages of single BCR molecules, thus developing a clearer picture of the behavior of these states over time. This approach would also allow making a better distinction between the roles of WASP and N-WASP in BCR mobility

modulation, since these proteins are activated at different signaling stages and are involved in different aspects of the immune synapse formation. The classification strategy is a powerful tool to extract information from a complex system like the diffusion of receptors in a heterogeneous membrane. However, a better interpretation of the results is possible if more information is obtained from the system under study. Our studies showing that BCR mobility is regulated by actin dynamics suggests a number of potential experiments and analysis to construct a physical picture of these findings. In recent years, several studies have suggested that dynamic actin filaments near the plasma membrane give rise to non-equilibrium structures, such as asters and foci, which in turn affect the mobility and clustering of membrane proteins. In order to detect signatures of these active mechanisms, and to study transitions between different modes of diffusion, we need to monitor single molecules over longer times without photobleaching. These will allow us to calculate various quantities from the trajectories to help us determine the role of active mechanisms. Such future studies require optimization of our imaging techniques and/or the use of more advanced fluorescence probes. Improved imaging methods such as simultaneous multispectral single molecule imaging will also enable us to visualize and track membrane receptors simultaneously with signaling molecules to directly correlate BCR and co-receptor diffusivity with signaling. This would allow obtaining information from different receptors and proteins involved in the BCR signaling pathway simultaneously. Such an approach would allow us to more directly associate diffusive states of BCR and associated proteins with their biochemical states. This could be further strengthened by correlation

130

analysis to better bridge biochemical interactions and diffusive behaviors. The actin dynamics analysis performed determines actin flows over ~ 500 nm^2 regions and averaged over a few seconds, however the receptor dynamics studied occur in a millisecond scale. Thus the use of higher resolution imaging of actin dynamics, using photoactivatable F-actin markers and single-particle tracking would allow a better connection between actin and receptor dynamics at short spatial and temporal scales. Finally, perturbations of actomyosin dynamics will enable us to determine the relationship between BCR clustering, signaling and active forces at the single molecule level.

In the third chapter I used fluorescence microscopy and quantitative image analysis to investigate the modulation of microtubule dynamics by the actomyosin cytoskeleton in activated Jurkat T cells. This cell line was chosen due to the concentric actin patterns they display, the larger size (>25 μm in spread diameter) and the ease of transfection and fluorescent protein expression. While mouse primary T cells have been shown to display similar actin patterns as Jurkat cells and are more appropriate systems for immunological studies, the smaller size and availability makes them harder to work with. The actomyosin – microtubule crosstalk studied here in Jurkat T cells is of high relevance for biophysical studies on the interaction between different cytoskeletal components, and may be relevant in general for cytoskeleton biology and may provide novel information on the role of microtubules during immune synapse formation.

Here, I studied the role of Arp2/3 and formin generated actin structures on MT growth and dynamics using chemical perturbations. Microtubule growth rates and filament dynamics vary across the different regions of the immune synapse. MT growth is slowest in the distal actin-rich region and formin inhibition leads to a moderate decrease in MT growth rates at the peripheral region. Integrin engagement enhanced the effect of formin inhibition in cells, causing a strong reduction in MT growth rates while Arp2/3 inhibition produced the opposite effect. Microtubule filaments display higher curvatures and increased dynamics in the peripheral actomyosin rich region of the cell-substrate contact compared to the central actin-depleted zone. Inhibition of formin and Arp2/3 as well as inhibition of ROCK kinase resulted in decreased deformations and shape fluctuations of MT filaments indicating that actin dynamics and actomyosin contractility play an important role in defining MT shapes. These results suggest an important mechanical coupling between the actomyosin and microtubule systems where different actin structures influence microtubule dynamics in distinct ways.

A next step for the actin-MT crosstalk study presented here is to explore the role of proteins that are known to mediate the interactions between these cytoskeletal systems. A number of proteins have been identified in a variety of cell types that mediate actin/microtubule interactions. The EB1 C-terminal binds to proteins that regulate actin polymerization, including the Dia family of formins, which stabilize MTs as well as nucleate and elongate actin filaments, Adenomatous polyposis coli (Apc), a large 370 kD protein that regulates MT dynamics and synergizes with mDia1 to nucleate actin

132

assembly, and CLIP-170, a scaffold protein that regulates actin. EB1 inhibits Apc/mDia1 mediated actin assembly while EB1/CLIP-170 complexes stabilize MTs and facilitate rapid mDia1-mediated actin polymerization. Thus, a hierarchical network of +TIP and associated proteins serve to link MT stability and formin-mediated actin polymerization. Finally, MT associated Rho-GEFs such as GEF-H1 to regulate myosin contractility. A functional understanding of the crosstalk between actin and MT cytoskeletons can be derived by various manipulations (knockdowns, mutations or optogenetic perturbations) of these MT associated proteins and studying the effect on T cell signaling and activation by studying markers of early signaling such as ZAP-70. Finally, knock down of proteins of the spectraplakin family like MACF-1 (Microtubule Actin Crosslinking Factor) will further the understanding of the interactions between actin and microtubules and the nature of their mechanical coupling.

Microtubules are known to be of high importance for signaling propagation and maturation and are intricately connected with signaling proteins. Microtubules facilitate receptors and adaptor protein recycling and the kinases of the Syk family that phosphorylate important adaptor proteins are also required for the establishment of a stable microtubule network at the synapse. Thus, there is a clear connection between microtubule growth dynamics and signaling, however the role in signaling of microtubule shapes and shape fluctuations will require further studies. Overall, these extensions of the work in this dissertation will identify how the mechanistic basis of actin/MT crosstalk and its effect on T cell signaling, contractility and function.

It is important to note that the results presented here were obtained from experiments performed on surrogate flat surfaces. Both B cells and T cells interact with antigen presenting cells with complex nanotopography, much lower stiffness than glass and antigen mobility that is likely to differ from in vitro systems such as supported lipid bilayers or antigen coated glass surfaces. In order to study single molecule dynamics on complex topographies it is necessary to use 3D imaging methods that combine isotropic resolution with high imaging rates (over 20 frames per second) – such imaging technologies may not exist at the moment. Moreover, it is certainly possible that ligand mobility on cells can have an influence on the observed actin and receptor dynamics. However many studies of BCR diffusivity are performed on glass substrates and the overall diffusivity distributions are not significantly different from the ones using mobile ligands (bilayers). Moreover, T cells display very similar actin architectures on glass substrates, supported lipid bilayers as well as cell-cell conjugates, suggesting that the overall set of phenomena we observe is unlikely to be qualitatively different across these conditions. Nevertheless, it is likely that the contraction of the cell, typically observed in cells on bilayers or conjugates may apply compressive loads on microtubules thereby affecting their dynamics.

The work presented here, furthers our understanding of how cytoskeletal dynamics shape the spatiotemporal organization of immune receptors and subsequent signaling.

These results will have implications in the development of vaccines and therapies for autoimmune diseases and cancer and potentially the development of immunotherapies.

Appendices

Appendix A: Microscopy techniques used

Microscopes allow us to explore the world of microorganisms and they have become essential tools for the study of properties and dynamics of biological systems at multiple scales, resolving single molecules in cells to single cells in tissues and developing organisms. Optical microscopy has been a continuously evolving technique ever since the development of the first compound microscope in 1590 by Zacharias Janssen. The advances on microscopy have been made both through the improvement of the equipment, by optimization of the optical elements configuration, and by innovations in the sample staining and preparation. Perhaps one of the most revolutionary improvements came with the use of fluorescent markers, which allow observing specific proteins through the use fluorophores bound to antibodies or to genetically encoded proteins.

Fluorescence microscopy is one of the most powerful light microscopy techniques since it allows the investigation of specific organelles and proteins inside the cell.

Within fluorescence microscopy there are variations in the way the sample is illuminated to restrict fluorophores excitation and improve the resolution. The most common illumination configuration in fluorescence microscopes is widefield (see Figure A.1a, left panel) where the whole sample is illuminated and the fluorescence from different planes is detected. While widefield is a useful technique, sometimes the phenomena of interest occurs at the interface between the cell and the coverslip, such is the case for immune synapse formation studies like the ones presented in this thesis. Total internal reflection fluorescence microscopy (TIRF) is ideal for the study of the interface between cell and substrate. In TIRF the excitation light reaches the interface at a critical angle at which it is completely reflected. If there is a difference in refractive index in the materials at the interface (glass and cell or water) an evanescent wave is generated [157] and excites the fluorophores within ~100 nanometers from the glass surface (see FigureA.1a, right panel). The TIRF illumination pattern reduces the background fluorescence and improves the resolution of cell features at the cell-glass interface (Figure A.1b).

Despite the improvements in resolution and contrast obtained from different optical sectioning techniques there is a limit to the capability of resolving two features using light. This limit is known as the diffraction barrier and it restricts the ability to distinguish between two objects separated by a lateral distance of about less than the wavelength (~250 nm) of the light used to image. However, lowering the density of molecules imaged at a time by, for example, stochastic photoactivation [158, 159], it

136

is possible to improve the localization precision of single emitters down to a few tens of nanometers by adjusting a Gaussian fit to their intensity profile [160]. In Chapter 2 of this thesis we used a technique known as single molecule tracking which combines TIRF illumination with low density of fluorophores allowing an improvement in the resolution of the position of the molecules [161] to a few tens of nanometers.

Another recently developed microscopy technique; structured illumination microscopy (SIM) provides improvement in the lateral resolution using conventional fluorophores at normal densities. In SIM the sample is sequentially illuminated by a series of patterns, the images obtained are linearly processed and allow a reconstruction of the sample with twice the normal resolution [162]. York et al. developed an analog implementation of structured illumination microscopy which enables 3D super-resolution with a lateral resolution of 145 nm and axial resolution of 350 nm [44]. Instant SIM (iSIM) uses optical instead of digital image processing operations, thus allowing much faster imaging rates. In this thesis, iSIM was used to study the dynamics of actin in primary B cells and to study actin and microtubule dynamics in Jurkat cells. Figure A.1c shows a two-channel (F-actin and microtubules) iSIM image of a fixed Jurkat cell. The white dashed line was used to generate an orthogonal view (using ImageJ) as shown in Figure A.1d, where the yellow arrows point the thin (~1 μm) region where actin and microtubules overlap at the contact zone. The nucleus of lymphocytes occupy a large volume of the cells leaving a small volume occupied by cytoplasmic proteins near the membrane. In Chapter 3 of this thesis iSIM images were

137

used to study microtubule deformation. The higher resolution of iSIM allows better identification and segmentation of microtubule shapes (see Figure A.1e,f).
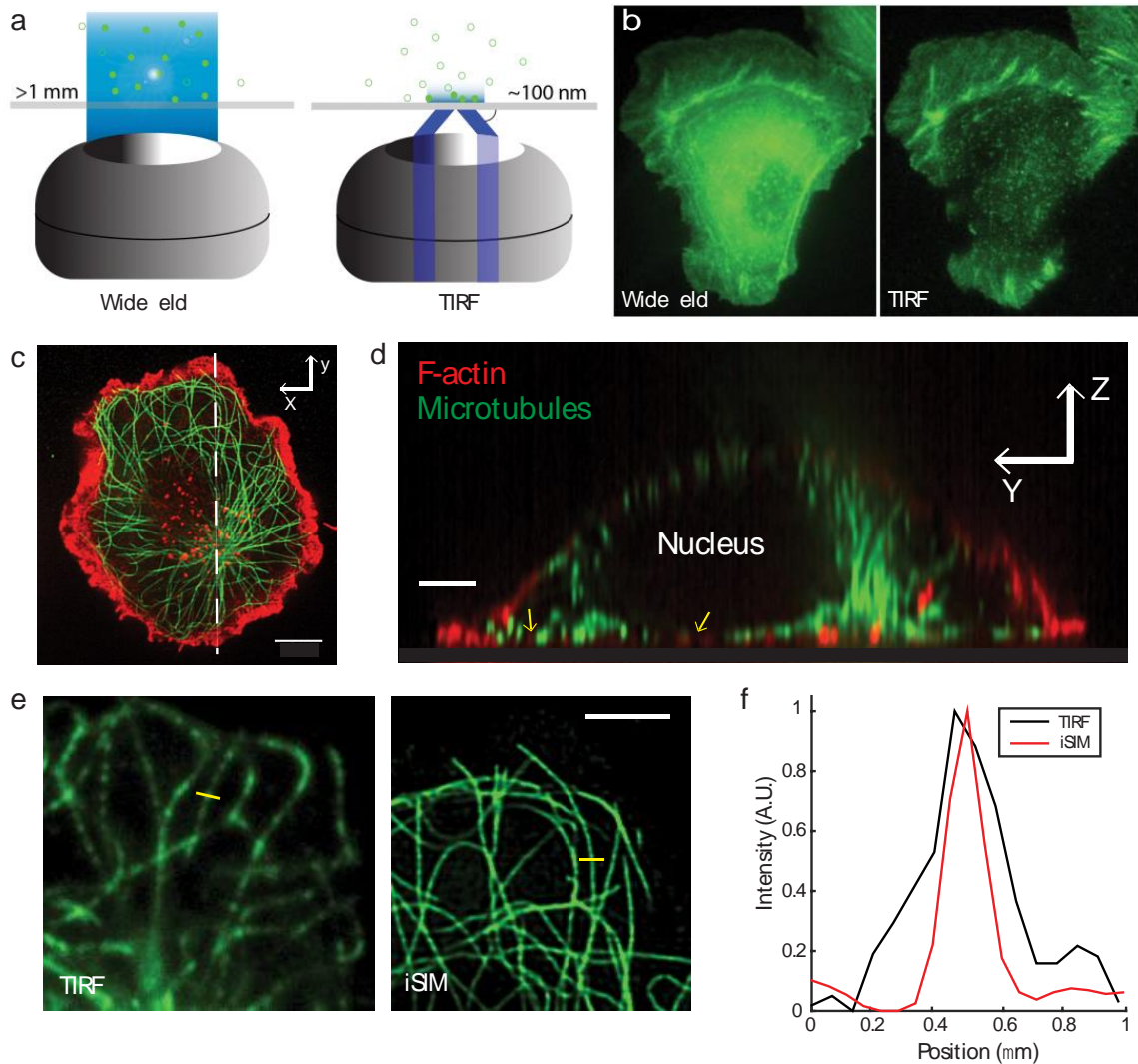

Figure A.1. Microscopy techniques employed. a) Schematics showing the illumination within the sample produced by widefield and TIRF microscopy (Total Internal Reflection Fluorescence). b) Sample images of widefield and TIRF microscopy of EGFP actin in MTLn3 live cells showing the improvement in resolution

obtained from TIRF illumination. c) Single Z slice image taken with iSIM of a fixed Jurkat cell with F-actin in red (rhodamine phalloidin staining) and microtubules in green (beta tubulin and Alexa Fluor 488). d) Orthogonal view across the dashed line in c showing the lateral distribution of F-actin and microtubules in the cell. The yellow arrows mark the small region (~ 1 μm) of overlap of actin and microtubules at the contact zone with the anti-CD3 coated glass. e) TIRF (left) and iSIM (right) images of microtubules. f) Comparison of the intensity profile across a microtubule filament obtained from the yellow lines in e for TIRF (black) and iSIM (red). All scale bars are 5 μm long. Panels a and b were adapted from [163].

Appendix B: Note on Brownian motion and diffusivity

Brownian dynamics is the random motion displayed by a molecule as the result of collisions with other molecules as a result of their kinetic energy, thus being a thermally driven process. Robert Brown first described this random motion in 1827 after the observation of pollen molecules in water. Years later, Albert Einstein developed a mathematical description of the phenomena providing a link between the macroscopic properties of a system (such as temperature) and the microscopic dynamics of a molecule. A parameter that describes the dynamics of molecules undergoing thermal-induced motion is the diffusion coefficient D, which can be obtained from the Einstein-

Stokes equation: $D = \frac{k_B T}{6\pi\eta r}$, where k_B is the Boltzmann constant, T is temperature, η is

the viscosity and r is the radius of the molecule. The displacements made by a molecule

displaying Brownian motion have square root dependence with time described by

$\langle \Delta x^2 \rangle = qD\Delta t$, where q is a constant the depends in the dimensionality of the dynamics

(2 for 1D, 4 for 2D, 6 for 3D), D is the diffusion coefficient and $\langle \Delta x^2 \rangle$ is the mean

square displacement or MSD. In many biophysical studies, the MSD has been used to

characterize the mobility of proteins in the cell membrane. However, it is important to

note that the dynamics displayed by these proteins is not entirely thermally driven and

likely to be modulated by interactions with other proteins or by drag or propulsive

forces generated by the actin cytoskeleton. The procedure to calculate the MSD from a

particle track is explained in Figure B.1a where for each time lag Δt the displacements

are calculated and averaged. Figure B.1b shows four particle tracks and their respective

color-matched MSD curves. The diffusivity can be calculated from the slope of the

curve and provides a measure of the effective mobility of the particle (compare for

example orange and blue tracks in Figure B.1b). It is important to note that the points

along the MSD curve are not statistically independent. In this thesis, we calculated

effective BCR mobilities using the covariance-based estimator [116] which is an

unbiased and regression-free method to calculate the diffusivity coefficients from

protein trajectories. In Chapter 2, pEM was used to classify the BCR trajectories into

eight different states, one can find however much less states from tracks of lipids in

supported lipid bilayers as shown in Figure B.1.c-e.
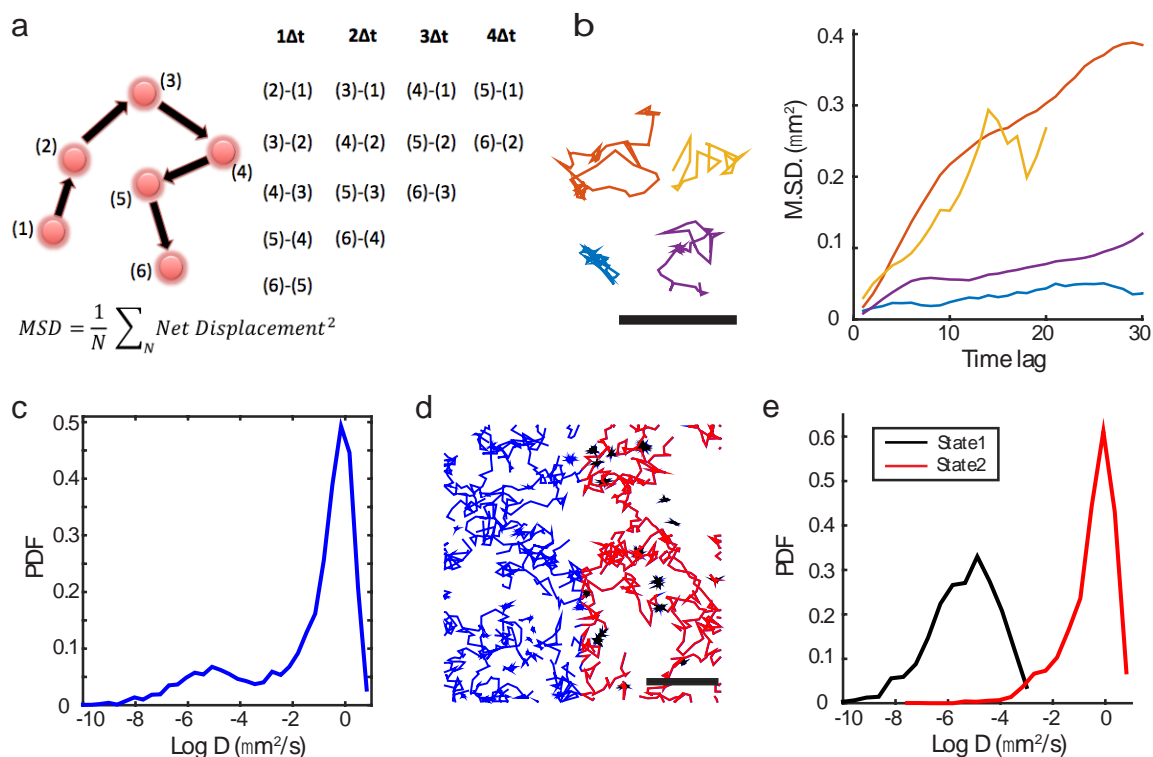
Figure B.1. Diffusivity calculation from single particle tracks. a) Schematics showing how the mean square displacement (MSD) is constructed from the position of the particle at different time points. b) Single BCR tracks and their respective color matching MSD plots. Scale bar is 1 μm. c) Probability distribution plot of the diffusivities (in log scale) for lipids fluorescently labeled in a supported lipid bilayer (as used in chapter 2). d) Sample single molecule trajectories measured in a supported lipid bilayer. Using pEM the trajectories shown in blue can be classified based in their diffusive properties shown in black and red. Scale bar is 2 μm. e) Probability distribution plot of the diffusivities shown in c after being classified by pEM into two

distinct diffusive states where state 1 (black) is the slow and state 2 (red) is the fast diffusive state.

Bibliography

1. Théry C, Amigorena S (2001) The cell biology of antigen presentation in dendritic cells. Curr Opin Immunol 13:45–51. https://doi.org/https://doi.org/10.1016/S0952-7915(00)00180-1

2. KABBAS, ABUL; LICHTMAN A (2009) Basic Immunology: Functions and Disorders of the Immune System, 3 RD. SAUNDERS ELSEVIER

3. P. AB. JA. LJ. RM. RK. & W (2002) Molecular biology of the cell, 6th ed. New York, Garland Science

4. MOLNAR, CHARLES; GAIR J CONCEPTS OF BIOLOGY, 1ST ed. B.C. OPEN TEXTBOOK PROJECT

5. Janeway CA Jr, Travers P, Walport M et al. (2001) Immunobiology: The Immune System in Health and Disease, 5th ed. Garland Science

6. Pollard TD, Borisy GG (2003) Cellular Motility Driven by Assembly and Disassembly of Actin Filaments. Cell 112:453–465. https://doi.org/https://doi.org/10.1016/S0092-8674(03)00120-X

7. Goley ED, Welch MD (2006) The ARP2/3 complex: an actin nucleator comes of age. Nat Rev Mol Cell Biol 7:713–726. https://doi.org/10.1038/nrm2026

8. MILLARD TH, SHARP SJ, MACHESKY LM (2004) Signalling to actin assembly via the WASP (Wiskott-Aldrich syndrome protein)-family proteins and the Arp2/3 complex. Biochem J 380:1 LP – 17

9. Zalevsky J, Lempert L, Kranitz H, Mullins RD (2001) Different WASP family proteins stimulate different Arp2/3 complex-dependent actin-nucleating activities. Curr Biol 11:1903–1913. https://doi.org/10.1016/S0960-9822(01)00603-0

10. Breitsprecher D, Goode BL (2013) Formins at a glance. J Cell Sci 126:1 LP – 7. https://doi.org/10.1242/jcs.107250

11. Ueda H, Zhou J, Xie J, Davis MM (2015) Distinct Roles of Cytoskeletal Components in Immunological Synapse Formation and Directed Secretion. J

Immunol 195:4117 LP – 4125. https://doi.org/10.4049/jimmunol.1402175

12. Desai A, Mitchison TJ (1997) MICROTUBULE POLYMERIZATION DYNAMICS. Annu Rev Cell Dev Biol 13:83–117. https://doi.org/10.1146/annurev.cellbio.13.1.83

13. Akhmanova A, Steinmetz MO (2015) Control of microtubule organization and dynamics: two ends in the limelight. Nat Rev Mol Cell Biol 16:711–726. https://doi.org/10.1038/nrm4084

14. Heald R, Nogales E (2002) Microtubule dynamics. J Cell Sci 115:3 LP – 4

15. Muroyama A, Lechler T (2017) Microtubule organization, dynamics and functions in differentiated cells. Development 144:3012 LP – 3021. https://doi.org/10.1242/dev.153171

16. Akhmanova A, Steinmetz MO (2010) Microtubule +TIPs at a glance. J Cell Sci 123:3415 LP – 3419. https://doi.org/10.1242/jcs.062414

17. Mattie FJ, Stackpole MM, Stone MC, et al (2010) Directed Microtubule Growth, +TIPs, and Kinesin-2 Are Required for Uniform Microtubule Polarity in Dendrites. Curr Biol 20:2169–2177. https://doi.org/10.1016/j.cub.2010.11.050

18. Tolar P, Sohn HW, Pierce SK (2005) The initiation of antigen-induced B cell antigen receptor signaling viewed in living cells by fluorescence resonance energy transfer. Nat Immunol 6:1168

19. Sohn HW, Tolar P, Jin T, Pierce SK (2006) Fluorescence resonance energy transfer in living cells reveals dynamic membrane changes in the initiation of B cell signaling. Proc Natl Acad Sci 103:8143 LP – 8148

20. Bálint Š, Dustin ML (2017) Localizing order to boost signaling. Elife 6:e25375. https://doi.org/10.7554/eLife.25375

21. Dal Porto JM, Gauld SB, Merrell KT, et al (2004) B cell antigen receptor signaling 101. Mol Immunol 41:599–613. https://doi.org/https://doi.org/10.1016/j.molimm.2004.04.008

22. Kurosaki T (2011) Regulation of BCR signaling. Mol Immunol 48:1287–1291.

https://doi.org/https://doi.org/10.1016/j.molimm.2010.12.007

23. Blasioli J, Goodnow CC (2002) Lyn/CD22/SHP-1 and Their Importance in Autoimmunity. In: Current Directions in Autoimmunity. pp 151–160

24. Nitschke L (2005) The role of CD22 and other inhibitory co-receptors in B-cell activation. Curr Opin Immunol 17:290–297. https://doi.org/https://doi.org/10.1016/j.coi.2005.03.005

25. Liu W, Tolar P, Song W, Kim TJ (2020) Editorial: BCR Signaling and B Cell Activation. Front Immunol 11:45. https://doi.org/10.3389/fimmu.2020.00045

26. Mattila PK, Feest C, Depoil D, et al (2013) The Actin and Tetraspanin Networks Organize Receptor Nanoclusters to Regulate B Cell Receptor-Mediated Signaling. Immunity 38:461–474. https://doi.org/https://doi.org/10.1016/j.immuni.2012.11.019

27. Maity PC, Blount A, Jumaa H, et al (2015) B cell antigen receptors of the IgM and IgD classes are clustered in different protein islands that are altered during B cell activation. Sci Signal 8:ra93 LP-ra93

28. Lee J, Sengupta P, Brzostowski J, et al (2016) The nanoscale spatial organization of B-cell receptors on immunoglobulin M– and G–expressing human B-cells. Mol Biol Cell 28:511–523. https://doi.org/10.1091/mbc.e16-06-0452

29. Yang J, Reth M (2010) Oligomeric organization of the B-cell antigen receptor on resting cells. Nature 467:465–469. https://doi.org/10.1038/nature09357

30. Kläsener K, Maity PC, Hobeika E, et al (2014) B cell activation involves nanoscale receptor reorganizations and inside-out signaling by Syk. Elife 3:e02069. https://doi.org/10.7554/eLife.02069

31. Tolar P (2017) Cytoskeletal control of B cell responses to antigens. Nat Rev Immunol 17:621

32. Yang J, Reth M (2010) The dissociation activation model of B cell antigen receptor triggering. FEBS Lett 584:4872–4877. https://doi.org/10.1016/j.febslet.2010.09.045

33. Pierce SK, Liu W (2010) The tipping points in the initiation of B cell signalling:

how small changes make big differences. Nat Rev Immunol 10:767–777. https://doi.org/10.1038/nri2853

34. Ponuwei GA (2016) A glimpse of the ERM proteins. J Biomed Sci 23:35. https://doi.org/10.1186/s12929-016-0246-3

35. Treanor B, Depoil D, Gonzalez-Granja A, et al (2010) The Membrane Skeleton Controls Diffusion Dynamics and Signaling through the B Cell Receptor. Immunity 32:187–199. https://doi.org/10.1016/j.immuni.2009.12.005

36. Ketchum C, Miller H, Song W, Upadhyaya A (2014) Ligand Mobility Regulates B Cell Receptor Clustering and Signaling Activation. Biophys J 106:26–36. https://doi.org/https://doi.org/10.1016/j.bpj.2013.10.043

37. Liu C, Miller H, Orlowski G, et al (2012) Actin Reorganization Is Required for the Formation of Polarized B Cell Receptor Signalosomes in Response to Both Soluble and Membrane-Associated Antigens. J Immunol 188:3237 LP – 3246. https://doi.org/10.4049/jimmunol.1103065

38. Bolger-Munro M, Choi K, Scurll JM, et al (2019) Arp2/3 complex-driven spatial patterning of the BCR enhances immune synapse formation, BCR signaling and B cell activation. Elife 8:e44574. https://doi.org/10.7554/eLife.44574

39. Song W, Liu C, Seeley-Fallen MK, et al (2013) Actin-mediated feedback loops in B-cell receptor signaling. Immunol Rev 256:177–189. https://doi.org/10.1111/imr.12113

40. Fleire SJ, Goldman JP, Carrasco YR, et al (2006) B Cell Ligand Discrimination Through a Spreading and Contraction Response. Science (80-) 312:738 LP – 741. https://doi.org/10.1126/science.1123940

41. Liu C, Miller H, Sharma S, et al (2012) Analyzing actin dynamics during the activation of the B cell receptor in live B cells. Biochem Biophys Res Commun 427:202–206. https://doi.org/https://doi.org/10.1016/j.bbrc.2012.09.046

42. Schnyder T, Castello A, Feest C, et al (2011) B Cell Receptor-Mediated Antigen Gathering Requires Ubiquitin Ligase Cbl and Adaptors Grb2 and Dok-3 to Recruit Dynein to the Signaling Microcluster. Immunity 34:905–918.

https://doi.org/https://doi.org/10.1016/j.immuni.2011.06.001

43. Sohn HW, Tolar P, Pierce SK (2008) Membrane heterogeneities in the formation of B cell receptor–Lyn kinase microclusters and the immune synapse. J Cell Biol 182:367 LP – 379

44. York AG, Chandris P, Nogare DD, et al (2013) Instant super-resolution imaging in live cells and embryos via analog image processing. Nat Methods 10:1122

45. Freeman SA, Lei V, Dang-Lawson M, et al (2011) Cofilin-Mediated F-Actin Severing Is Regulated by the Rap GTPase and Controls the Cytoskeletal Dynamics That Drive Lymphocyte Spreading and BCR Microcluster Formation. J Immunol 187:5887 LP – 5900. https://doi.org/10.4049/jimmunol.1102233

46. Freeman SA, Jaumouillé V, Choi K, et al (2015) Toll-like receptor ligands sensitize B-cell receptor signalling by reducing actin-dependent spatial confinement of the receptor. Nat Commun 6:6168

47. Seeley-Fallen MK, Liu LJ, Shapiro MR, et al (2014) Actin-binding protein 1 links B-cell antigen receptors to negative signaling pathways. Proc Natl Acad Sci 111:9881 LP – 9886. https://doi.org/10.1073/pnas.1321971111

48. Alekhina O, Burstein E, Billadeau DD (2017) Cellular functions of WASP family proteins at a glance. J Cell Sci 130:2235 LP – 2241. https://doi.org/10.1242/jcs.199570

49. Sharma S, Orlowski G, Song W (2009) Btk Regulates B Cell Receptor-Mediated Antigen Processing and Presentation by Controlling Actin Cytoskeleton Dynamics in B Cells. J Immunol 182:329 LP – 339. https://doi.org/10.4049/jimmunol.182.1.329

50. Liu C, Bai X, Wu J, et al (2013) N-WASP Is Essential for the Negative Regulation of B Cell Receptor Signaling. PLOS Biol 11:1–16. https://doi.org/10.1371/journal.pbio.1001704

51. Tolar P, Hanna J, Krueger PD, Pierce SK (2009) The Constant Region of the Membrane Immunoglobulin Mediates B Cell-Receptor Clustering and Signaling in Response to Membrane Antigens. Immunity 30:44–55.

https://doi.org/http://doi.org/10.1016/j.immuni.2008.11.007

52. Wang J, Tang S, Wan Z, et al (2016) Utilization of a photoactivatable antigen system to examine B-cell probing termination and the B-cell receptor sorting mechanisms during B-cell activation. Proc Natl Acad Sci 113:E558–E567. https://doi.org/10.1073/pnas.1517612113

53. Stone MB, Veatch SL (2015) Steady-state cross-correlations for live two-colour super-resolution localization data sets. Nat Commun 6:7347

54. Gasparrini F, Feest C, Bruckbauer A, et al (2015) Nanoscale organization and dynamics of the siglec CD22 cooperate with the cytoskeleton in restraining BCR signalling. EMBO J 35:258–280. https://doi.org/10.15252/embj.201593027

55. Xu L, Xia M, Guo J, et al (2016) Impairment on the lateral mobility induced by structural changes underlies the functional deficiency of the lupus-associated polymorphism FcγRIIB-T232. J Exp Med. https://doi.org/10.1084/jem.20160528

56. Walker JA, Smith KGC (2008) CD22: an inhibitory enigma. Immunology 123:314–325. https://doi.org/10.1111/j.1365-2567.2007.02752.x

57. Rey-Suarez I, Wheatley BA, Koo P, et al (2020) WASP family proteins regulate the mobility of the B cell receptor during signaling activation. Nat Commun 11:439. https://doi.org/10.1038/s41467-020-14335-8

58. Kuokkanen E, Šuštar V, Mattila PK (2015) Molecular Control of B Cell Activation and Immunological Synapse Formation. Traffic 16:311–326. https://doi.org/10.1111/tra.12257

59. Cai E, Marchuk K, Beemiller P, et al (2017) Visualizing dynamic microvillar search and stabilization during ligand detection by T cells. Science (80-) 356:eaal3118. https://doi.org/10.1126/science.aal3118

60. Babbitt BP, Allen PM, Matsueda G, et al (1985) Binding of immunogenic peptides to Ia histocompatibility molecules. Nature 317:359–361. https://doi.org/10.1038/317359a0

61. Samelson LE, Patel MD, Weissman AM, et al (1986) Antigen activation of

murine T cells induces tyrosine phosphorylation of a polypeptide associated with the T cell antigen receptor. Cell 46:1083–1090. https://doi.org/10.1016/0092-8674(86)90708-7

62. Au-Yeung BB, Shah NH, Shen L, Weiss A (2018) ZAP-70 in Signaling, Biology, and Disease. Annu Rev Immunol 36:127–156. https://doi.org/10.1146/annurev-immunol-042617-053335

63. Thumkeo D, Katsura Y, Nishimura Y, et al (2020) mDia1/3-dependent actin polymerization spatiotemporally controls LAT phosphorylation by Zap70 at the immune synapse. Sci Adv 6:eaay2432. https://doi.org/10.1126/sciadv.aay2432

64. Billadeau DD, Nolz JC, Gomez TS (2007) Regulation of T-cell activation by the cytoskeleton. Nat Rev Immunol 7:131

65. Gascoigne NRJ (2008) Do T cells need endogenous peptides for activation? Nat Rev Immunol 8:895–900. https://doi.org/10.1038/nri2431

66. Grakoui A, Bromley SK, Sumen C, et al (1999) The Immunological Synapse: A Molecular Machine Controlling T Cell Activation. Science (80-) 285:221 LP – 227. https://doi.org/10.1126/science.285.5425.221

67. Choudhuri K, Llodrá J, Roth EW, et al (2014) Polarized release of T-cell-receptor-enriched microvesicles at the immunological synapse. Nature 507:118–123. https://doi.org/10.1038/nature12951

68. Liu W, Wang H, Xu C (2016) Antigen Receptor Nanoclusters: Small Units with Big Functions. Trends Immunol 37:680–689. https://doi.org/10.1016/j.it.2016.07.007

69. Dustin ML, Depoil D (2011) New insights into the T cell synapse from single molecule techniques. Nat Rev Immunol 11:672–684. https://doi.org/10.1038/nri3066

70. Murugesan S, Hong J, Yi J, et al (2016) Formin-generated actomyosin arcs propel T cell receptor microcluster movement at the immune synapse. J Cell Biol 215:383–399. https://doi.org/10.1083/jcb.201603080

71. Yi J, Wu XS, Crites T, et al (2012) Actin retrograde flow and actomyosin II arc

contraction drive receptor cluster dynamics at the immunological synapse in Jurkat T cells. Mol Biol Cell 23:834–852. https://doi.org/10.1091/mbc.e11-08-0731

72. Mossman KD, Campi G, Groves JT, Dustin ML (2005) Altered TCR Signaling from Geometrically Repatterned Immunological Synapses. Science (80-) 310:1191 LP – 1193. https://doi.org/10.1126/science.1119238

73. Varma R, Campi G, Yokosuka T, et al (2006) T Cell Receptor-Proximal Signals Are Sustained in Peripheral Microclusters and Terminated in the Central Supramolecular Activation Cluster. Immunity 25:117–127. https://doi.org/10.1016/j.immuni.2006.04.010

74. Ritter AT, Asano Y, Stinchcombe JC, et al (2017) Actin Depletion Initiates Events Leading to Granule Secretion at the Immunological Synapse. Immunity 42:864–876. https://doi.org/10.1016/j.immuni.2015.04.013

75. Yi J, Wu X, Chung AH, et al (2013) Centrosome repositioning in T cells is biphasic and driven by microtubule end-on capture-shrinkage. J Cell Biol 202:779 LP – 792

76. Morgan H, Audrey F, Xin L (2013) From lipid second messengers to molecular motors: microtubule-organizing center reorientation in T cells. Immunol Rev 256:95–106. https://doi.org/10.1111/imr.12116

77. Huppa JB, Davis MM (2003) T-cell-antigen recognition and the immunological synapse. Nat Rev Immunol 3:973–983. https://doi.org/10.1038/nri1245

78. Hammer JA, Wang JC, Saeed M, Pedrosa AT (2018) Origin, Organization, Dynamics, and Function of Actin and Actomyosin Networks at the T Cell Immunological Synapse. Annu Rev Immunol 37:201–224. https://doi.org/10.1146/annurev-immunol-042718-041341

79. Nolz JC, Gomez TS, Zhu P, et al (2006) The WAVE2 complex regulates actin cytoskeletal reorganization and CRAC-mediated calcium entry during T cell activation. Curr Biol 16:24–34. https://doi.org/10.1016/j.cub.2005.11.036

80. Zipfel PA, Bunnell SC, Witherow DS, et al (2006) Role for the Abi/Wave

Protein Complex in T Cell Receptor-Mediated Proliferation and Cytoskeletal Remodeling. Curr Biol 16:35–46. https://doi.org/10.1016/j.cub.2005.12.024

81. Le Floc'h A, Tanaka Y, Bantilan NS, et al (2013) Annular PIP3 accumulation controls actin architecture and modulates cytotoxicity at the immunological synapse. J Exp Med 210:2721–2737. https://doi.org/10.1084/jem.20131324

82. Rak GD, Mace EM, Banerjee PP, et al (2011) Natural Killer Cell Lytic Granule Secretion Occurs through a Pervasive Actin Network at the Immune Synapse. PLOS Biol 9:e1001151

83. Ritter AT, Kapnick SM, Murugesan S, et al (2017) Cortical actin recovery at the immunological synapse leads to termination of lytic granule secretion in cytotoxic T lymphocytes. Proc Natl Acad Sci 114:E6585 LP-E6594. https://doi.org/10.1073/pnas.1710751114

84. Kumari S, Depoil D, Martinelli R, et al (2015) Actin foci facilitate activation of the phospholipase C-γ in primary T lymphocytes via the WASP pathway. Elife 4:e04953. https://doi.org/10.7554/eLife.04953

85. Babich A, Li S, O'Connor RS, et al (2012) F-actin polymerization and retrograde flow drive sustained PLCγ1 signaling during T cell activation. J Cell Biol 197:775–787. https://doi.org/10.1083/jcb.201201018

86. Martín-Cófreces NB, Robles-Valero J, Cabrero JR, et al (2008) MTOC translocation modulates IS formation and controls sustained T cell signaling. J Cell Biol 182:951 LP – 962

87. Bustos-Morán E, Blas-Rus N, Martin-Cófreces NB, Sánchez-Madrid F (2017) Microtubule-associated protein-4 controls nanovesicle dynamics and T cell activation. J Cell Sci 130:1217 LP – 1223. https://doi.org/10.1242/jcs.199042

88. Huse M, Le Floc'h A, Liu X (2013) From lipid second messengers to molecular motors: microtubule-organizing center reorientation in T cells. Immunol Rev 256:95–106. https://doi.org/10.1111/imr.12116

89. Ritter AT, Asano Y, Stinchcombe JC, et al (2015) Actin Depletion Initiates Events Leading to Granule Secretion at the Immunological Synapse. Immunity

42:864–876. https://doi.org/10.1016/j.immuni.2015.04.013

90. Martín-Cófreces NB, Sancho D, Fernández E, et al (2006) Role of Fyn in the Rearrangement of Tubulin Cytoskeleton Induced through TCR. J Immunol 176:4201 LP – 4207. https://doi.org/10.4049/jimmunol.176.7.4201

91. Liu X, Kapoor TM, Chen JK, Huse M (2013) Diacylglycerol promotes centrosome polarization in T cells via reciprocal localization of dynein and myosin II. Proc Natl Acad Sci 110:11976 LP – 11981. https://doi.org/10.1073/pnas.1306180110

92. Gomez TS, Kumar K, Medeiros RB, et al (2007) Formins Regulate the Actin-Related Protein 2/3 Complex-Independent Polarization of the Centrosome to the Immunological Synapse. Immunity 26:177–190. https://doi.org/10.1016/j.immuni.2007.01.008

93. Andrés-Delgado L, Antón O, Alonso M (2013) Centrosome Polarization in T Cells: A Task for Formins. Front Immunol 4:191. https://doi.org/10.3389/fimmu.2013.00191

94. López MP, Huber F, Grigoriev I, et al (2014) Actin–microtubule coordination at growing microtubule ends. Nat Commun 5:4778. https://doi.org/10.1038/ncomms5778

95. Aspengren S, Wielbass L, Wallin M (2006) Effects of acrylamide, latrunculin, and nocodazole on intracellular transport and cytoskeletal organization in melanophores. Cell Motil 63:423–436. https://doi.org/10.1002/cm.20134

96. Henty-Ridilla JL, Rankova A, Eskin JA, et al (2016) Accelerated actin filament polymerization from microtubule plus ends. Science (80-) 352:1004 LP – 1009. https://doi.org/10.1126/science.aaf1709

97. Dogterom M, Koenderink GH (2019) Actin–microtubule crosstalk in cell biology. Nat Rev Mol Cell Biol 20:38–54. https://doi.org/10.1038/s41580-018-0067-1

98. Hui KL, Upadhyaya A (2017) Dynamic microtubules regulate cellular contractility during T-cell activation. Proc Natl Acad Sci 114:E4175–E4183.

https://doi.org/10.1073/pnas.1614291114

99. Hashimoto-Tane A, Yokosuka T, Sakata-Sogawa K, et al (2011) Dynein-Driven Transport of T Cell Receptor Microclusters Regulates Immune Synapse Formation and T Cell Activation. Immunity 34:919–931. https://doi.org/https://doi.org/10.1016/j.immuni.2011.05.012

100. Cambier JC, Pleiman CM, Clark MR (1994) Signal Transduction by the B Cell Antigen Receptor and its Coreceptors. Annu Rev Immunol 12:457–486. https://doi.org/10.1146/annurev.iy.12.040194.002325

101. Batista FD, Iber D, Neuberger MS (2001) B cells acquire antigen from target cells after synapse formation. Nature 411:489–494. https://doi.org/10.1038/35078099

102. Rolli V, Gallwitz M, Wossning T, et al (2002) Amplification of B Cell Antigen Receptor Signaling by a Syk/ITAM Positive Feedback Loop. Mol Cell 10:1057–1069. https://doi.org/https://doi.org/10.1016/S1097-2765(02)00739-6

103. Tolar P, Sohn HW, Liu W, Pierce SK (2009) The molecular assembly and organization of signaling active B-cell receptor oligomers. Immunol Rev 232:34–41. https://doi.org/10.1111/j.1600-065X.2009.00833.x

104. Charrier C, Ehrensperger M-V, Dahan M, et al (2006) Cytoskeleton Regulation of Glycine Receptor Number at Synapses and Diffusion in the Plasma Membrane. J Neurosci 26:8502 LP – 8511. https://doi.org/10.1523/JNEUROSCI.1758-06.2006

105. Lenne P-F, Wawreziniecke L, Conchonaud F, et al (2006) Dynamic molecular confinement in the plasma membrane by microdomains and the cytoskeleton meshwork. EMBO J 25:3245–3256. https://doi.org/10.1038/sj.emboj.7601214

106. Sheetz MP, Schindler M, Koppel DE (1980) Lateral mobility of integral membrane proteins is increased in spherocytic erythrocytes. Nature 285:510–512. https://doi.org/10.1038/285510a0

107. Treanor B, Depoil D, Gonzalez-Granja A, et al (2010) The Membrane Skeleton Controls Diffusion Dynamics and Signaling through the B Cell Receptor.

Immunity 32:187–199. https://doi.org/http://doi.org/10.1016/j.immuni.2009.12.005

108. Treanor B, Depoil D, Bruckbauer A, Batista FD (2011) Dynamic cortical actin remodeling by ERM proteins controls BCR microcluster organization and integrity. J Exp Med 208:1055–1068. https://doi.org/10.1084/jem.20101125

109. Machesky LM, Insall RH (1998) Scar1 and the related Wiskott–Aldrich syndrome protein, WASP, regulate the actin cytoskeleton through the Arp2/3 complex. Curr Biol 8:1347–1356. https://doi.org/10.1016/S0960-9822(98)00015-3

110. Miki H, Miura K, Takenawa T (1996) N-WASP, a novel actin-depolymerizing protein, regulates the cortical cytoskeletal rearrangement in a PIP2-dependent manner downstream of tyrosine kinases. EMBO J 15:5326–5335

111. Symons M, Derry JMJ, Karlak B, et al (1996) Wiskott–Aldrich Syndrome Protein, a Novel Effector for the GTPase CDC42Hs, Is Implicated in Actin Polymerization. Cell 84:723–734. https://doi.org/10.1016/S0092-8674(00)81050-8

112. Brownlie RJ, Lawlor KE, Niederer HA, et al (2008) Distinct cell-specific control of autoimmunity and infection by FcgammaRIIb. J Exp Med 205:883–895. https://doi.org/10.1084/jem.20072565

113. Fearon DT, Carroll MC, Carroll MC (2000) Regulation of B Lymphocyte Responses to Foreign and Self-Antigens by the CD19/CD21 Complex. Annu Rev Immunol 18:393–422. https://doi.org/10.1146/annurev.immunol.18.1.393

114. Rey I, Garcia DA, Wheatley BA, et al (2018) Biophysical Techniques to Study B Cell Activation: Single-Molecule Imaging and Force Measurements. In: Liu C (ed) B Cell Receptor Signaling: Methods and Protocols. Springer New York, New York, NY, pp 51–68

115. Frost NA, Shroff H, Kong H, et al (2010) Single-Molecule Discrimination of Discrete Perisynaptic and Distributed Sites of Actin Filament Assembly within Dendritic Spines. Neuron 67:86–99.

https://doi.org/10.1016/j.neuron.2010.05.026

116. Vestergaard CL, Blainey PC, Flyvbjerg H (2014) Optimal estimation of diffusion coefficients from single-particle trajectories. Phys Rev E 89:22726. https://doi.org/10.1103/PhysRevE.89.022726

117. Koo PK, Weitzman M, Sabanaygam CR, et al (2015) Extracting Diffusive States of Rho GTPase in Live Cells: Towards In Vivo Biochemistry. PLOS Comput Biol 11:e1004297

118. Koo PK, Mochrie SGJ (2016) Systems-level approach to uncovering diffusive states and their transitions from single-particle trajectories. Phys Rev E 94:52412. https://doi.org/10.1103/PhysRevE.94.052412

119. Sengupta P, Jovanovic-Talisman T, Skoko D, et al (2011) Probing protein heterogeneity in the plasma membrane using PALM and pair correlation analysis. Nat Methods 8:969–975. https://doi.org/10.1038/nmeth.1704

120. Depoil D, Fleire S, Treanor BL, et al (2008) CD19 is essential for B cell activation by promoting B cell receptor–antigen microcluster formation in response to membrane-bound ligand. Nat Immunol 9:63–72. https://doi.org/10.1038/ni1547

121. Ono M, Bolland S, Tempst P, Ravetch J V (1996) Role of the inositol phosphatase SHIP in negative regulation of the immune system by the receptor FeγRIIB. Nature 383:263–266. https://doi.org/10.1038/383263a0

122. Xu L, Li G, Wang J, et al (2014) Through an ITIM-Independent Mechanism the FcγRIIB Blocks B Cell Activation by Disrupting the Colocalized Microclustering of the B Cell Receptor and CD19. J Immunol 192:5179 LP – 5191. https://doi.org/10.4049/jimmunol.1400101

123. Hebert B, Costantino S, Wiseman PW (2005) Spatiotemporal Image Correlation Spectroscopy (STICS) Theory, Verification, and Application to Protein Velocity Mapping in Living CHO Cells. Biophys J 88:3601–3614. https://doi.org/10.1529/biophysj.104.054874

124. Isogai T, van der Kammen R, Leyton-Puig D, et al (2015) Initiation of

lamellipodia and ruffles involves cooperation between mDia1 and the Arp2/3 complex. J Cell Sci 128:3796 LP – 3810. https://doi.org/10.1242/jcs.176768

125. Deng S, Bothe I, Baylies MK (2015) The Formin Diaphanous Regulates Myoblast Fusion through Actin Polymerization and Arp2/3 Regulation. PLOS Genet 11:e1005381

126. Sakata D, Taniguchi H, Yasuda S, et al (2007) Impaired T lymphocyte trafficking in mice deficient in an actin-nucleating protein, mDia1 . J Exp Med 204:2031–2038. https://doi.org/10.1084/jem.20062647

127. Stone MB, Shelby SA, Núñez MF, et al (2017) Protein sorting by lipid phase-like domains supports emergent signaling function in B lymphocyte plasma membranes. Elife 6:e19891. https://doi.org/10.7554/eLife.19891

128. Veatch SL, Chiang EN, Sengupta P, et al (2012) Quantitative Nanoscale Analysis of IgE-FcεRI Clustering and Coupling to Early Signaling Proteins. J Phys Chem B 116:6923–6935. https://doi.org/10.1021/jp300197p

129. Shelby SA, Veatch SL, Holowka DA, Baird BA (2016) Functional nanoscale coupling of Lyn kinase with IgE-FcεRI is restricted by the actin cytoskeleton in early antigen-stimulated signaling. Mol Biol Cell 27:3645–3658. https://doi.org/10.1091/mbc.E16-06-0425

130. Chaudhuri A, Bhattacharya B, Gowrishankar K, et al (2011) Spatiotemporal regulation of chemical reactions by active cytoskeletal remodeling. Proc Natl Acad Sci 108:14825 LP – 14830

131. Fritzsche M, Fernandes RA, Chang VT, et al (2017) Cytoskeletal actin dynamics shape a ramifying actin network underpinning immunological synapse formation. Sci Adv 3:e1603032. https://doi.org/10.1126/sciadv.1603032

132. Riedl J, Flynn KC, Raducanu A, et al (2010) Lifeact mice for studying F-actin dynamics. Nat Methods 7:168

133. Peluso P, Wilson DS, Do D, et al (2003) Optimizing antibody immobilization strategies for the construction of protein microarrays. Anal Biochem 312:113–124. https://doi.org/http://doi.org/10.1016/S0003-2697(02)00442-6

134. Alarcón B, Mestre D, Martínez-Martín N (2011) The immunological synapse: a cause or consequence of T-cell receptor triggering? Immunology 133:420–425. https://doi.org/10.1111/j.1365-2567.2011.03458.x

135. Hong J, Murugesan S, Betzig E, Hammer JA (2017) Contractile actomyosin arcs promote the activation of primary mouse T cells in a ligand-dependent manner. PLoS One 12:e0183174–e0183174. https://doi.org/10.1371/journal.pone.0183174

136. Rotty JD, Bear JE (2015) Competition and collaboration between different actin assembly pathways allows for homeostatic control of the actin cytoskeleton. Bioarchitecture 5:27–34. https://doi.org/10.1080/19490992.2015.1090670

137. Lomakin AJ, Lee K-C, Han SJ, et al (2015) Competition for actin between two distinct F-actin networks defines a bistable switch for cell polarization. Nat Cell Biol 17:1435

138. Martín-Cófreces NB, Baixauli F, López MJ, et al (2012) End-binding protein 1 controls signal propagation from the T cell receptor. EMBO J 31:4140 LP – 4152

139. Wang JC, Lee JY-J, Christian S, et al (2017) The Rap1–cofilin-1 pathway coordinates actin reorganization and MTOC polarization at the B cell immune synapse. J Cell Sci 130:1094 LP – 1109. https://doi.org/10.1242/jcs.191858

140. BREHM MA, SCHREIBER I, BERTSCH U, et al (2004) Identification of the actin-binding domain of Ins(1,4,5)P3 3-kinase isoform B (IP3K-B). Biochem J 382:353–362. https://doi.org/10.1042/BJ20031751

141. Jaqaman K, Loerke D, Mettlen M, et al (2008) Robust single-particle tracking in live-cell time-lapse sequences. Nat Methods 5:695–702. https://doi.org/10.1038/nmeth.1237

142. Jankowska KI, Williamson EK, Roy NH, et al (2018) Integrins Modulate T Cell Receptor Signaling by Constraining Actin Flow at the Immunological Synapse . Front. Immunol. 9:25

143. Lam Hui K, Kwak SI, Upadhyaya A (2014) Adhesion-dependent modulation of actin dynamics in Jurkat T cells. Cytoskeleton 71:119–135.

https://doi.org/10.1002/cm.21156

144. Brangwynne CP, MacKintosh FC, Weitz DA (2007) Force fluctuations and polymerization dynamics of intracellular microtubules. Proc Natl Acad Sci U S A 104:16128–16133. https://doi.org/10.1073/pnas.0703094104

145. Brangwynne CP, Koenderink GH, MacKintosh FC, Weitz DA (2008) Nonequilibrium Microtubule Fluctuations in a Model Cytoskeleton. Phys Rev Lett 100:118104. https://doi.org/10.1103/PhysRevLett.100.118104

146. Bulinski JC, Odde DJ, Howell BJ, et al (2001) Rapid dynamics of the microtubule binding of ensconsin in vivo. J Cell Sci 114:3885 LP – 3897

147. Clausen MP, Colin-York H, Schneider F, et al (2017) Dissecting the actin cortex density and membrane-cortex distance in living cells by super-resolution microscopy. J Phys D Appl Phys 50:64002. https://doi.org/10.1088/1361-6463/aa52a1

148. Chugh P, Clark AG, Smith MB, et al (2017) Actin cortex architecture regulates cell surface tension. Nat Cell Biol 19:689–697. https://doi.org/10.1038/ncb3525

149. Koenderink GH, Paluch EK (2018) Architecture shapes contractility in actomyosin networks. Curr Opin Cell Biol 50:79–85. https://doi.org/https://doi.org/10.1016/j.ceb.2018.01.015

150. Andrés-Delgado L, Antón OM, Bartolini F, et al (2012) INF2 promotes the formation of detyrosinated microtubules necessary for centrosome reorientation in T cells. J Cell Biol 198:1025–1037. https://doi.org/10.1083/jcb.201202137

151. Serrador JM, Cabrero JR, Sancho D, et al (2004) HDAC6 Deacetylase Activity Links the Tubulin Cytoskeleton with Immune Synapse Organization. Immunity 20:417–428. https://doi.org/10.1016/S1074-7613(04)00078-0

152. Xu Z, Schaedel L, Portran D, et al (2017) Microtubules acquire resistance from mechanical breakage through intralumenal acetylation. Science (80-) 356:328 LP – 332. https://doi.org/10.1126/science.aai8764

153. Brangwynne CP, MacKintosh FC, Kumar S, et al (2006) Microtubules can bear enhanced compressive loads in living cells because of lateral reinforcement. J

Cell Biol 173:733–741. https://doi.org/10.1083/jcb.200601060

154. Bicek AD, Tüzel E, Kroll DM, Odde DJBT-M in CB (2007) Analysis of Microtubule Curvature. In: Cell Mechanics. Academic Press, pp 237–268

155. Bicek AD, Tüzel E, Demtchouk A, et al (2009) Anterograde Microtubule Transport Drives Microtubule Bending in LLC-PK1 Epithelial Cells. Mol Biol Cell 20:2943–2953. https://doi.org/10.1091/mbc.e08-09-0909

156. Massey FJ (1951) The Kolmogorov-Smirnov Test for Goodness of Fit. J Am Stat Assoc 46:68–78. https://doi.org/10.2307/2280095

157. Axelrod D (1981) Cell-substrate contacts illuminated by total internal reflection fluorescence. J Cell Biol 89:141–145. https://doi.org/10.1083/jcb.89.1.141

158. Betzig E, Patterson GH, Sougrat R, et al (2006) Imaging Intracellular Fluorescent Proteins at Nanometer Resolution. Science (80-) 313:1642 LP – 1645

159. Rust MJ, Bates M, Zhuang X (2006) Sub-diffraction-limit imaging by stochastic optical reconstruction microscopy (STORM). Nat Meth 3:793–796

160. Thompson RE, Larson DR, Webb WW (2002) Precise Nanometer Localization Analysis for Individual Fluorescent Probes. Biophys J 82:2775–2783. https://doi.org/10.1016/S0006-3495(02)75618-X

161. Gordon MP, Ha T, Selvin PR (2004) Single-molecule high-resolution imaging with photobleaching. Proc Natl Acad Sci U S A 101:6462 LP – 6465. https://doi.org/10.1073/pnas.0401638101

162. Gustafsson MGL (2000) Surpassing the lateral resolution limit by a factor of two using structured illumination microscopy. J Microsc 198:82–87. https://doi.org/10.1046/j.1365-2818.2000.00710.x

163. Epifluorescence vs TIRF microscopy